論文 / 著書情報
Article / Book Information

題目(和文)	銀河拡散光の観測による星間ダストの研究
Title(English)	Study of interstellar dust from measurements of Diffuse Galactic Light
著者(和文)	大西陽介
Author(English)	Yosuke Onishi
出典(和文)	学位:博士(理学), 学位授与機関:東京工業大学, 報告番号:甲第10395号, 授与年月日:2017年3月26日, 学位の種別:課程博士, 審査員:松原 英雄,河合 誠之,堂谷 忠靖,宗宮 健太郎,野村 英子,尾中 敬
Citation(English)	Degree:Doctor (Science), Conferring organization: Tokyo Institute of Technology, Report number:甲第10395号, Conferred date:2017/3/26, Degree Type:Course doctor, Examiner:,,,,,
学位種別(和文)	博士論文
Type(English)	Doctoral Thesis

Study of interstellar dust from measurements of Diffuse Galactic Light

Yosuke Onishi

Department of Physics, Graduate School of Science,
Tokyo Institute of Technology

December, 2016

Abstract

Diffuse Galactic Light (DGL) is the scattered starlight by interstellar dust grains in the Galaxy. DGL gives us crucial information on optical properties especially size of interstellar dust grains, because the scattering phenomena is the most efficient where its size is comparable to the wavelength of scattered light. To date, measurements of DGL were mostly carried out only in optical wavelength range, however they are insufficient to understand the optical properties of interstellar dust grains.

In this study, we have conducted near-infrared observations of diffuse clouds in high Galactic latitude ($|b| \sim 40$ °) at I-band (1.1 μm) and H-band (1.6 μm), and obtained high quality photometric data with a wide-field imager ($\sim 3.67 \times 3.67$ deg^2) onboard Korean space telescope so-called Multi-purpose Infra-Red Imaging System (MIRIS), with the best accuracy sufficient to discuss on size of interstellar dust grains. Since the starlight is not only scattered but also absorbed by interstellar dust and re-emitted in the far-infrared, the near-infrared brightness correlates well with the far-infrared one. Thus, the DGL brightness was derived by correlating the near-infrared brightness with the far-infrared brightness observed with *IRAS* and DIRBE/*COBE* in a wide density range from blank field to dense dust cloud. In addition, by correlating the near-infrared brightness with the optical brightness taken from existing optical images, we derived an optical to near-infrared spectrum of DGL.

The derived DGL at 1.1 μm and 1.6 μm are different among the three observed field, which means the scattering property of interstellar dust grains is different even in similar Galactic latitude. To investigate the size of interstellar dust grains in detail, we firstly compared our result with model spectra of DGL which is generated by applying the conventional interstellar dust models incorporating sub-micrometer sized grains. However, the model spectra shows significantly bluer color than the measured DGL's even though anisotropic effect on scattering is taken into account.

One possibility of discrepancy is underestimation of albedo in the dust models. In fact, higher near-infrared albedo has been suggested for several Galactic regions. Moreover, measurements of interstellar extinction curve universally exhibited a flatter shape in 3–8 μm than the predicted one from the conventional dust model. These studies imply the existence of larger size grains than the models consider. Therefore, we need to improve the dust models with reconsideration of size distribution of interstellar dust.

In order to explain the measured DGL spectrum, we extended a popular existing dust model by invoking a population of micrometer sized grains (up to $\sim$ 10 μm), and calculated the albedo and DGL spectrum concurrently taking account of the effects on the interstellar extinction curve, the thermal emission in the far-infrared and sub-milimeter wave. The predicted thermal emission and interstellar extinction were found to be consistent with the *Planck* observations and extinction curve. By the created models with a population of micrometer sized grains, DGL spectra is also calculated with two scattering models. One is the isotropic scattering model, and the another is anisotropic one that the dust grains are illuminated by an infinite homogeneous disk. Comparing with measured DGL, isotropic scattering model with micrometer sized grains is more favorable to explain the measured near-infrared DGL color (1.1 μm to 1.6 μm). This model also mostly agrees with optical to near-infrared color of DGL.

High photometric accuracy of our data also allowed us to apply the dark cloud method to constrain the Extragalactic Background Light (EBL) which is the integrated light from extragalactic sources. The dark cloud method is one observation technique which is advantageous for eliminating uncertainty of the Zodiacal Light (ZL) foreground by using the screening effect by a diffuse cloud to subtract the foreground. By applying dark cloud method, we obtained 1σ upper limit of the EBL brightness of 38.2 nW m^{-2} sr^{-1} at 1.1 μm, corresponding to the allowable minimum albedos. In other words, by assuming the integrated Galactic light from deep galaxy counts as the lower limit of EBL brightness, we determined the maximum albedo of the interstellar dust to be 0.7 at 1.1 μm, which is consistent with that from our created dust model with micrometer sized grains.

Contents

Chapter 1

Introduction

1.1 Diffuse sky brightness in optical to near-infrared

In modern astronomy and cosmology, astronomical diffuse components are becoming hot topics. For example, scattered light by interstellar dust grains informs us about dust properties and radiation field incident on the dust grains. Another essential topic is diffuse extragalactic background light (EBL) which represents total brightness of the light coming from outside of our Galaxy. The EBL records the total photon energy released by stellar nucleosynthesis or, any radiation emitting process throughout the cosmic history. Thus it gives us crucial information about star formation and structure evolution history in the universe.

In optical to near-infrared wavelength range, several astronomical components contribute to the diffuse brightness of the sky (I_{sky}).

- Zodiacal Light (I_{ZL}), scattered sunlight and thermal emission from interplanetary dust particles.
- Integrated starlight (I_{ISL}) from unresolved galactic sources.
- Diffuse Galactic Light (I_{DGL}), scattered starlight by interstellar dust grains.
- Extragalactic Background Light (I_{EBL}), integrated light of extragalactic objects.

The spectra of these diffuse radiation are shown in Figure 1.1, and the total diffuse sky brightness I_{SKY} is expressed as follows,

$$I_{sky} = I_{ZL} + I_{ISL} + I_{DGL} + I_{EBL} \tag{1.1}$$

Among these components, we mainly focus on the DGL and the EBL. The study of DGL allows us to understand the properties of interstellar dust grains. In addition, dust properties give us a clue to understand its origin and evolution history. On the other hands, one of the important questions for cosmology is the absolute brightness level of EBL. If it would be precisely measured, it can constrain the models of galaxy formation and evolution by providing an anchor that connects the overall radiation energy density to star formation and metal production history.

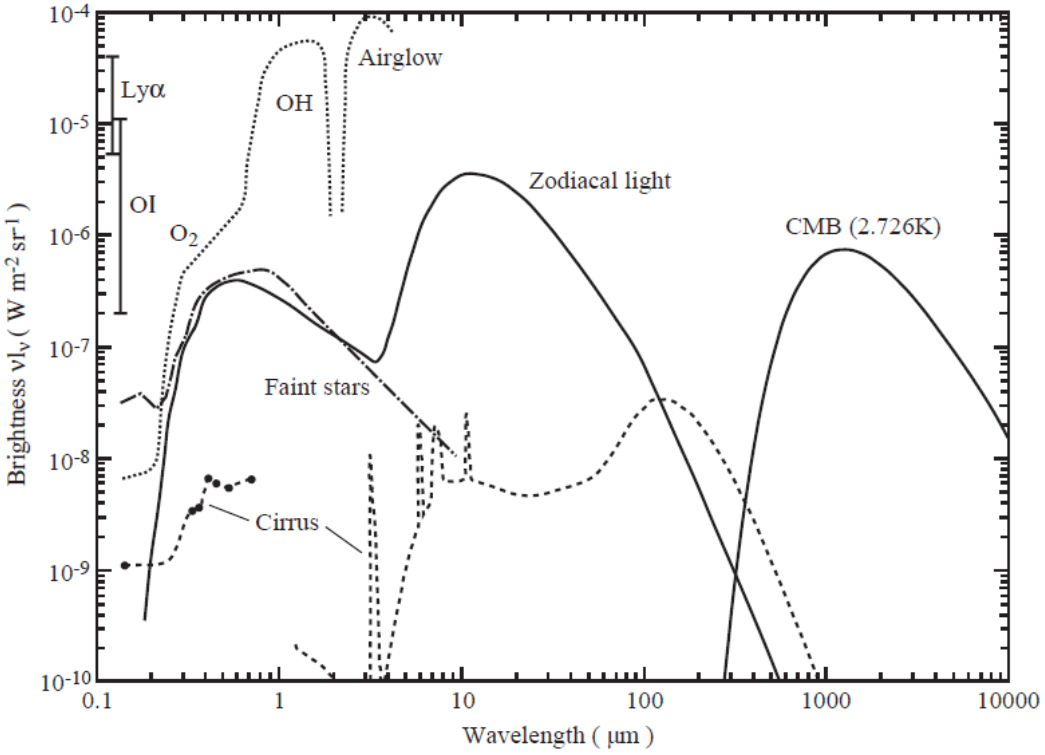

Figure 1.1 Overview on the brightness of the sky seen from outside the lower terrestrial atmosphere and at high ecliptic and galactic latitudes (Leinert et al. 1998). The zodiacal emission and scattering as well as the integrated light of stars are given for the South Ecliptic Pole ($l = 276°, b = -30°$). The bright magnitude cutoff for the stellar component is $V = 6.0$ mag for 0.3 - 1 μm. In the infrared, stars brighter than 15 Jy between 1.25 and 4.85 μm and brighter than 85 Jy at 12 μm are excluded. No cut-off was applied to the UV data, $\lambda \leq 0.3$ μm. The interstellar cirrus component is normalized for a column density of 10^{20} H-atoms cm^{-2} corresponding to a visual extinction of 0.053 mag. This is close to the values at the darkest patches in the sky. Source for the long-wavelength data, $\lambda \geq 1.25$ μm, are DIRBE/*COBE* and FIRAS measurements as presented by Désert et al. (1996). The IR cirrus spectrum is according to the model of Desert et al. (1990) fitted to the *IRAS* photometric data. The short-wavelength data, $\lambda \leq 1.0\mu$m, are from the following sources: zodiacal light: Leinert et al. 1990; integrated starlight: $\lambda \leq 0.3$ μm, Gondhalekar et al. (1990), $\lambda \geq 0.3$ μm, Mattila et al. (1980); cirrus: $\lambda = 0.15$ μm, Haikala et al. (1995), $\lambda = 0.35 - 0.75$ μm, Mattila et al. (1990b), Mattila et al. (1979). The geocoronal Lyman α(121.6 nm) and the OI(130.4, 135.6 nm) line intensities were as measured with the Faint Object Camera of the Hubble Space Telescope at a height of 610 km Caulet et al. (1994).

1.2 Zodiacal Light

In optical to near-infrared wavelength, the Zodiacal Light (hereafter ZL) is dominated by scattered sunlight by interplanetary dust (IPD) particles in zodiacal cloud. In mid-infrared to far infrared, the ZL is dominated by the thermal emission from IPD particles. Thus, the spectral energy distribution of ZL has two peaks as shown in Figure 1.1.

On the other hand, because IPD smoothly distributes mainly on the symmetry plane, which is slightly inclined to the ecliptic plane due to the Jupiter orbit, the ZL brightness is expressed as a function of heliocentric distance, position of the observer relative to the symmetry plane of interplanetary dust, and viewing direction ($\lambda - \lambda_\odot$, β), where λ presents an ecliptic longitude, $\lambda_\odot$ is an ecliptic longitude of the Sun, and β is an ecliptic latitude.

Observations of ZL are mainly motivated by the cosmological studies via EBL, because it dominates the diffuse sky brightness and contaminates the EBL measurement as shown in Figure 1.1. At present, the overall brightness distribution of ZL was determined almost completely, with the largest sky coverage in the optical. The infrared maps of ZL obtained by the the Diffuse Infrared Background Experiment (DIRBE) onboard the Cosmic Background Explorer (*COBE*) provided excellent data, with relative accuracies of 1% to 2% at least for the wavelengths between 1.25 and 100 μm. Thanks to DIRBE/*COBE* observation, two popular ZL models are developed in Kelsall et al. (1998) and Wright (1998). The brightness of ZL at (r_h, β') is calculated by integrating the scattered light from IPD particles with number density n_c corresponding to component c along a line of sight as follows:

$$I_{ZL} = \sum_c \int_0^\infty n_c\left(r_h, \beta'\right) \left[F_\odot \left(\frac{r_h}{r_0} \right)^{-2} \langle \sigma_{sca} \rangle \, \Phi\left(\theta\right) + \langle \sigma_{abs} \rangle \, B\left(T\right) \right] dl \tag{1.2}$$

where dl is line element, $F_\odot$ is the solar flux, r_0 is the heliocentric distance, $\langle \sigma_{sca} \rangle$ is the mean total scattering cross section of IPD, $\langle \sigma_{abs} \rangle$ is the mean total absorption cross section of IPD, $\Phi\left(\theta\right)$ is the mean volume scattering phase function, and $B(T)$ is the planck function. The first term denotes the scattering component, the second term denotes the thermal emission component by IPD. The geometry and the notations are summarized in Figure 1.2.

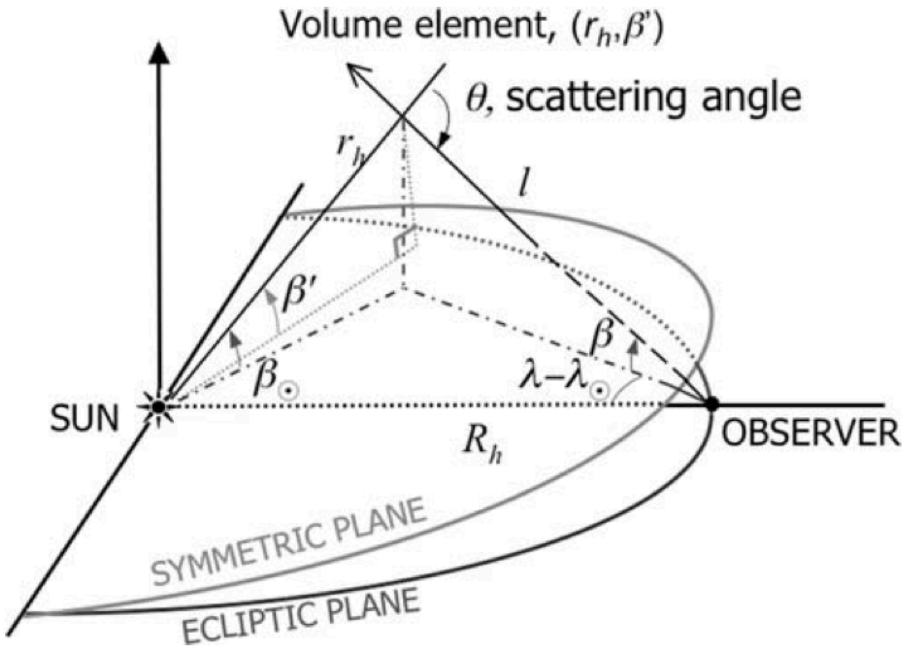

Figure 1.2 The viewing geometry for light scattering by a dust volume element (Ishiguro et al. 2007). The scattering angle θ is defined as an angle between the line toward the observer and the anti-solar direction at the volume elements.

Table 1.1 ZL brightness from the earth for a viewing direction parallel to the ecliptic plane at elongation $\sim 90°$. (Leinert et al. 1998)

λ	$I_{ZL}(\lambda)$	
(μm)	(10^{-7} W m^{-2} sr^{-1} μm^{-1})	(MJy sr^{-1})
0.2	0.25	0.00036
0.3	5.3	0.017
0.4	22	0.13
0.5	26	0.23
0.7	20	0.35
0.9	13	0.38
1.0	12	0.43
1.2	8.1	0.42
2.2	1.7	0.28

1.3 Integrated starlight

Integrated starlight (hereafter ISL) is diffuse emission from unresolved galactic sources, with the contribution being dominated by hot stars and white dwarfs at the shortest wavelengths, main sequence stars at optical wavelengths, and red giants in the infrared (Mathis et al. 1983). The contribution of ISL depends on the sensitivity of observation; e.g., detection limit for stars which can be spatially resolved in the sky, and type/number of stars in the line of sight. If we assume that stars brighter than flux F_0 are resolved and excluded from the diffuse sky brightness, then the ISL contribution is integral of the fluxes from stars fainter than F_0 over the line of sight:

$$I_{ISL} = \int_0^{F_0} F \frac{dn\,(l,b)}{dF} dF \tag{1.3}$$

where $\frac{dn(l,b)}{dF}dF$ is the number of stars in the flux range F to $F+dF$, for a line of sight towards galactic coordinates (l, b). When the instruments can sufficiently resolve stars, the ISL contribution is negligible compared to the other diffuse components (EBL and DGL). In appendix of this thesis, we will show the result of calculation of ISL at 1.1 and 1.6 μm towards galactic latitude $|b| \sim 40°$. The derived contribution of ISL is a few nW m^{-2} sr^{-1}, which is half or lower than EBL and DGL.

1.4 DGL

The DGL is scattered emission component from interstellar dust grains illuminated by interstellar radiation field. Since DGL is a foreground, contaminating emission component for the EBL measurement, we need to discreetly estimate and separate the contribution of DGL for the precise measurement of EBL. In addition, the evaluation of DGL is important to reveal the properties of interstellar dust grains such as its size distribution and composition. The DGL is the most intense in directions where the dust column density and the interstellar radiation field are both highest. Assuming the interstellar radiation field is isotropic, an intensity of the DGL (I_{DGL}) towards the direction with the optical depth τ can be written by (Henyey 1937):

$$I_{DGL} = \frac{\gamma}{1-\gamma} I_{ISRF} \left[1 - e^{-(1-\gamma)\tau}\right] \tag{1.4}$$

where I_{ISRF} is the intensity of interstellar radiation field, γ represents the albedo (dimensionless value) which is defined by the ratio of scattering cross section to total extinction (scattering + absorption) cross section of dust grains.

1.5 Historical studies on interstellar dust

1.5.1 Measurements of DGL

Initial studies (e.g., Elvey & Roach 1937; Henyey & Greenstein 1941; van de Hulst & de Jong 1969; Elsasser & Haug 1960; Wolstencroft & Rose 1966; Mattila 1979) revealed that DGL is a scattered emission component from interstellar dust grains illuminated by interstellar radiation field in the optical to near-infrared wavelengths.

After a few decades from those studies, diffuse far-infrared emission so-called IR-cirrus was discovered by Low et al. (1984) by using Infrared Astronomical Satellite (*IRAS*). From the *IRAS* data, de Vries & Le Poole (1985), Laureijs et al. (1987) suggested that 100 μm brightness is remarkably linear to extinction in a range of up to ~ 20 MJy sr^{-1} and indicated that starlight coming from interstellar radiation field is not only scattered but also absorbed by the interstellar dust and re-emitted in the far-infrared. It is thus natural to expect a linear correlation between the DGL and the far-infrared brightness in the optically thin limit. This discovery also suggests that a combination of optical/near-infrared and far-infrared observations would give a powerful tool for investigating the dust properties. At present, 100 μm all-sky map is published with the efforts of Schlegel et al. (1998), by combining *IRAS* and DIRBE data.

For many years, with the correlation analysis between optical and far-infrared, measurements of DGL have been carried out vigorously to investigate the composition, size, and optical properties of interstellar dust grains.

Guhathakurta & Tyson 1998 observed the edge of four high Galactic latitude clouds ir1 ($l = 174°, b = -42°$), ir2 ($l = 235°, b = 37°$), ir3 ($l = 38°, b = 45°$), and ir4 ($l = 72°, b = 25°$) with three bands (B_J, R, and I-band). The bright stars were clipped out of the image and the faint stars were cleaned by replacing them with the local value of sky images. The images were smoothed to an angular resolution of FWHM of *IRAS* high quality maps in order to find a correlation between the optical and far-infrared images. However, they did not show a clear correlation between the optical and far-infrared brightness.

Zagury et al. (1999) observed a high Galactic latitude cloud MCLD123.5+24.9 ($l = 123.5°, b = 24.9°$) located in the large infrared cirrus known as the Polaris Flare. They observed the cloud with a CCD with B, V, and R filters. The stars

and galaxies on the optical images were subtracted from each image and replaced by an interpolation. Then, in order to compare the optical and *IRAS* 100 μm map, the optical images were smoothed to *IRAS* resolution. They also showed that the optical brightness, colors, and the surface brightness ratios between the optical and the far-infrared can be explained by forward scattering of Polaris light.

Witt et al. (2008) observed five high Galactic latitude clouds MBM25 ($l = 173.8°, b = 31.5°$), MBM30 ($l = 142.2°, b = 38.2°$), MBM32 ($l = 147.2°, b = 40.7°$), 41A ($l = 90.0°, b = 39.0°$), and 41D ($l = 92.3°, b = 37.5°$) at *B, G, R*, and *I*-band. By comparing to the 100 μm map, they found a linear correlation between the surface brightness of the optical and that of the 100 μm.

Matsuoka et al. (2011) performed a correlation analysis for the high-latitude sky ($|b| > 35°$) by using the diffuse emission map created by *Pioneer* 10/11 at 0.44 μm and 0.64 μm and the 100 μm map. Brandt & Draine (2012) derived an optical DGL spectrum by correlating optical and far-infrared emissions from 92,000 blank sky images obtained by the Sloan Digital Sky Survey (York et al. 2000). Ienaka et al. (2013) carried out a ground-based observation of the dark cloud MBM32 at a high Galactic latitude in four optical bands (B, g, V, and R-bands). Previous measurement of optical DGL summarized in Figure 1.3. However, as shown in Figure 1.3, without data at various wavelength bands including the near infrared, it is difficult to understand the dust grain properties.

However, only a few observations have been carried out at near-infrared wavelengths so far. Tsumura et al. (2013b) produced a continuous DGL spectrum at low Galactic latitude regions ($5° < |b| < 15°$) from 1.8 to 5.3 μm using IRC/*AKARI*. Sano et al. (2015; 2016a) also derived DGL using all-sky maps obtained from DIRBE/*COBE* at 1.5, 2.2, 3.5, and 4.9 μm. In a range of 0.95 to 1.65 μm, Arai et al. (2015) measured a continuous spectrum of DGL in several regions at a high Galactic latitude ($|b| > 30°$) using the Low-Resolution Spectrometer (LRS) on the sounding rocket-borne Cosmic Infrared Background ExpeRiment (CIBER), which was designed to measure the absolute EBL spectrum. However, because of the uncertainties of near-infrared measurements of DGL, size distribution and composition are still under discussion. Thus, it should be noted, however, in order to determine the size distribution, it is essential to obtain wealth information about optical properties of dust grains, for which derivation of an accurate DGL spectrum over a wide range from optical to near-infrared will play a key role.

1.5.2 Dust models

The model for interstellar dust has been developed by some authors (e.g., Weingartner & Draine 2001; Zubko et al. 2004; Draine & Fraisse 2009). The WD01 model consists of graphite, silicate, and polycyclic aromatic hydrocarbon (PAH) material, while the dust composition of the ZDA04 model consists of bare graphite and bare silicate grains and PAHs. The size distribution of the ZDA04 model was shifted to a smaller grain size than the WD01 model: the half-mass grain radius was $a_{\rm dust} \sim 0.12$ μm for both silicate and carbonaceous grains in the WD01 model, while in the ZDA04 model $a_{\rm dust} \sim 0.06$ and 0.07 μm for graphite and silicate grains, respectively. They tried to make the model of dust composition, abundance, and size by fitting to observed values e.g., interstellar extinction. The interstellar extinction is a reliable index to constrain on the properties of interstellar dust grains. Since a dust grain absorbs and scatters light most effectively at wavelengths comparable to its size $\lambda \approx a$, the wavelength dependence of extinction $A(\lambda)$ in units of magnitudes so-called "extinction curve" which can constrain the dust size distribution. Moreover, extinction curve reflects the features of dust components, e.g., 2175 Å feature of graphite grains. Thus, the dust abundance is constrained by shape of the features.

The standard interstellar extinction curve is normalized in terms of $E(B-V)$ which is defined by $E(B-V) = A(B) - A(V)$, where $A(B)$ and $A(V)$ indicate the extinction at B-band ($\lambda = 0.43$ μm) and V-band ($\lambda = 0.55$ μm). If the interstellar extinction curve has a universal form, there will be a simple relation between $E(B-V)$ and the total extinction at a specific wavelength for example, $A(V)$. Conventionally, we define this in terms of the parameter R_V which indicates the ratio of total to selective extinction: $R_V = A(V)/E(B-V)$. Usually we can specify the interstellar extinction law by adopting one from two typical values for R_V:

- $R_V = 3.1$, typical value of the local diffuse clouds.
- $R_V = 5$, typical value of dense clouds nearby Galactic-center.

Different values of R_V obviously must have either different compositions or different size distributions, or both of them.

By fitting to observed extinction in the range from UV to near-infrared, the conventional dust models include the composition (graphite and silicate grains) and the size distribution; which is dominated by sub-micrometer sized grains which follows

the power-law size distribution $dn/da \propto a^{-\alpha}$. Old study of Mathis et al. (1977) so-called MRN showed that models using silicate and graphite spheres with power-raw size distribution of $\alpha = 3.5$.

Using dust models, Brandt & Draine (2012) generated the model spectra of DGL in an infinite plane-parallel galaxy model and using a stellar emission spectrum (Mathis et al. 1983) that reproduces the local interstellar radiation field (ISRF) of MMP83 and the stellar population synthesis model of Bruzual & Charlot (2003) (BC03) with solar metallicity and a star formation rate of $\propto \exp(-t/5\mathrm{Gyr})$, where t denotes the timescale in units of Gyr. The model spectra by Brandt & Draine (2012) is shown in Figure 1.3.

The conventional dust models are successful to reproduce the interstellar extinction curve from UV to near-infrared, however, there are some issues conflicting with observations. One is the discrepancy of grain albedo in the near-infrared. Their dust models predict that the albedo at near-infrared wavelength range is about 0.4. In contrast, high near-infrared albedo over 0.6 has been reported (Witt et al. 1994; Block 1996; Lehtinen & Mattila 1996). Another issue is incompleteness of the extinction in mid-infrared wavelength range. Recent measurement of extinction in Galactic center (Lutz 1999; Nishiyama et al. 2009), the Galactic plane (Indebetouw et al. 2005; Jiang et al. 2006; Gao et al. 2009), the Coalsack nebula (Wang et al. 2013), and nearby star-forming regions (Flaherty et al. 2007) appear to suggest that mid-infrared (3–8 μm) extinction has a flat structure, although conventional dust models (e.g., Weingartner & Draine 2001) predicts a power-law extinction curve of $A(\lambda) \propto \lambda^{-1.75}$ at 1–7 μm as shown in Figure 1.4. These facts imply the existence of larger dust grains than the model prediction.

Finally, we note that micrometer-sized grains were detected in dense cloud cores through the scattering of the interstellar radiation at the *Spitzer*/IRAC 3.6 and 4.5 μm bands (Pagani et al. 2010, Steinacker et al. 2014).

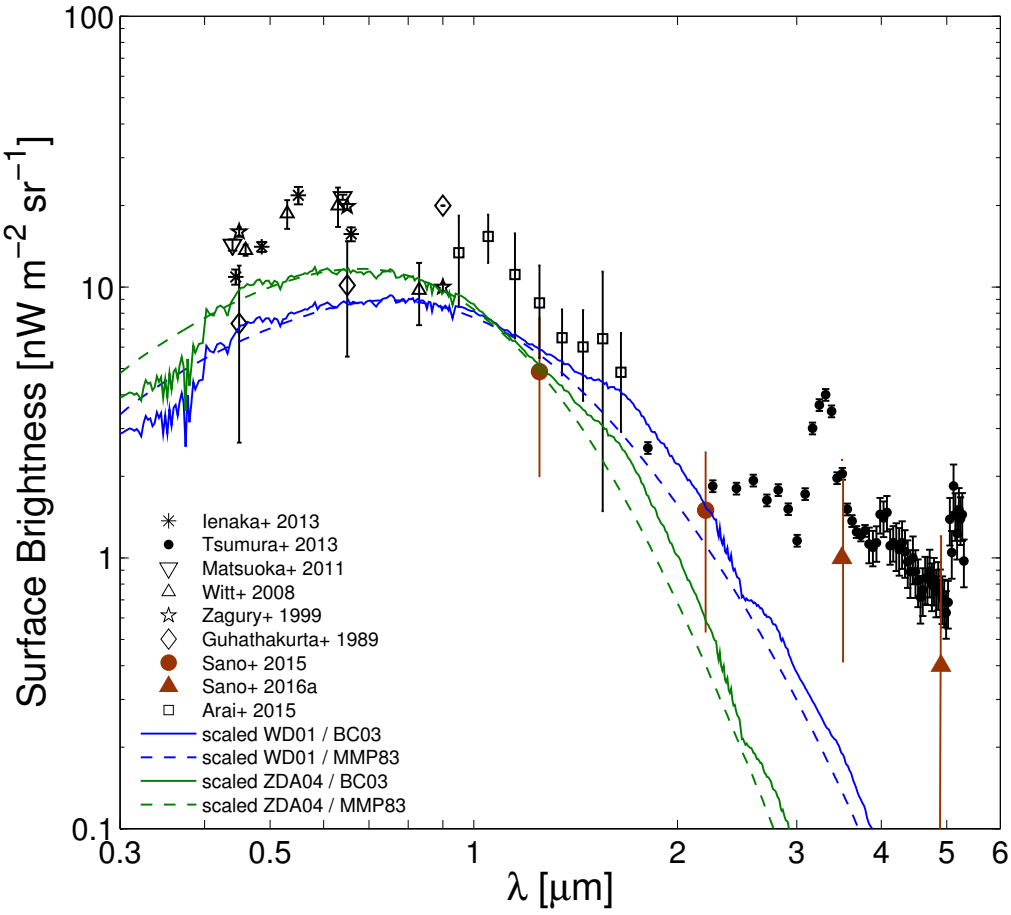

Figure 1.3 Previous measurements of DGL from optical to near-infrared wavelength range, which is normalized by 100 μm brightness of 1 MJy sr^{-1}. The red solid curve and the orange dashed curve indicate the model spectrum of DGL by Brandt & Draine (2012) for typical dust sizes 0.12 and 0.06 μm, respectively.

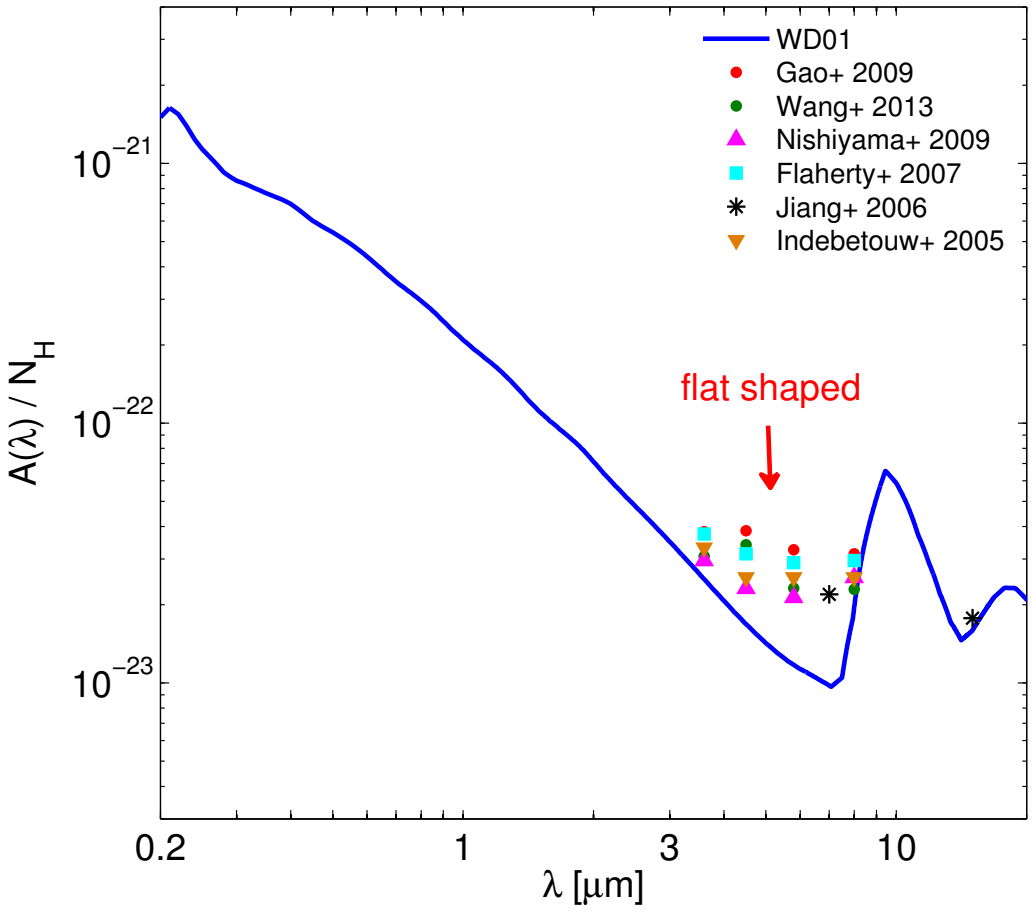

Figure 1.4 The interstellar extinction. The blue thick curve is the extinction curve predicted from WD01 for R_V=3.1. The colored points are the measured extinction at 3.6, 4.5, 5.8, 8.0 μm which show a universally flat structure.

1.6 EBL

One major question in modern cosmology is to reveal how the various structure in the universe has been formed and evolved. After the epoch of recombination, there is no luminous object like stars and galaxies in the universe and this stage is called Dark Ages. After a few million years, super massive first stars were born in the hydrogen gas to illuminate the universe and terminate the Dark Ages. This stage is generally called Cosmic Dawn which is an important stage to reveal the structure evolution as the beginning point of star formation and galaxy formation history. The simplest and the most direct way to understand the star formation history is to observe the early stage of the universe. However, the distance to first luminous objects are too much distant to be detected. The only possible way for us to detect the light from the early universe is to measure the Extragalactic Background Light (EBL) which is the integrated light from extragalactic sources. Intensity of the EBL I_{EBL} can be written by

$$I_{EBL} = \frac{c}{4\pi} \int_0^\infty \frac{L\left(z\right)}{H_0 \left(1+z\right) \left[\Omega_m (1+z)^3 + \Omega_\lambda\right]^{1/2}} dz \tag{1.5}$$

where $L\left(z\right)$ is comoving specific luminous density for any redshift z, H_0 is Hubble constant of 67.2 $\pm$ 1.2 km s^{-1} Mpc^{-1}, c is the velocity of light, Ω_m and Ω_λ present the cosmological density parameters for the matters and the dark energy.

The EBL contains the all the light generated through the physical process in stars between Cosmic Dawn and the present day, it is an important tool to resolve star formation history and the various radiation processes occurring throughout the cosmic history. Many cosmologists are vigorously trying to reveal the cosmic history from theoretical or observational studies of EBL in various electromagnetic wavelengths from X-rays to sub-millimeter.

1.7 Previous measurements of EBL

Observations of DIRBE/*COBE* revealed the total EBL brightness in the near-infrared after direct subtraction of the ZL and other foreground components. The EBL brightness obtained was found to significantly exceed the integrated flux of the known galaxy counts (e.g., Hauser et al. 1998; Wright 2001; Cambrésy et al. 2001, and Sano et al. 2015). Matsumoto et al. (2005; 2015) and Tsumura et al. (2013a) mea-

sured near-infrared EBL spectrum by using the Infrared Telescope in Space (*IRTS*) and the Infra-Red Camera (IRC) onboard the *AKARI* satellite, respectively. Particularly in the optical to near-infrared wavelength range, EBL was found to have an excess component a few times higher than the known galaxy counts.

In addition to direct measurements, indirect derivation of EBL brightness by observation of the spectrum of blazars emitting γ-rays has been carried out (e.g., Guy et al. 2000; Dwek et al. 2005b; Schroedter 2005; Aharonian et al.2006; Albert et al.2008; Mazin & Raue 2007; Orr et al. 2011; Meyer et al. 2012). As γ-rays are attenuated through interaction with EBL photons in intergalactic space, EBL intensity can be derived by assuming an intrinsic blazer spectrum. The results of these studies indicate that EBL brightness is comparable to known galaxy counts.

This discrepancy in EBL brightness under different observational methods can be attributed to the need to insufficient knowledge to accurately subtract the contribution of the ZL, which is roughly ten times brighter than EBL. The ZL subtraction is performed using the model developed by Kelsall et al. (1998), which is based on all-sky observations by DIRBE/*COBE* over ten months. The model includes a 5% uncertainty, which significantly contributes to the resultant EBL uncertainty. Therefore, to measure the actual brightness and investigate the origin of the excess emission, it is ideal to take an observational method in which the uncertainty involved in subtracting the ZL is removed.

One observational technique that is independent of ZL subtraction is the dark cloud method, which utilizes the screening effect of dark clouds to spatially isolate all foreground contributions from the background. The resulting difference in surface brightness between a dark cloud and its neighboring blank sky will therefore be a direct measure of EBL and diffuse galactic light (DGL), and most ZL contributions, as well as faint Galactic starlight (e.g., ISL), can therefore be eliminated. Mattila (1976) introduced this method for the first time and measured the dark cloud LDN 134 by using a ground-based telescope. As LDN 134 is located at a high galactic latitude ($l = 4^\circ$, $b = 36^\circ$), galactic emission was minimized and the cloud was opaque enough to shield the background light. The derived value of EBL brightness was 92 ± 32 nW m^{-2} sr^{-1} at 0.40 μm, which was unexpectedly higher than the extragalactic count and the previously derived upper limits of EBL because the data were contaminated by strong terrestrial airglow and a bright source was present in the cloud. Mattila et al. (2011) used the dark cloud method to produce new EBL values

(6.4 ± 2.0 nW m^{-2} sr^{-1} at 0.4 μm and < 8.3 nW m^{-2} sr^{-1} at 0.52 μm) by using data from the European Space Observatory's Very Large Telescope. The result of previous EBL measurements are shown in Figure 1.5.

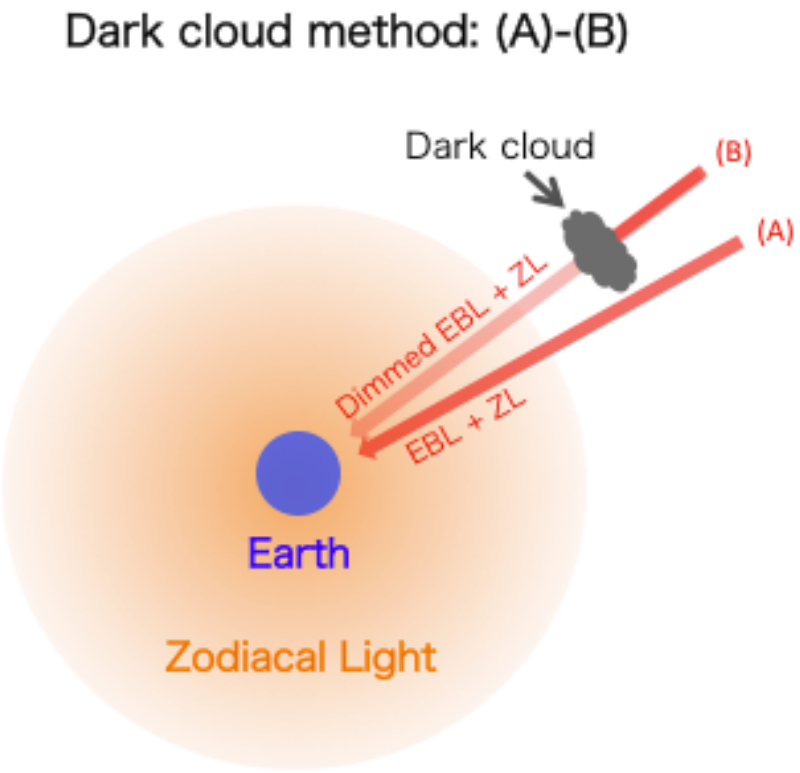

Figure 1.5 Conceptual diagram of EBL measurement using dark cloud method.

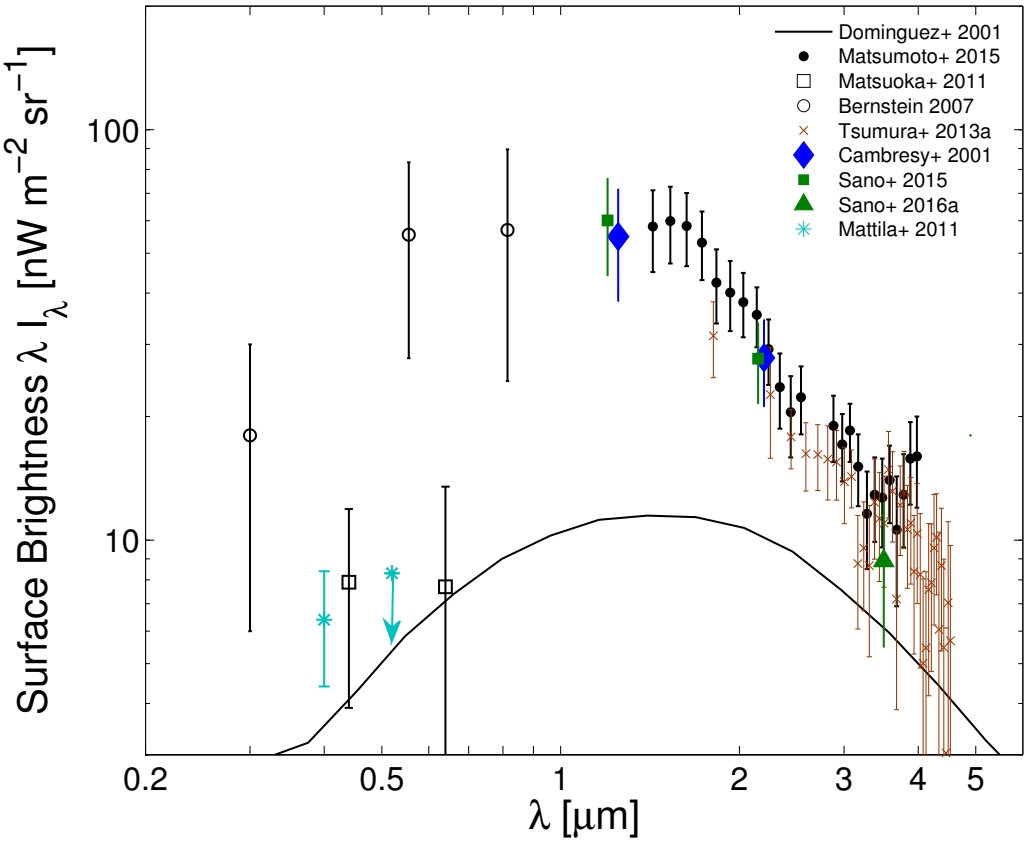

Figure 1.6 Previous measurement of EBL from optical to near-infrared wavelength range. The black solid spectrum indicates known galaxy counts by Domínguez et al. (2011). The cyan asterisk points indicate the measurement by Mattila et al. (2011) using dark cloud method.

1.8 Purpose and outline of this thesis

As described in previous section, it is necessary to obtain wealth spectral information of DGL in order to develop the study of interstellar mediums. The main purpose of this thesis is to derive an accurate spectrum of the DGL over a wide wavelength range from optical to near-infrared and improve our knowledge on properties of interstellar dust.

Secondary, near-infrared EBL is expected to contain the crucial information about star formation history in the universe. However, the direct measurement of near-infrared EBL has ever been suffered from the contribution of ZL. Thus, we need to derive the brightness of EBL without the subtraction of ZL foreground. For this purpose, we utilized the screening effect of diffuse cloud so-called dark cloud method and aim at the first detection of near-infrared EBL at 1.1 and 1.6 μm without ZL uncertainty.

In chapter 2, we provide pieces of the information about telescopes and observed targets. To make an accurate measurement of DGL and EBL, we utilized the wide-field imager (3.67×3.67 deg^2) onboard the Korean space telescope so-called Multi-purpose Infra-Red Imaging System (MIRIS) (Han et al. 2014).

In chapter 3, we present the reduction process of the MIRIS data. The process includes flux calibration of instruments, and a few more process to separate the diffuse emission from the obtained images.

In chapter 4, we describe the analysis method to derive the DGL spectrum. To derive the near-infrared DGL, we correlated the MIRIS data with the 100 μm intensity map. Furthermore, to derive the global DGL spectrum from optical to near-infrared, we correlated the MIRIS data with the optical dataset which was obtained by Ienaka et al. (2013).

In chapter 5, we discuss on previous and current DGL result, especially related to the size distributions of interstellar dust grains by providing diagnostic tests for a popular dust model (Weingartner & Draine 2001). For further discussion, we derived the albedos of interstellar dust grains, using our DGL spectrum.

In chapter 6, we present the result of EBL measurement using dark cloud method, and discuss on origin of near-infrared EBL in comparison with the other studies and measurements of EBL.

Chapter 2

Observations

2.1 Observational design

As described in the previous chapter, we need a precise measurement of the DGL in order to investigate the scattering properties of interstellar dust, and a measurement of near-infrared EBL with precise subtraction of ZL is needed to constrain the star formation history in the universe. For precise detection of the faint diffuse emissions such as DGL and EBL, we need a wide-field observation by space near-infrared telescope. Furthermore, for the accurate determination with using the intensity correlation analysis with far-infrared data, we need large area images with sufficient spatial resolution. To satisfy these requirement, we chose the Multi-purpose Infra-Red Imaging System (MIRIS) which has been developed by the Korea Astronomy and Space Science Institute (KASI) whose Field of View (FOV) is 3.67×3.67 deg^2 with high spatial resolution ($\sim 1'$pixel^{-1}), which is sufficient to measure the near-infrared DGL with the best ever accuracy, and to attempt the dark cloud method in near-infrared wavelengths. Assuming the use of the MIRIS telescope, we selected the observation targets to achieve the purpose of our thesis work as following conditions.

- (1) Clouds are sufficiently apart from Galactic center, and Galactic plane.
- (2) Extinction of the clouds is large enough to shield the background radiation.
- (3) Clouds are compact, in a degree scale.

The condition (1) is to minimize the contamination of Galactic stars. In order to satisfy the condition (1), we selected the clouds which locates on $120^\circ < l < 240^\circ$

and $|b| > 30°$. In these coordinate, the contribution of galactic stars is roughly 400 nW m^{-2} sr^{-1} at J-band, but the total brightness of the stars which are fainter than limiting magnitude of MIRIS is less than 10 nW m^{-2} sr^{-1}.

To satisfy the condition (2), we found the molecular clouds with strong far-infrared emission of 10 MJy sr^{-1} which corresponds to usual optical depth $\tau_V \sim 1$ with the 100 μm intensity map based on the observation by *IRAS* and DIRBE/*COBE*.

The condition (3) is to avoid from the gradient of the ZL. ZL is known to be uniform on spatial scales smaller than a degree. However, because of large FOV of MIRIS, we had better to remove the large-scale spatial gradient of the Zodiacal Light for the evaluation of DGL.

Under these criteria, we selected two clouds which are named CIBDC 3 and CIBDC 5, respectively. And we adopted the field named MBM 32 where the analysis of the optical DGL was made in Ienaka et al. (2013) in order to determine the color of DGL between near-infrared and optical. Theme of the thesis with DGL and EBL measurement by using these dark clouds were not initially included in the observation project of MIRIS. Moreover, the data were not archived yet, and were under the reduction. Therefore, in order to achieve the purpose of the thesis work, I proposed the observation program to the MIRIS team. The use of the MIRIS telescope was approved willingly by KASI, and our three targets CIBDC 3, MBM 32, and CIBDC 5 were successfully observed in Jan 13, 2015, Feb 25, 2015, and Mar 20, 2015, according to the visibility of them. The status of three selected fields is shown in Table 2.1, and the images of the dark clouds captured by MIRIS are shown in Figure 2.1.

Table 2.1 Status of our target, (λ, β) and (l, b) indicate ecliptic and galactic coordinates respectively. Maximum brightness of SFD 100 μm in MIRIS FoV is also presented.

Field name	Date of the observation	Exposure time [sec]	(λ, β) [deg]	(l, b) [deg]	$I_{100\mu\mathrm{m}}$ [MJy sr^{-1}]
CIBDC 3	Jan 13, 2015	340	(41.01, 2.04)	(154.60, -39.70)	≤ 14.69
MBM 32	Feb 25, 2015	340	(119.06, 47.61)	(147.16, 40.62)	≤ 7.95
CIBDC 5	Mar 20, 2015	340	(115.17, 52.49)	(140.98, 38.21)	≤ 10.01

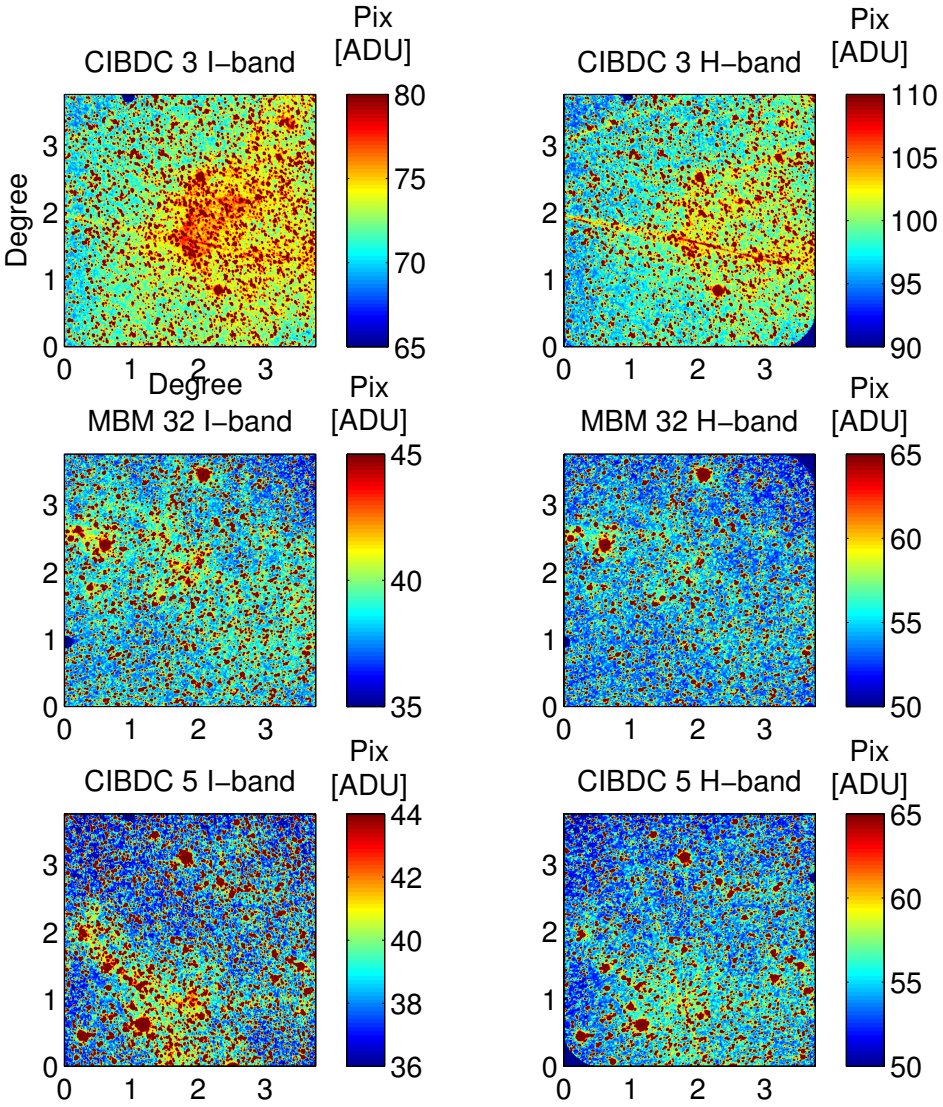

Figure 2.1 The I and H-band images of our targets obtained by MIRIS.

2.2 Multi-purpose Infra-Red Imaging System (MIRIS)

MIRIS has been developed by the Korea Astronomy and Space Science Institute (KASI), and launched onboard the Science and Technology Satellite-3 of Korea (STSAT-3) in 2013 November. STSAT-3 is operating in Sun-synchronous orbit with an altitude of around 600 km and maintains high Sun and Earth avoidance angles of more than 90° for as long as possible during each orbit by controlling the satellitefs attitude. In June 2015, MIRIS observation is terminated due to the lifetime of cooling system.

Primary purposes of MIRIS are the survey of Paschen-α emission line coming from the Galactic plane and detecting EBL at high Galactic latitude. The optical design of MIRIS was optimized for a wide-field survey in near-infrared wavelengths.

MIRIS telescope is designed with a wide-field, F/2 refractive optics using 80 mm diameter aperture. The structure of MIRIS telescope is shown in Figure 2.2, it consists of a radiator, a Winston cone baffle, a sunshade, a thermal-shield box, the Glass Fiber Reinforced Plastic (GFRP) pipe support, 30 layers of Multi-Layer Insulation (MLI), a cryostat, a filter-wheel, and a micro cooler. The MIRIS optics consists of five lenses, among which the rear surface of the fifth lens is aspheric. The detector module in a cryostat was designed to be cooled down to around 90 K by a micro Stirling cooler (Ricor K508 model) at the passive cooled space environment consuming minimum power.

MIRIS performs observation by two broad-bands I-band (1.076 μm), H-band (1.608 μm) and three narrow-bands composed by Paschen-α line band (1.876 μm) and dual band Continuum (1.84μm, 1.91 μm) which are mounted on a filter-wheel such as Figure 2.3, and employed a 256×256 PICNIC HgCdTe sensor array, providing a $3.67^\circ \times 3.67^\circ$ Field of View (FOV) with a pixel scale of 51.6 arcsec, and the detector reads their count at specified intervals of ~ 2 sec while the reset is commanded (The reset interval is 10 frames). From each pointed observation, we obtain about 200 images with the effective exposure time of ~ 6 minutes. Those images are stacked and mosaicked after the astrometry correction has been applied.

For the data reduction, KASI established data reduction pipeline software written in *Python* code. The pipeline composed of six processes, bad pixels masking, non-linearity correction of the detector signals, frame differentiation, flat-field correction and astrometry correction (Han et al. 2014).

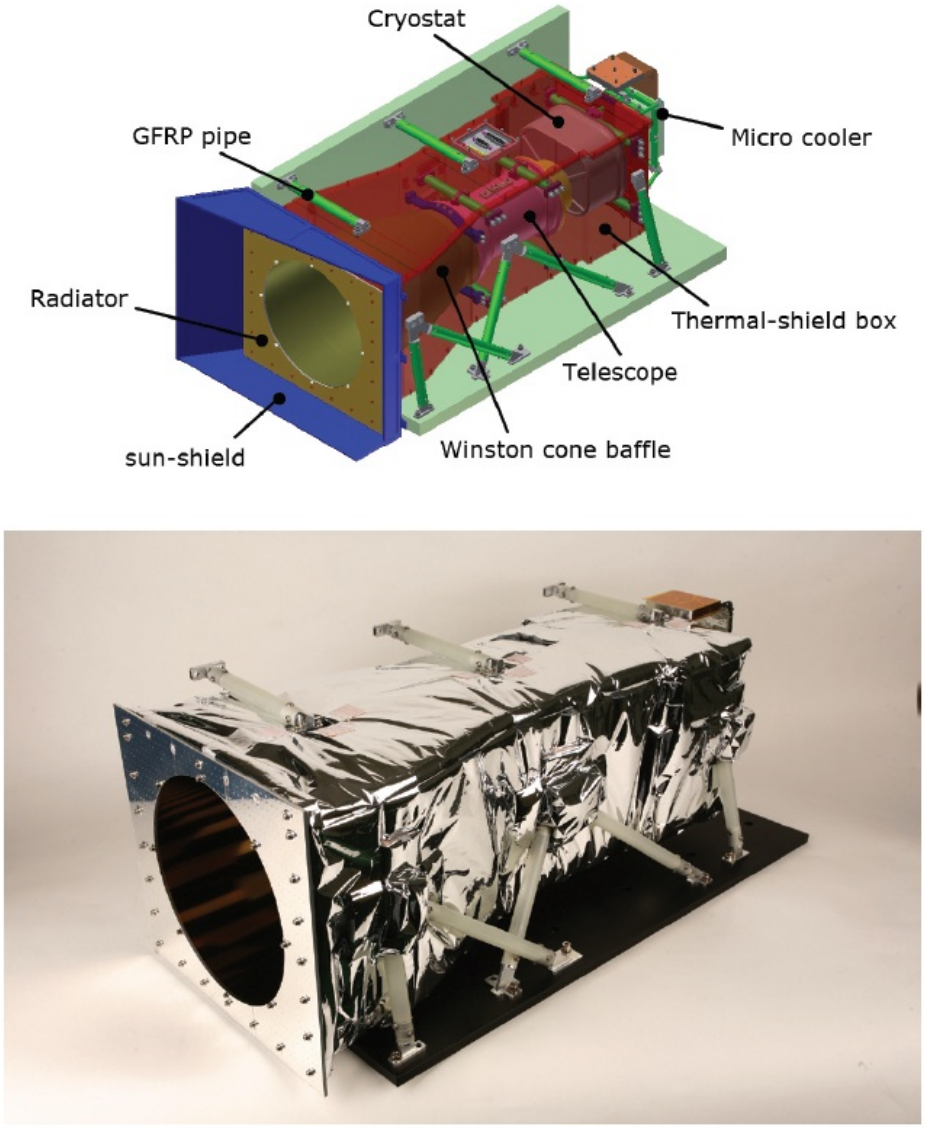

Figure 2.2 Mechanical layout and appearance of MIRIS telescope, which is composed of a radiator, a Winston cone baffle, a sunshade, a thermal-shield box, the Glass Fiber Reinforced Plastic pipe support, 30 layers of Multi-Layer Insulation (MLI), a cryostat, a filter-wheel, and a micro cooler.

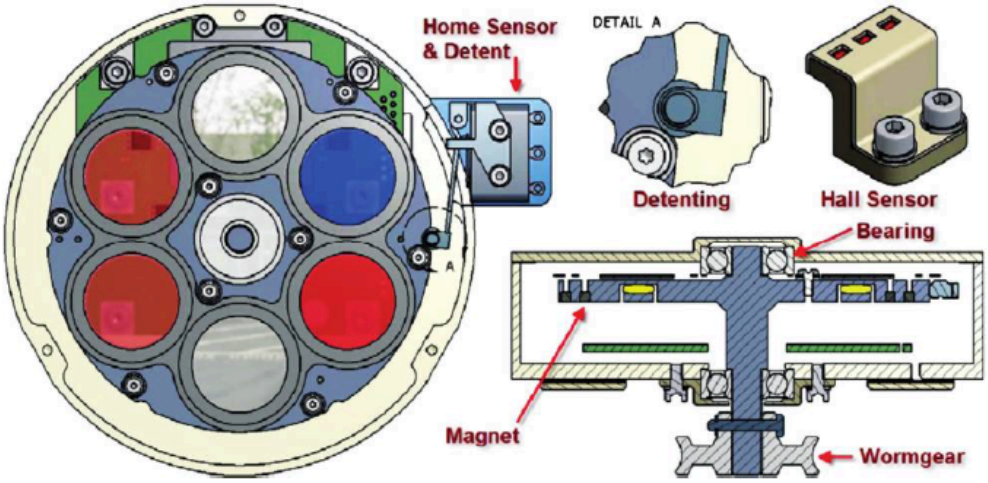

Figure 2.3 Filter-wheel and driving system overview of MIRIS, which is consist of I, H-bands (blue and red) and the Paschen-α line filter (gray), dual continuum filter (orange), plus an aluminum blank filter for dark measurements with a redundant filter

Chapter 3

Data processing

As described in previous section, data provision system of MIRIS is still in preparation. Thus, we individually conducted several processes of data reduction including flux calibration of MIRIS detector by using standard stars in observed images. And providing its informations to MIRIS team.

3.1 Instrument calibration

3.1.1 Evaluation of calibration factor

In order to derive surface brightness of the observed diffuse sky, we conducted instrument calibration. The standard method of flux calibration for the MIRIS detector had not yet been accomplished by the KASI team. Hence, we carried it out by ourselves using stars which exist in our target images.

First of all, we selected 50 stars from Two Micron All-sky Survey (2MASS) Point Source Catalog (PSC) (Cutri et al. 2003; Skrutskie et al. 2006) in our images whose spectral type is known. This is because we need spectral color correction due to very broad profiles of MIRIS bandpass filter. Then, we stacked these stars to estimate Point Spread Function (PSF) on the detector array. We approximate the beam profile as a two-dimensional Gaussian. Estimated Gaussian σ along both directions (σ_x and σ_y) are 1.14 $\pm$ 0.04 and 1.04 $\pm$ 0.10 pixel which are equivalent to 0.98 $\pm$ 0.03 and 0.09 arcmin. Stacked image and Gaussian fitting along both x and y direction with estimated σ is shown in Figure 3.1.

Next process is to determine the spectral radiance of the standard stars. We assume

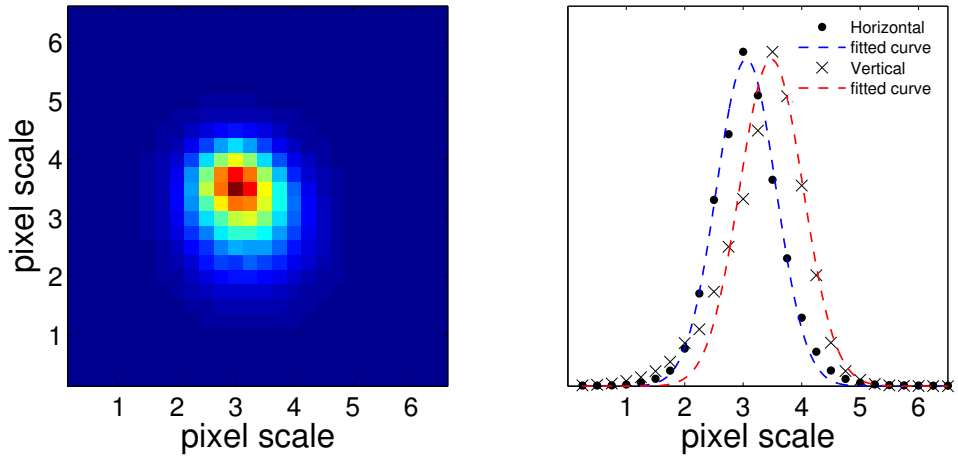

Figure 3.1 Left panel indicates a stacked image of I-band. Right panel indicates the crosscut profile of the beam along horizontal and vertical direction and dashed curves are fitted Gaussian with estimated σ from two-dimensional fitting.

that the spectra of the stars are blackbody whose temperature is derived from spectral type in catalogs, and they are scaled to 2MASS magnitude. For I-band, we adopted the 2MASS J-band flux as a scaling factor of the blackbody spectrum. For H-band case, 2MASS H-band flux is operated. We can express a star flux which is detected on the MIRIS focal plane F_i corresponds to star ID i with color correction by equation (3.1).

$$F_i = \frac{S_i \int_0^\infty B_i(\lambda)\, T(\lambda)\, d\lambda}{\int_0^\infty T(\lambda)\, d\lambda} \tag{3.1}$$

where T is transmittance of MIRIS filters (I and H-band) as a function of wavelength λ shown in Figure 3.2, S_i is scaling factor to 2MASS magnitude and planck function of star ID i, and B_i is blackbody spectrum of star ID i. Finally, we can obtain flux calibration factor C_i for star ID i by comparing a flux with the beam profile $P_i(x, y)$ integrated on whole array:

$$C_i = \frac{\lambda_C F_i}{\Omega_p \iint_{-\infty}^{\infty} P_i(x, y)\, dxdy} \tag{3.2}$$

where Ω_p is FOV of a pixel in unit of sr, λ_C is the center wavelength of both pass bands ($\lambda_C = 1.076\ \mu$m for I-band, $\lambda_C = 1.608\ \mu$m for H-band). We present evaluated flux calibration factor C_i in Figure 3.3, and direct comparison of pixel values and flux of standard stars is shown in Figure 3.6 For a few bright stars (~ 0.15 nW m^{-2} μm^{-1}

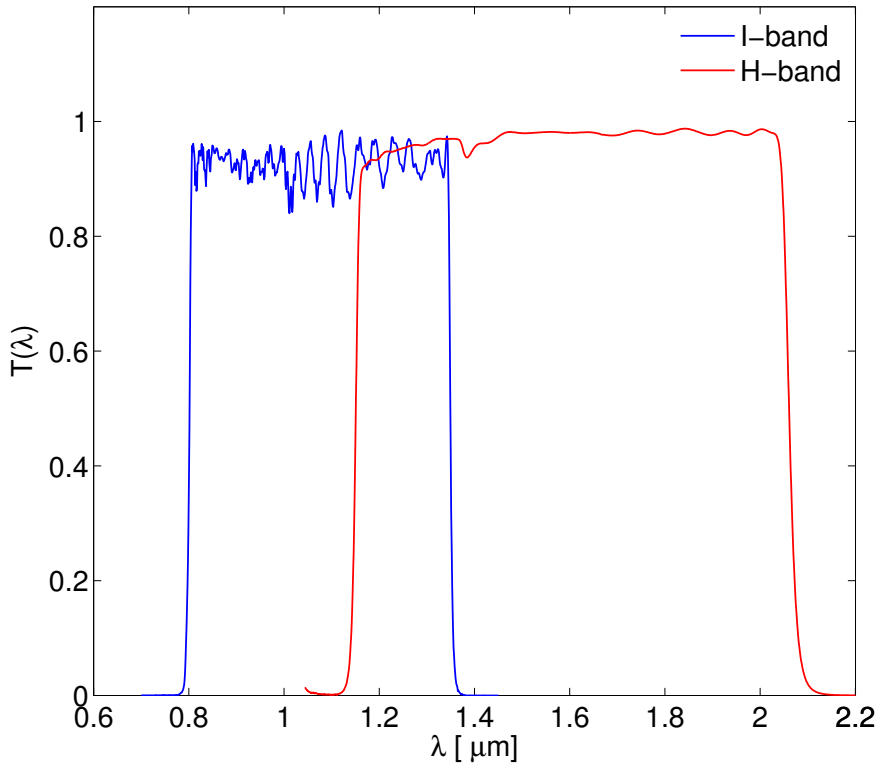

Figure 3.2 Transmittance plot of MIRIS I and H-band filters.

at I-band), because of their incompleteness of non-linearity correction, C_i becomes higher than most of the stars. We excluded these super bright stars when we estimate the mean of calibration factor. As a result, for I-band calibration factor, we derived 11.83 $\pm$ 0.34 nW m^{-2} sr^{-1} ADU^{-1}, for H-band, we also concluded 6.02 $\pm$ 0.11 nW m^{-2} sr^{-1} ADU^{-1}. These errors include both statistical error and photometric error of standard stars. The evaluation of systematic uncertainty is also described in next subsection. From our calibration, we estimated the detection limit of MIRIS telescope, which is

3.1.2 Evaluation of systematic error

It has been reported that the sensitivity of the MIRIS detector changes slightly over time during its observations. As it was difficult to correct this effect by directly modeling changes in detector sensitivity, we instead incorporated time variance of sensitivity as a systematic error of the calibration factor using data from three of

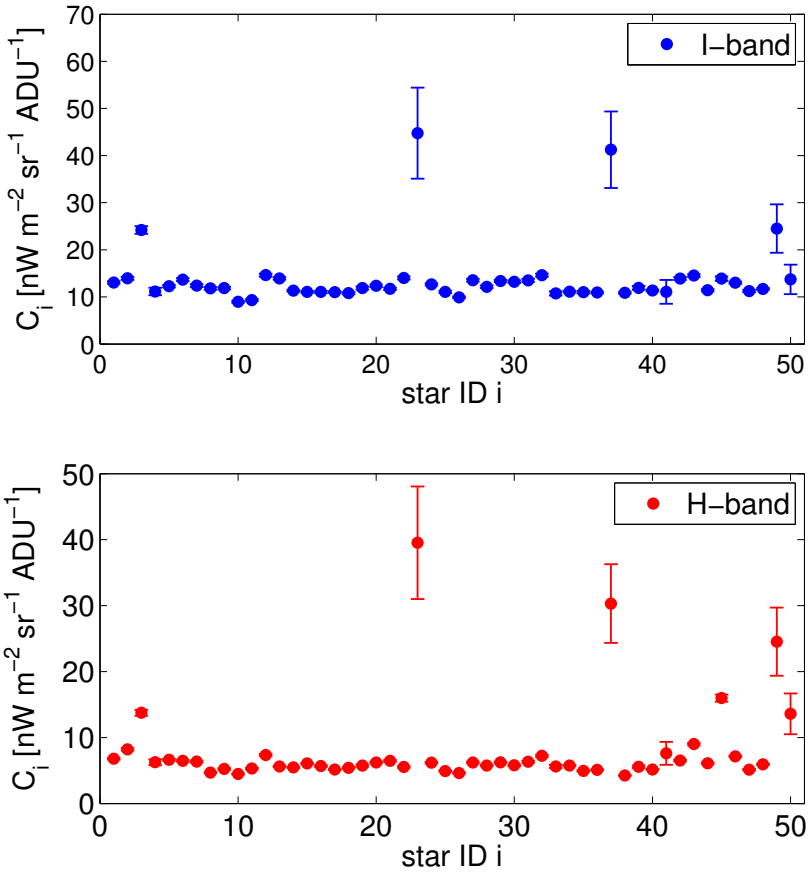

Figure 3.3 Estimated calibration factor which corresponds to star ID i. Top panel indicates I-band calibration and bottom panel indicates H-band's. Each error bar indicates photometric error provided by 2MASS catalog.

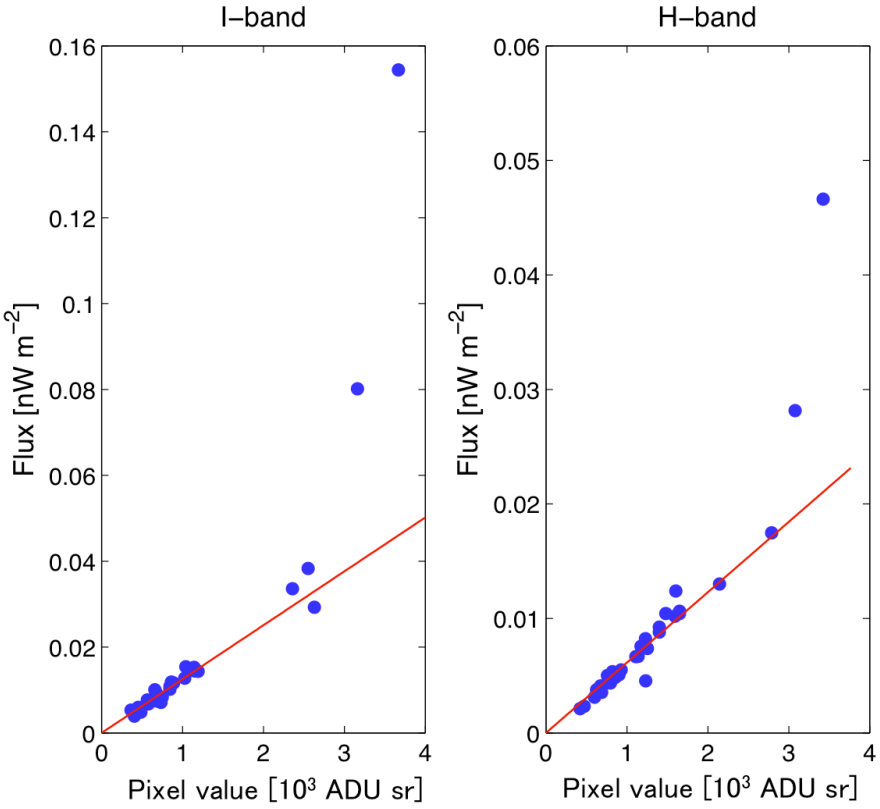

Figure 3.4 Comparison between pixel value and flux of standard stars in CIBDC3 after color correction has been applied.

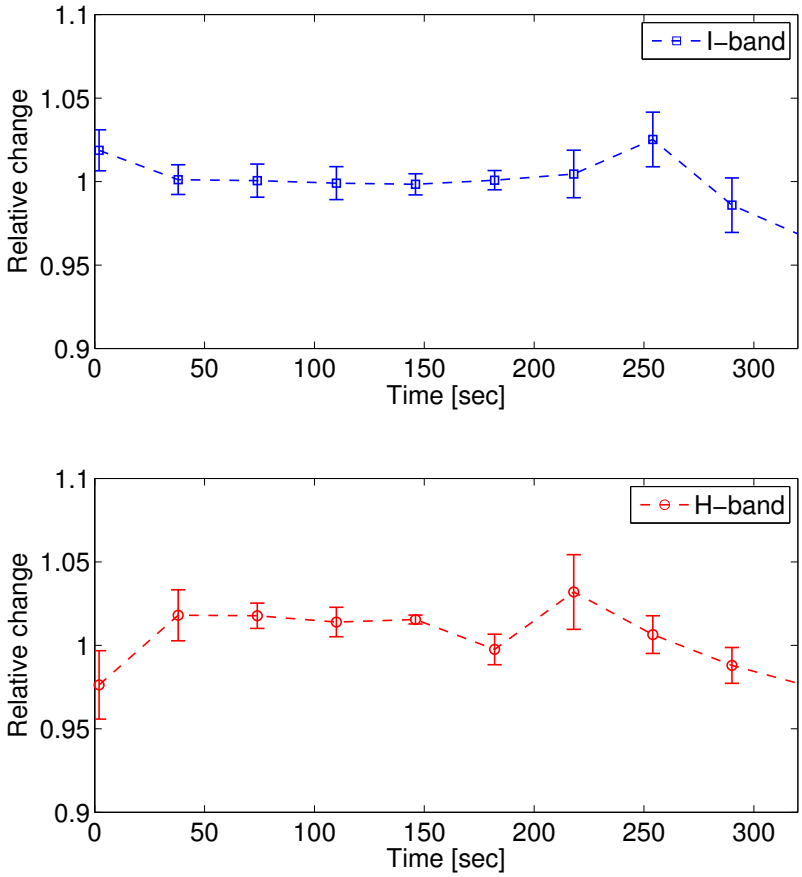

Figure 3.5 Relative change of calibration factor as a function of time. Top and bottom panels indicate I and H-band changes respectively. We utilized PSF template which is generalized by stacking of standard stars for the conversion of flux to intensity.

our targets that were utilized for instrument calibration. All of our fields had 4% time variance at maximum, and there was a 1.5% difference among all fields. The time variance of the calibration factor of CIBDC 3 is shown in Figure 4. We derived systematic uncertainties including the variance of three fields as root mean square (RMS) errors in the I- and H-bands of 1.9% and 2.4%, respectively. Finally, from the time and field variances, we estimated total calibration factor errors of 11.83 $\pm$ 0.34 nW m^{-2} sr^{-1} ADU^{-1} and 6.02 $\pm$ 0.27 nW m^{-2} sr^{-1} ADU^{-1} or the I and H-bands, respectively.

3.2 Point source masking

In order to analyze the diffuse emission in our field, it is necessary to remove bright point sources from the image. For the point source masking, two processes have been performed.

At first, we generated the integrated brightness map of the stars from the 2MASS Point Source Catalogue. The 2MASS PSC contains the photometry of the objects covering 99.998% of the sky with accurate detections below the completeness limit $J = 15.8$ and $H = 15.1$ magnitude (Skrutskie et al. 2006, Cutri et al. 2006). On the other hand, we estimated the confusion limit of the MIRIS toward the high Galactic latitude sky, which is approximately 15 magnitude at MIRIS H-band. Therefore, we utilized the H-band as the integrated brightness map for the masking. The sources are convolved with MIRIS Point Spread Function (PSF), then mask is generated for the pixels whose values are larger than sky noise.

Because of the pointing instability of the MIRIS which is approximately one pixel ($\sim 1'$) during the observations, there are slight incompleteness of the masking especially from bright sources. Thus, in the second process, we carried out the 2σ clipping method. In this process, we established the compartments in all parts of the array which are sufficiently larger than aperture scale but smaller than the size of the dark clouds ($\sim 10 \times 10$ pixels) and calculated the means to determine 2σ in each compartment, then pixels which have larger/smaller value than 2σ were masked. We iterated this clipping procedure until clipped pixels disappear.

3.3 Removal of the gradient of ZL

The one necessary thing is removal of the ZL in order to take the spatial correlation between our image and 100 μm. ZL is scattered component by interplanetary dust which is illuminated by Sun and it dominates the diffuse sky component more than 80 % of the total brightness. ZL is known to be uniform on spatial scales smaller than a degree (Abraham et al. 1997; Kashlinsky et al. 2005; Pyo et al. 2012). However, because of large FOV of MIRIS, we must remove the large-scale spatial gradient of the ZL for the evaluation of DGL from MIRIS data.

In order to remove the gradient of ZL, we adopted a ZL model generated by Kelsall et al. (1998) based on the observation of DIRBE/*COBE*. Modeling of the

ZL is accomplished at 1.25 and 2.2 μm. Therefore, we need a spectral information of ZL other than its absolute value. To obtain the spectral information of ZL for our observation bands, we used the data of CIBER/LRS (Tsumura et al. 2010; Arai et al. 2015) which observed the low resolution spectrum of several local regions in different ecliptic latitude. Then we extracted a spectrum of ZL from absolute changes between several different fields. Relative change of ZL within each image taken by MIRIS (in $3.67^\circ \times 3.67^\circ$) is $\pm 3\%$ which are shown in Figure 3.6. We also investigated the effect of absolute uncertainty of ZL model and described in Appendix C.

3.4 Smoothing of the images

The resolution of the *IRAS* image is approximately three times lower than the that of MIRIS ($\sim 0\farcm9$). Hence, in the process of smoothing, the measurement errors are reduced due to the averaging of independent data points. In order to compare the MIRIS data and the 100μm map derived by *IRAS*/DIRBE (Schlegel et al. 1998), we reduced the resolution of the near-infrared images to the same resolution as the *IRAS* 100 μm resolution ($2\farcm372 \times 2\farcm372$) by averaging 3×3 pixels of MIRIS. We present the processed images in comparison with 100 μm map in Figure 3.7.

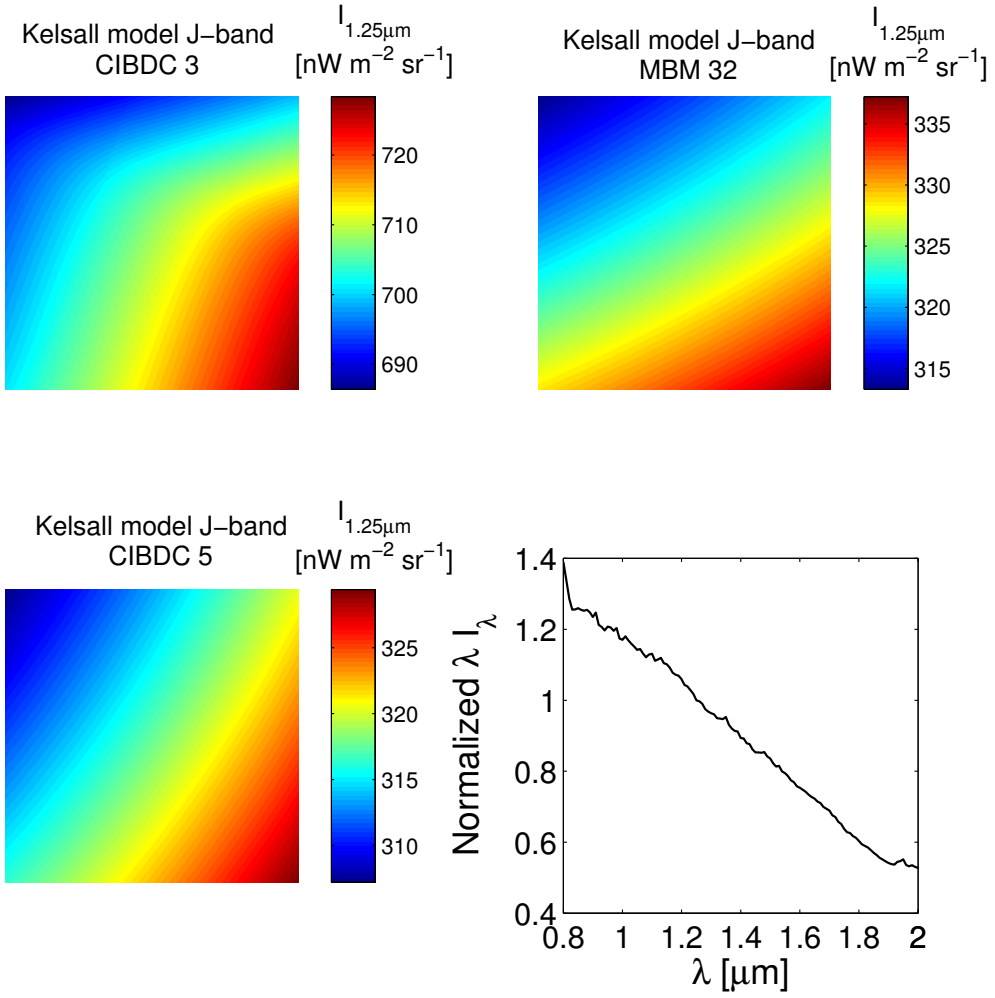

Figure 3.6 The ZL gradient at 1.25 μm for each field based on the model of Kelsall et al. (1998) and the spectrum of ZL derived by Arai et al. (2015). The top left panel is the ZL gradient in CIBDC 3 field, the top right panel is MBM 32's, the bottom left panel is CIBDC 5's, and the bottom right panel indicates the spectrum of ZL normalized by 1.25 μm.

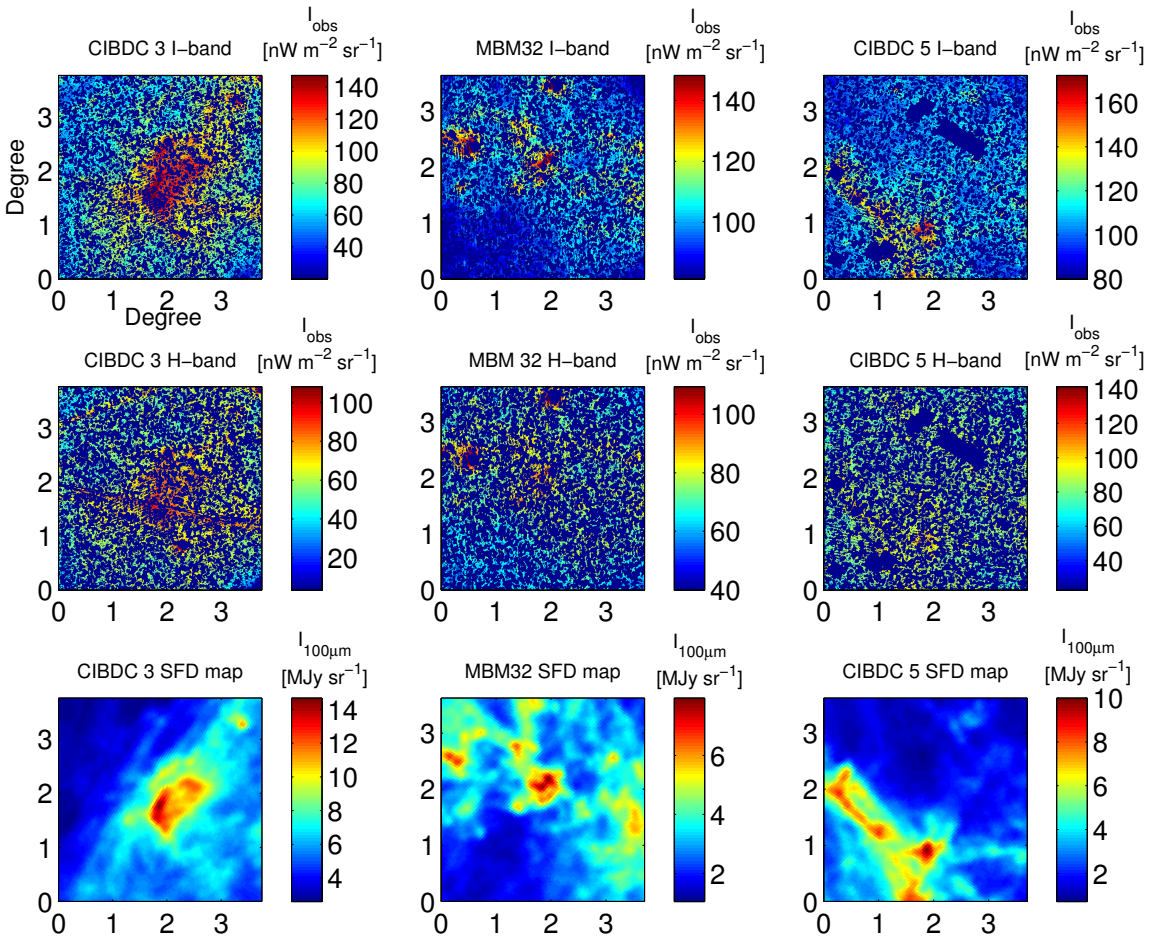

Figure 3.7 The images of our targets after the all reduction processes has been applied. Top panels and middle panels indicate I and H-band images respecttively, bottom panels are SFD 100 μm intensity map corresponds to FOV in each target. For the top and middle panels, colorbars indicate the brightness in the unit of nW m^{-2} sr^{-1}. For the bottom pannels, in the unit of MJy sr^{-1}.

Chapter 4

Analysis of DGL

4.1 Correlation analysis between near-infrared and 100 μm

Previous study of the DGL reveals that scattering components through the interstellar dust has correlation with the far-infrared dust emission which is corresponds to column density of the interstellar dust grains. We correlated the near-infrared data with SFD 100 μm map. First of all, we need to clear and enumerate the relation between DGL and far-infrared emission. According to Henyey (1937), DGL brightness along a line of sight I_{DGL} can be written as:

$$I_{DGL} = \frac{\gamma_\lambda}{1-\gamma_\lambda} I_{ISRF} \left[1 - e^{-(1-\gamma_\lambda)\sigma_\lambda N_D}\right] \tag{4.1}$$

where γ_λ and σ_λ represent albedo and scattering cross section of the interstellar dust depending on wavelength λ, I_{ISRF} indicates the brightness of interstellar radiation field (ISRF) and N_D is column density of interstellar dust. We can replace equation (4.1) to (4.2) for the optically thin limit $\sigma_\lambda N_D \ll 1$.

$$I_{DGL} \approx \gamma_\lambda I_{ISRF} \sigma_\lambda N_D \tag{4.2}$$

On the other hand, the brightness of far-infrared 100 μm emission $I_{100\mu\mathrm{m}}$ is expressed as:

$$I_{100\mu\mathrm{m}} \approx (1 - \gamma_{100\mu\mathrm{m}})\, \sigma_{100\mu\mathrm{m}} N_D B\,(T_D) \tag{4.3}$$

where B presents a Planck function of the dust temperature T_D. At last, we can write

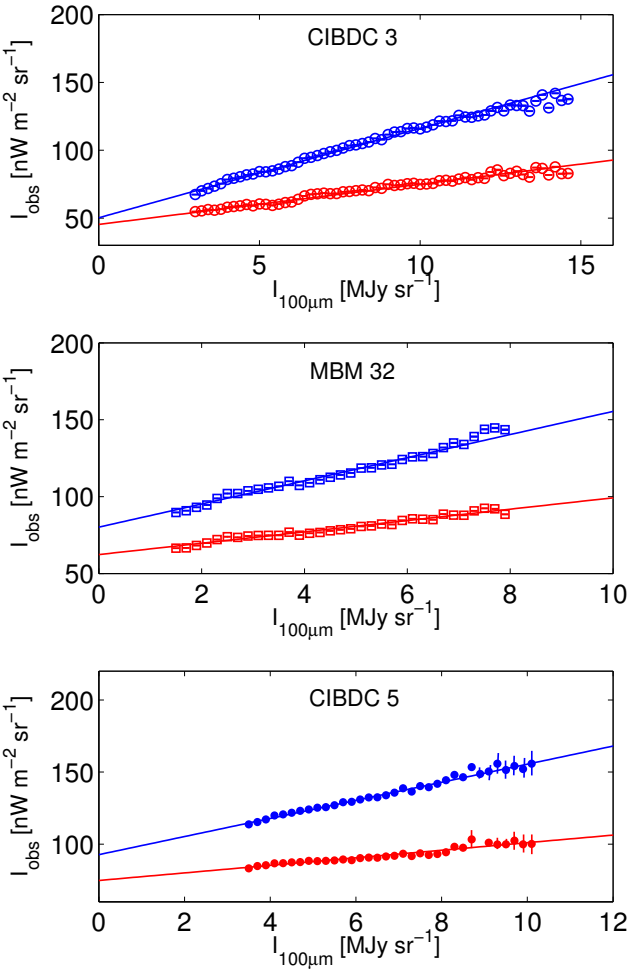

Figure 4.1 Comparison between near-infrared brightness and 100 μm brightness (blue:I-band, red: H-band). Each point are binned with the resolution of 0.2 MJy sr^{-1}. Errors of each point are also reduced by the binning. The panels from top to bottom indicate the comparison for CIBDC 3, MBM 32, and CIBDC 5 field. The solid lines in each panel present the best fit lines of the correlation from minimum to maximum range of 100 μm brightness.

the relation between I_{DGL} and $I_{100\mu\mathrm{m}}$ as

$$I_{DGL} \approx \frac{\gamma_\lambda I_{ISRF} \sigma_\lambda}{(1-\gamma_{100\mu\mathrm{m}})\,\sigma_{100\mu\mathrm{m}} B\,(T_D)} I_{100\mu\mathrm{m}} \tag{4.4}$$

From equation (4.4), there is linear correlation between the brightness of DGL and the 100 μm emission for optically thin case.

Besides DGL, observational data is contributed by isotropic components EBL and integrated faint star. Therefore, we can approximate the near-infrared measured sky brightness I_{obs} as

$$I_{obs} = a_\lambda + b_\lambda I_{100\mu\mathrm{m}} \tag{4.5}$$

Slope b_λ indicates relative brightness of DGL against the brightness of 100 μm in unit of nW m^{-2} MJy^{-1}, and a_λ gives contributions of spatially isotropic components (ISL, ZL and EBL) in unit of nW m^{-2} sr^{-1}. There is significant difference between CIBDC 3 and the other fields. The variance of isotropic a_λ is thought to be affected by uncertainty of the model of the ZL which is utilized in section 3.3. As shown in Table 2.1, CIBDC 3 locates on low ecliptic latitude where ZL is roughly twice stronger than MBM 32 and CIBDC 5.

We put the results of the linear fitting by equation (4.5) in Figure 4.1. Each data point includes pixel variances and dashed line presents the best fit line when we consider the uncertainty of calibration factor. All fields clearly correlate with 100 μm. As can be seen in Figure 4.1 our DGL result b_λ by correlative analysis is hardly influenced by the absolute error of the calibration. The coefficient values and its errors are summarized in Table 4.1. Our DGL results b_λ comparing with previous results are plotted in 4.4 in comparison with previous results.

If the dust scattering is not optically thin, DGL will not correlate linearly with 100 μm. We investigated how coefficient values have been changed when we use various local ranges of the 100 μm brightness. As a result, the slope where $I_{100\mu\mathrm{m}}$ is faint ($\leq$7 MJy sr^{-1}) has approximately 20% differences for a slope derived from brighter $I_{100\mu\mathrm{m}}$ range. The result shows that a slope of the correlation significantly changes with a range of $I_{100\mu\mathrm{m}}$ neighboring 10 MJy sr^{-1}. We finalized the result by taking weighted mean of each $I_{100\mu\mathrm{m}}$ range belong to each field. The result summarized in Table 4.1.

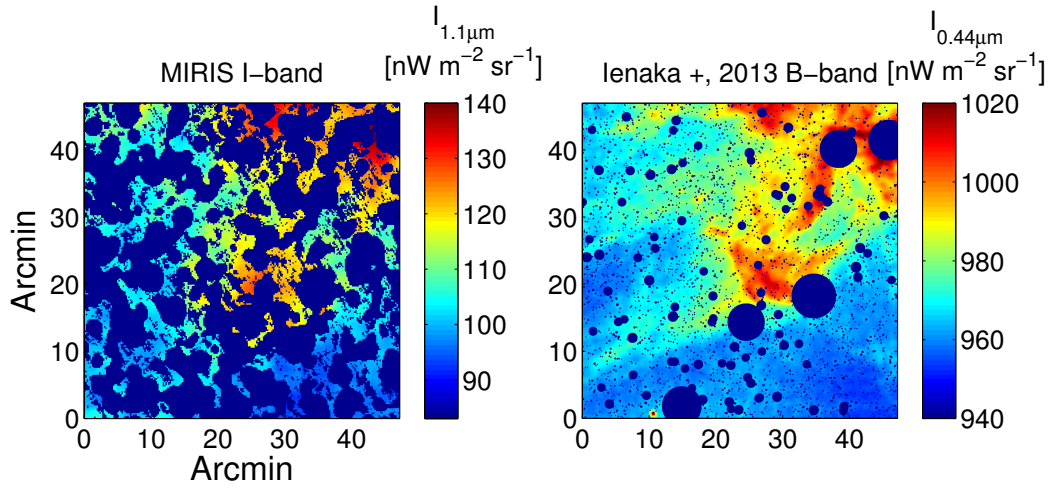

Figure 4.2 Images of MBM 32. Left panel is the sub-frame image of MIRIS corresponding to optical images shown in right panel, which is the B-band image observed by Ienaka et al. (2013). On the image of Ienaka et al. (2013), the masking of bright sources was applied in their data processing. Colorbars indicate brightness in units of nW m^{-2} sr^{-1}.

4.2 Correlation between near-infrared and optical

To investigate the color of DGL between near-infrared and optical, we analyzed sub-frame image of MBM 32 where optical observation of DGL (B, g, V and R-band) was accomplished by Ienaka et al. (2013). The optical data were acquired by using the 105 cm Schmidt telescope with the 2KCCD camera with 2048×2048 pixels at Kiso observatory in dark nights in 2011 February, April, and 2012 February. The FOV of the camera is $50' \times 50'$ with a plate scale $1\farcs5$ $pixel^{-1}$. To calculate the correlation, we create a sub-frame image of MIRIS, and the resolution of optical image to match with the MIRIS's resolution. The sub-frame image and optical image is shown in Figure 4.2. We also determined the correlation coefficients between the I-band and optical bands (B, g, V and R-band) by linear fitting such as Figure 4.3. By using the correlation coefficients between I and B, g, V, R-band, we derived optical DGL which is also plotted in Figure 4.4.

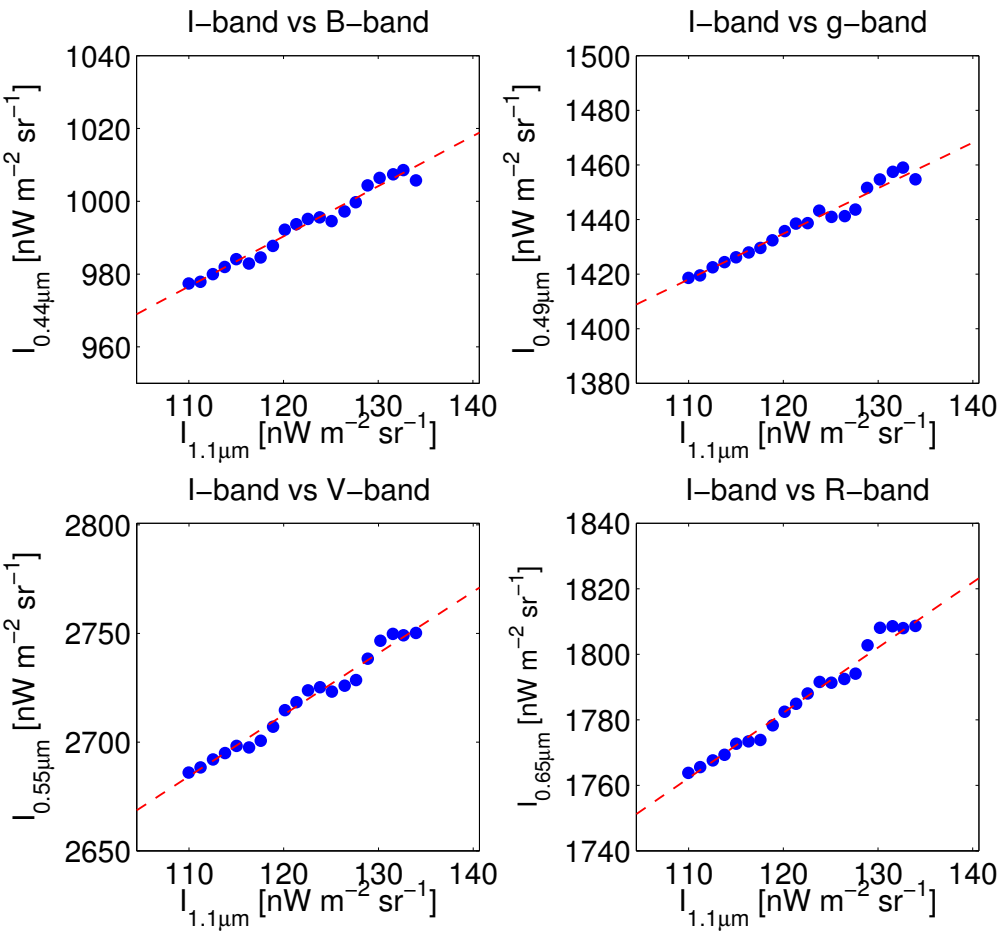

Figure 4.3 Comparison between 1.1 μm and four optical bands. Top left: comparison between 1.1μm and 0.44 μm, top right: 1.1 μm vs 0.49 μm, bottom left : 1.1 μm vs 0.55 μm, bottom right: 1.1 μm vs 0.65 μm

.

Table 4.1 Summary of the linear-fitting parameters for various ranges of $I_{100\mu m}$. The last column shows errors in the weighted mean, estimated from 1σ field variances.

Field name	Range of $I_{100\mu m}$ MJy sr^{-1}	$a_{1.1\mu m}$ nW m^{-2} sr^{-1}	$b_{1.1\mu m}$ nW m^{-2} MJy^{-1}	$a_{1.6\mu m}$ nW m^{-2} sr^{-1}	$b_{1.6\mu m}$ nW m^{-2} MJy^{-1}	$b_{1.1\mu m}/b_{1.6\mu m}$
CIBDC 3	$\leq$7	51.6 $\pm$ 3.1	6.89 $\pm$ 0.21	44.5 $\pm$ 2.0	3.00 $\pm$ 0.29	2.29 $\pm$ 0.23
	7 – 12	54.3 $\pm$ 3.4	6.11 $\pm$ 0.12	51.1 $\pm$ 2.3	2.55 $\pm$ 0.10	2.39 $\pm$ 0.10
	12 – 15	62.1 $\pm$ 3.9	5.20 $\pm$ 1.16	56.3 $\pm$ 2.7	2.03 $\pm$ 0.91	2.55 $\pm$ 1.27
	$\leq$ 15	50.3 $\pm$ 3.1	6.23 $\pm$ 0.10	42.4 $\pm$ 2.8	2.51 $\pm$ 0.09	2.48 $\pm$ 0.09
MBM 32	$\leq$5	85.9 $\pm$ 5.3	7.83 $\pm$ 0.50	60.2 $\pm$ 2.8	3.73 $\pm$ 0.33	2.10 $\pm$ 0.22
	5 – 7	87.1 $\pm$ 5.2	7.59 $\pm$ 0.60	59.7 $\pm$ 2.7	3.45 $\pm$ 0.35	2.20 $\pm$ 0.25
	$\leq$7	84.5 $\pm$ 5.2	7.75 $\pm$ 0.32	60.5 $\pm$ 2.7	3.64 $\pm$ 0.27	2.13 $\pm$ 0.19
CIBDC 5	$\leq$5	95.4 $\pm$ 5.6	6.68 $\pm$ 0.36	73.2 $\pm$ 4.8	2.85 $\pm$ 0.32	2.34 $\pm$ 0.29
	5 – 10	93.0 $\pm$ 5.6	6.36 $\pm$ 0.19	72.6 $\pm$ 3.3	2.54 $\pm$ 0.20	2.50 $\pm$ 0.21
	$\leq$10	94.7 $\pm$ 5.3	6.56 $\pm$ 0.12	72.1 $\pm$ 3.2	2.63 $\pm$ 0.10	2.49 $\pm$ 0.11
Weighted mean	——	——	**6.42 $\pm$ 0.82**	——	**2.65 $\pm$ 0.66**	——

Table 4.2 Optical–1.1μm color of DGL in MBM 32 and predicted colors by the models of Brandt & Draine (2012)

	$b_{0.44\mu m}/b_{1.1\mu m}$	$b_{0.49\mu m}/b_{1.1\mu m}$	$b_{0.55\mu m}/b_{1.1\mu m}$	$b_{0.65\mu m}/b_{1.1\mu m}$
MBM 32	**1.38 ± 0.09**	**1.67 ± 0.09**	**2.83 ± 0.19**	**1.99 ± 0.10**
WD01/BC03	0.96	1.11	1.17	1.29
WD01/MMP83	0.89	1.00	1.12	1.26
ZDA04/BC03	1.33	1.53	1.61	1.71
ZDA04/MMP83	1.29	1.45	1.60	1.72

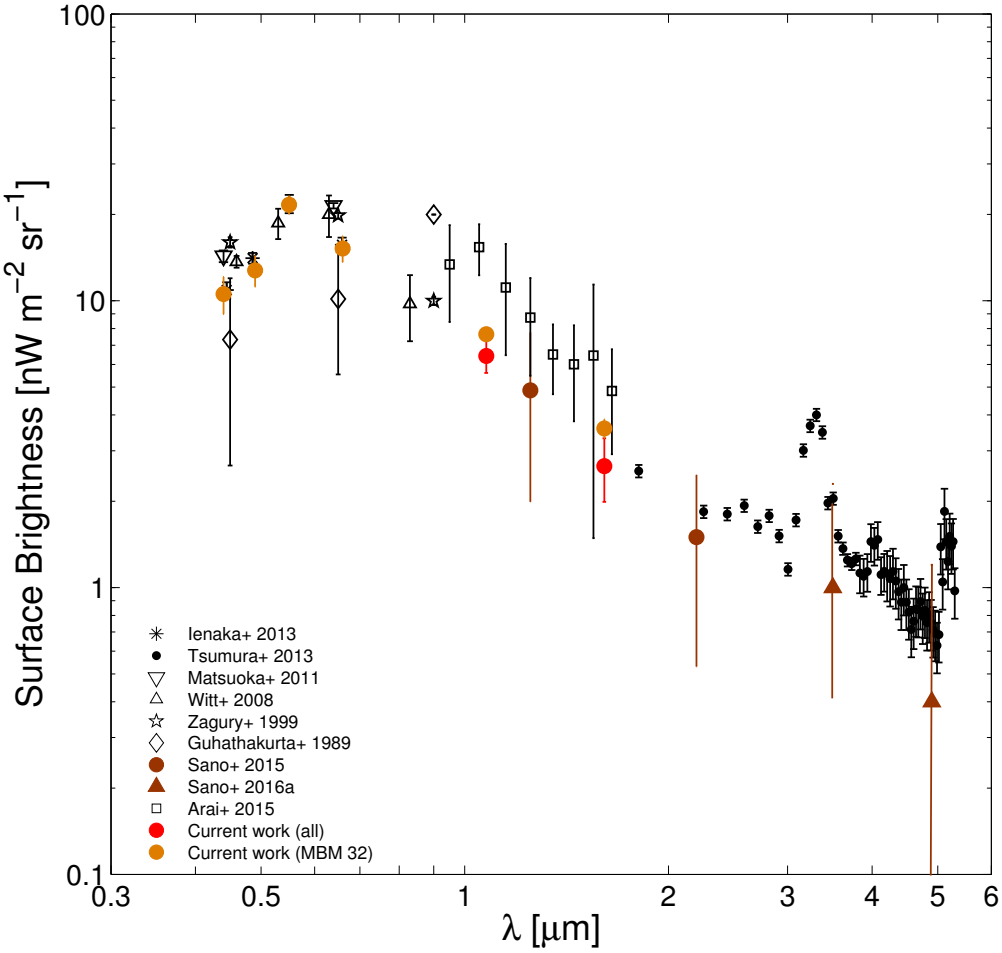

Figure 4.4 Surface brightness of the DGL normalized by $I_{100\mu\mathrm{m}} = 1$ MJy sr^{-1} as a function of wavelength λ. The red points show result from all data combined. The errorbars include 1σ standard errors and the variances of three fields. The orange points indicate the case of MBM 32 derived by correlation between MIRIS and Ienaka et al. (2013).

Chapter 5

Discussion on DGL

Here, we discuss on size distribution of interstellar dust grains by examining applicability of a popular dust model (Weingartner & Draine 2001), in order to explain the obtained spectrum of DGL. For further discussion of size distribution, we also investigated the effect on the interstellar extinction and thermal emission from dust grains in comparison with extinction curve and *Planck* observation.

5.1 Spectrum of DGL

Wavelength dependence of DGL is a reliable tool for investigating the size distribution of interstellar dust grains. As shown in Figure 4.4, our DGL result smoothly connects to the DIRBE/*COBE* data points derived by Sano et al. (2015) and is marginally consistent with the spectrum of CIBER/LRS produced by Arai et al. (2015).

For detailed investigation of scattered light, we compared our result with model spectra which is calculated from WD01 dust model using equation (1.4). For ISRF spectrum, we adopted a stellar population synthesis model from BC03, with solar metallicity and an exponential star formation history over 12 Gyr. The comparison of our result with model spectrum is shown in Figure 5.1. Calculated spectra exhibits bluer color than the measured DGL from optical to near-infrared wavelength range.

One cause of inconsistency between model spectra and the measured DGL is that BC03 model is bluer than real ISRF spectrum. Maraston (2005) (M05), Charlot & Bruzual (2007) (CB07) suggested that intermediate mass stars in the thermally pulsing asymptotic giant branch (TP-AGB) phase of their evolution contribute at

least 50% of the near-infrared light. However, Melbourne et al. (2012), and Zibetti et al. (2013) have shown evidence that the treatment of the TP-AGB stars in the CB07 and M05 models overestimates the contribution by TP-AGB stars in the NIR, favoring BC03. Moreover, derived DGL color (0.5 μm to 1.6 μm 2.5 times differs in comparison with model spectrum. Thus, it is difficult to explain the discrepancy of color by only ISRF spectrum, because the color difference (0.55 μm to 1.6 μm) between BC03 and M05, CB07 is less than difference of DGL color.

Another possibility of inconsistency is that albedo in dust models is not a real one. Actually, conventional dust models are generated to reproduce the optical interstellar extinction (Fitzpatrick 1999) without the consideration of other properties of dust grains such as albedos. Ienaka et al. (2013) noted that the changing of albedo from 0.6 to 0.8 causes more than twice increase of DGL. This discrepancy suggests that the real albedo is greater than what was used in the models. In fact, high near-infrared albedo has been reported for several regions: 0.86 at 2.1 μm for the prominent dust lane in the Evil eye galaxy NGC4826 (Witt et al. 1994) and 0.9 at 2.1 μm for the dust in the M51 arms (Block 1996) and 0.6–0.8 in Thumb Print Neblae (Lehtinen & Mattila 1996). Li (2004) interprets the discrepancy of the albedos between observation and models by suggesting the existence of a population of interstellar dust grains of at least 0.5 μm, which could be responsible for the near-infrared scattering and/or the measured high albedo may be caused by thermal continuum emission from stochastically heated ultra-small grains.

On the other hand, Sano et al. (2016b) derived Galactic-latitude dependence of the intensity ratios of near-infrared DGL (1.25 and 2.2 μm) to 100 μm emission from the DIRBE/*COBE* data at high Galactic latitudes ($|b| > 35^\circ$) and they found that the ratios ($I_{DGL}/I_{100\mu m}$) increase toward low-latitude regions. In contrast, according to the model by Draine & Li (2007), a contribution of near-infrared thermal emission from small dust grains is expected to decrease toward low-latitudes. The decreasing trend of the model is characterized by the peak shift of the far-infrared thermal emission at 100 μm by increasing of the ISRF toward low-latitude regions, i.e. dust temperatures. The result of Sano et al. (2016b) suggests that the near-infrared thermal emission does not contribute to latitude dependence of DGL. Thus, the high near-infrared albedo is expected to be produced by scattering process through the interstellar dust grains.

The character of the electromagnetic scattering depends on the dimensionless ratio

a/λ where a is grain radius and λ is wavelength of scattered light. In the case of $a/\lambda \ll 1$, scattering factor is proportional to λ^{-4} and it is called Rayley-scattering. For $a/\lambda \approx 1$, scattering factor is independent on wavelength and this is called Mie-scattering. Thus, to explain the red spectrum of albedo from optical to near-infrared, it is expected to be larger amount of micrometer sized grains in local molecular cloud than model predictions. In addition, as plotted in Figure 1.4, recent measurement of extinction in Galactic center (Lutz 1999; Nishiyama et al. 2009), the Galactic plane (Indebetouw et al. 2005; Jiang et al. 2006; Gao et al. 2009), the Coalsack nebula (Wang et al. 2013), and nearby star-forming regions (Flaherty et al. 2007) appear to suggest that mid-infrared (3–8 μm) extinction curve has a universally flat extinction law, even though ordinary dust models (e.g., WD01) predicts a power-law extinction of $A_\lambda \propto \lambda^{-1.75}$ at $\lambda \sim$ 1–7 μm. This is a further evidence for existence of larger grains.

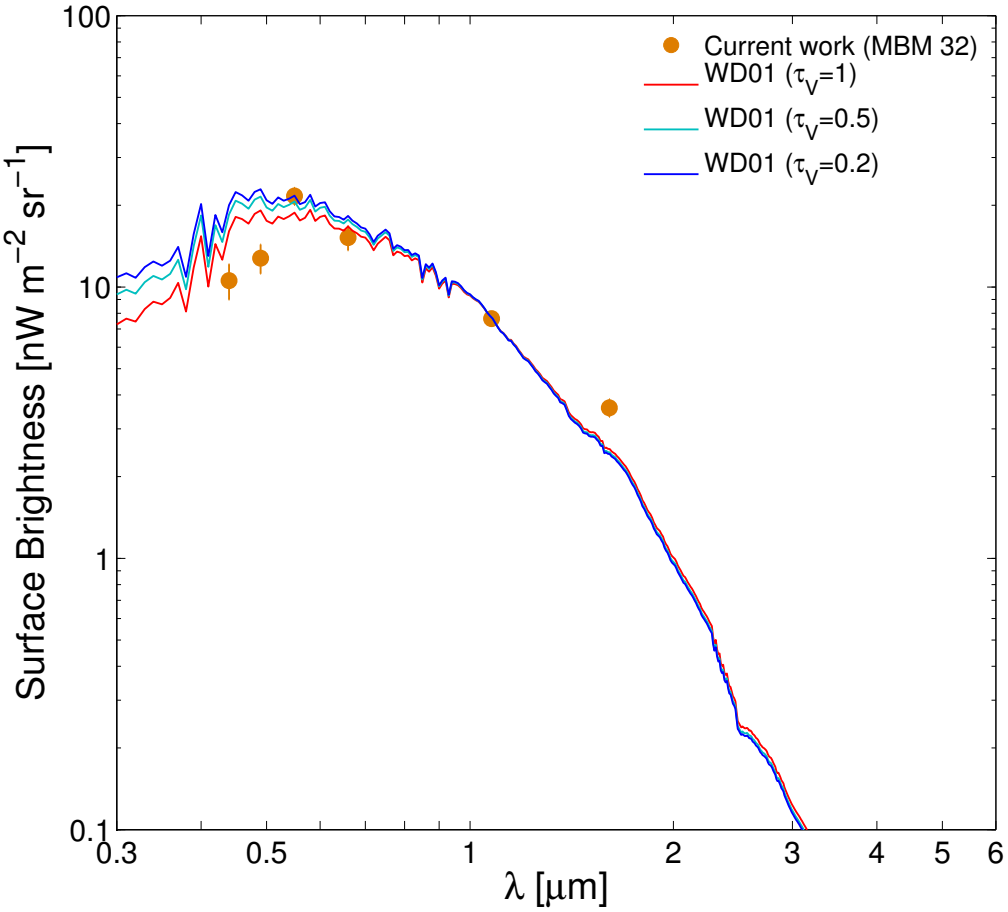

Figure 5.1 Surface brightness of the DGL normalized by $I_{100\mu\mathrm{m}} = 1$ MJy sr^{-1} as a function of wavelength λ. Solid curves represent the model spectra for several optical depth corresponding to MBM 32's, which is calculated with equation (1.4) by applying WD01 interstellar dust model.

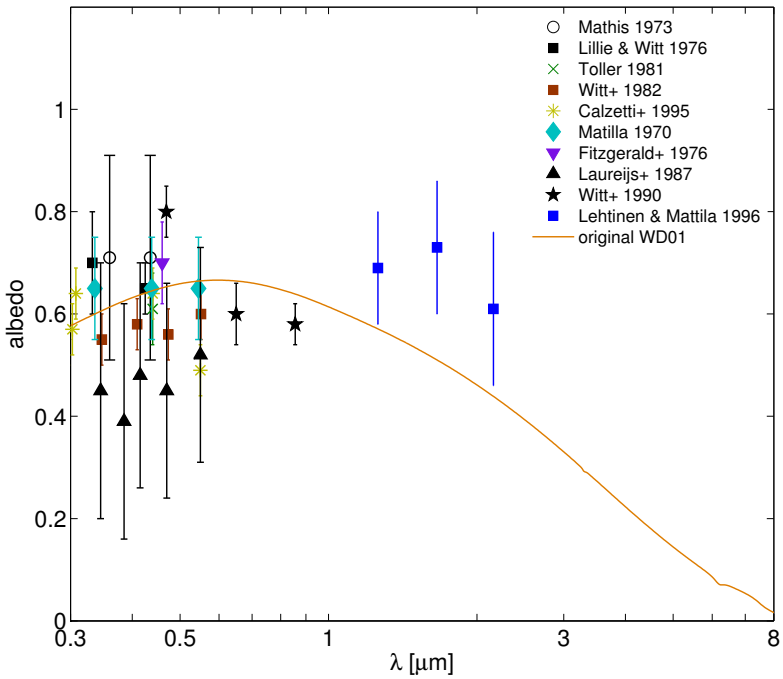

Figure 5.2 Current values and previous values of albedos. The orange solid curves present an albedo spectrum which is calculated by original WD01 model for R_V=3.1.

5.2 Extension of the dust model

In order to explain high near-infrared albedos, we created the model including micrometer sized grains in addition to sub-micrometer sized grains. By using created models, we calculated the grain albedos and DGL spectrum. The calculation has been done with the code of Mie-scattering which is generated by Bruce T. Draine.

5.2.1 Functional form of size distribution

At first, we have to give a size distributions of silicate and graphite grains. In general, the size of the interstellar dust is thought to follow the power-law distribution $dn/da \propto a^{-\alpha}$. We employed size distribution model of WD01. Functional form of WD01 is given by

$$\frac{1}{n_H}\frac{dn}{da} = \frac{C}{a}\left(\frac{a}{a_t}\right)^{\alpha} F(a)\, f(a) \tag{5.1}$$

$$F(a) = \begin{cases} 1+\beta a/a_t & (\text{for} \quad \beta \geq 0) \\ (1-\beta a/a_t)^{-1} & (\text{for} \quad \beta < 0) \end{cases} \tag{5.2}$$

$$f(a) = \begin{cases} 1 & (\text{for} \quad a < a_t) \\ \exp\left\{-[(a-a_t)/a_c]^3\right\} & (\text{for} \quad a \geq a_t) \end{cases} \tag{5.3}$$

where n_H is the number density of hydrogen nuclei, n is the number of grains whose radius is a. Nominal number of the parameters in WD01 model, C, a_t, a_c, α, β for (graphite, silicate) are (9.99×10^{-12}, 1.00×10^{-13}), (0.0107, 0.164), (0.428, 0.1), (-1.54, -2.21), (-0.165, 0.300). Amount of large grains are controlled by exponential cutoff with parameter a_c in equation (5.4). In this calculation, we deal with the grains whose size 0.001, 0.0025, 0.0063, 0.01, 0.015, 0.025, 0.039, 0.063, 0.1, 0.15, 0.25, 0.39, 0.63, 1.0, 1.5, 2.5, 3.9, and 6.3 μm. In our model, we extent graphite grains toward larger size, because silicate grains are more transparent at $\lambda < 8$ μm, exhibit a Si–O resonance dip at ~ 8 μm which is not seen in the observed extinction curve, and poorer than carbon dust. We created two petters of model as:

- (1) Single power-law distribution where $f(a) = 1$, $\beta = 0$, the other parameters are given by nominal value in WD01.
- (2) Two distributions, one is for sub-micrometer sized grains with $a_c = 0.3$,

and nominal WD01 parameters, another is for micrometer grains with $a_c = 5$, $\alpha = -0.5$, $C = 2 \times 10^{-13}$, and nominal WD01 parameters.

The size distributions of them are shown in Figure 5.3.

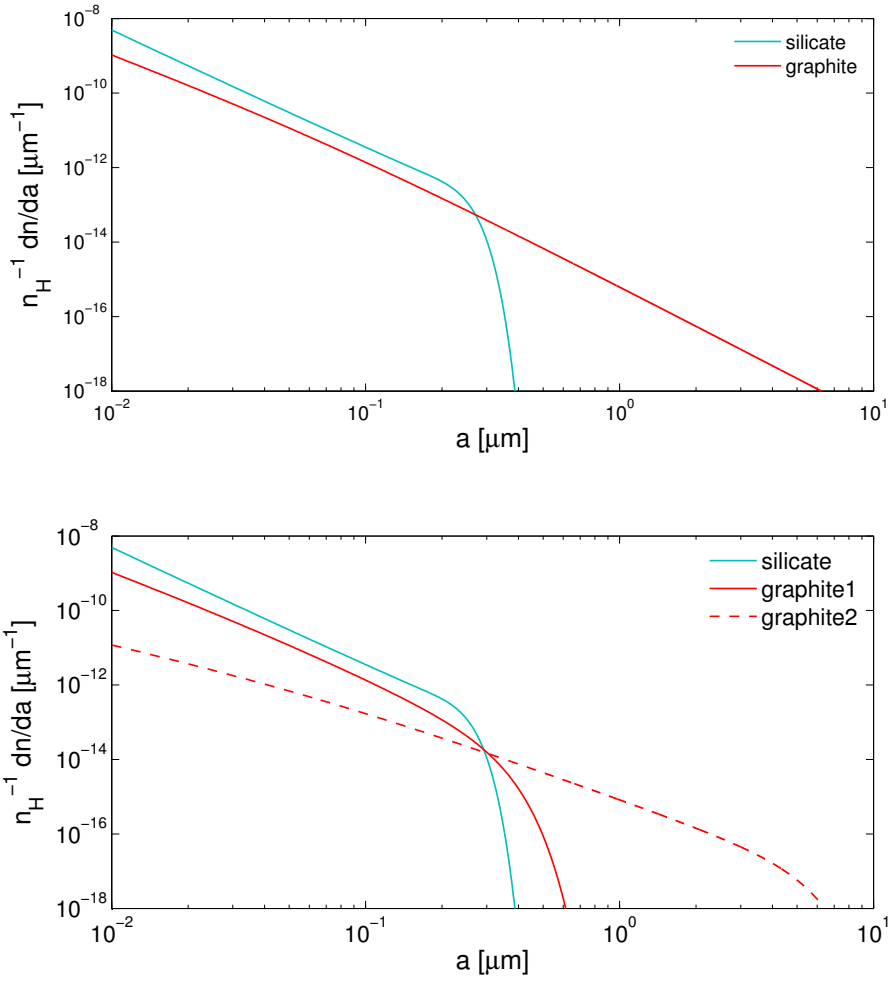

Figure 5.3 The created size distributions. The top panel indicates a created distribution from case (1) with the single power-law of graphite grains, the bottom panel indicates the case (2), with the two components of sub-micrometer and micrometer graphite grains distributions.

5.2.2 Fitting to the interstellar extinction

The micrometer sized grains are responsible for interstellar extinction and must distort a shape of extinction curve. Therefore, we need to create the model without contradiction to the conventional extinction curve in optical wavelength range. To calculate the extinction $A(\lambda)$ by dust grains, we utilized equation (5.5).

$$\frac{A(\lambda)}{N_H} = 1.086\pi \int a^2 Q_{ext}(\lambda, a) \frac{1}{n_H} \frac{dn}{da} da \tag{5.4}$$

where N_H is column density of hydrogens, $Q_{ext}(\lambda, a)$ is extinction efficiency (sum of absorption efficiency and scattering efficiency, $Q_{ext} = Q_{abs} + Q_{sca}$) of dust grains as a function of wavelength λ and grain size a which is generated by Draine's code. Calculated absorption efficiencies (Q_{abs}) and scattering efficiency (Q_{sca}) for 0.1, 1.0, 6.3 μm graphite grains are shown in Figure 5.4 and 5.5.

After the calculation of extinction, we fitted our model to optical extinction curve. For our (1) model, we conducted the fitting at optical wavelength range ($0.2 \leq \lambda_i \leq 0.7$ μm) by tuning the linear factor C of graphite distribution in equation (5.2). Fitting is carried out by minimizing equation (5.6).

$$\epsilon = \sum_i \left[1 - \frac{A(\lambda_i)}{A_0(\lambda_i)} \right]^2 \tag{5.5}$$

where $A(\lambda_i)$ is total extinction of grains which is generated by equation (5.4), $A_0(\lambda_i)$ is total extinction which is conducted with nominal parameters of WD01. Estimated linear factor for graphite distribution is 8.76×10^{-12}.

For our (2) model, distribution of sub-micrometer sized grains are fitted by same procedure as model (1) by minimizing equation (5.6), but the distribution of micrometer sized grains are fitted to measured mid-infrared extinction at $\lambda_i = 3.6, 4.5, 5.8, 8.0$ μm by minimizing equation (5.7).

$$\epsilon' = \sum_i \left[\overline{A_{MIR}(\lambda_i)} - A(\lambda_i) \right]^2 \tag{5.6}$$

where $\overline{A_{MIR}(\lambda_i)}$ is the mean value of measured extinction at wavelength λ_i. Estimated linear factor for sub-micrometer and micrometer graphite grains ($C_{\rm small}$ and $C_{\rm large}$) are 9.22×10^{-12} and 1.49×10^{-13}, respectively. Derived extinction curves with large grains are shown in Figure 5.6 as solid thick light green curves.

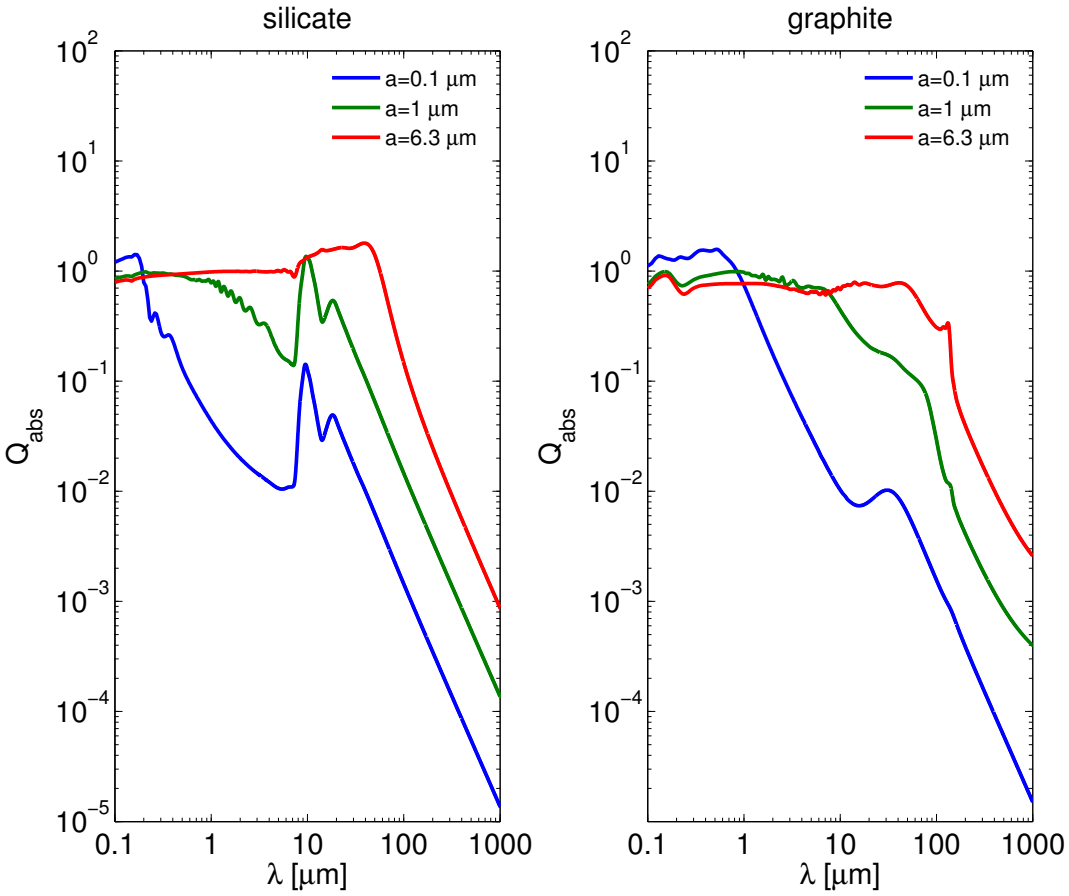

Figure 5.4 Calculated absorption efficiency Q_{abs} for silicate and graphite grains whose size 0.1, 1.0, 6.3 μm.

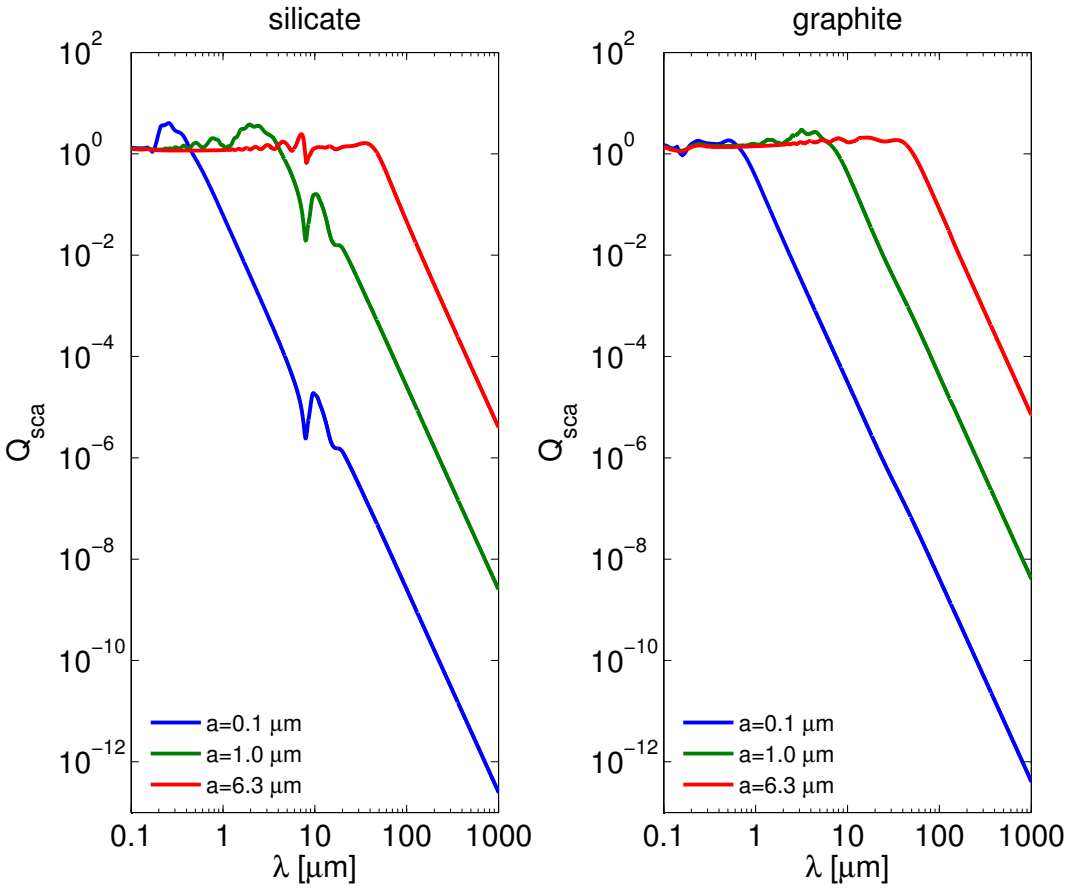

Figure 5.5 Calculated scattering efficiency Q_{sca} for silicate and graphite grains whose size 0.1, 1.0, 6.3 μm.

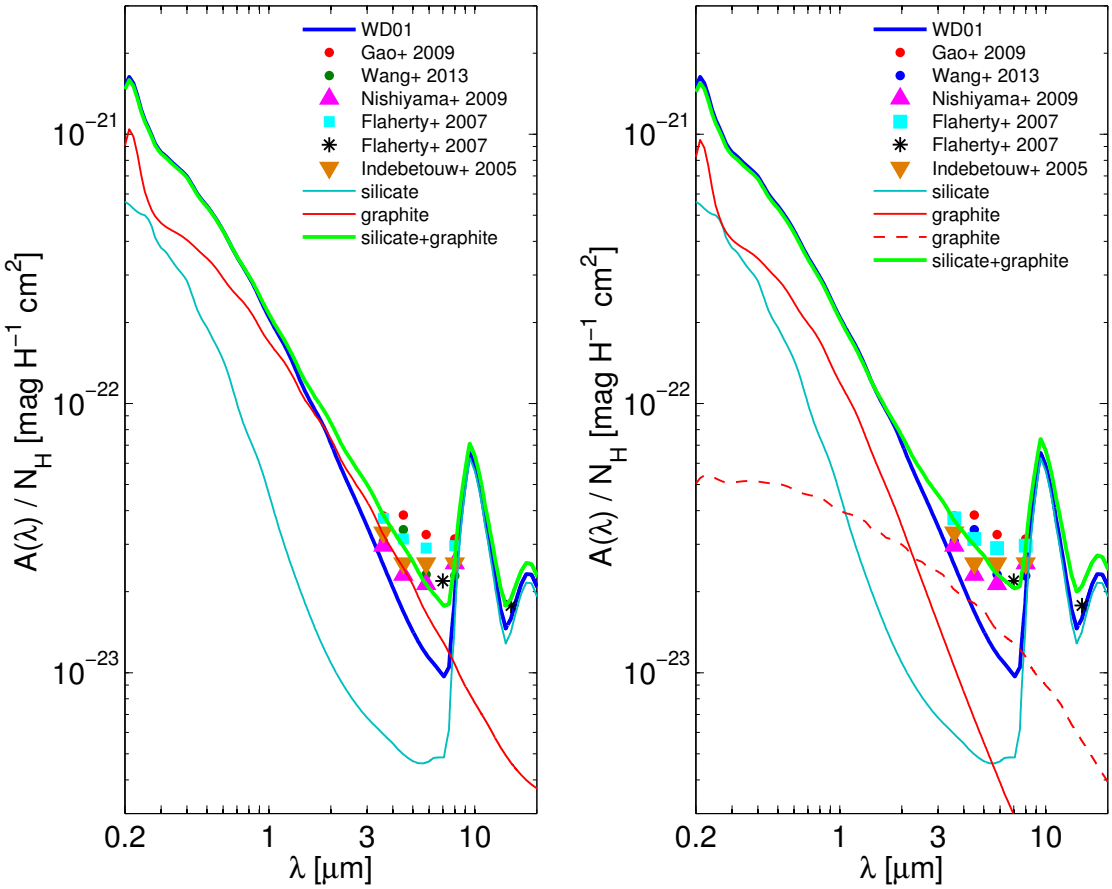

Figure 5.6 The extinction curves, which is fitted to a curve with the nominal parameters of WD01 in a range of $0.2 \leq \lambda_i \leq 0.7$ μm and measured mid-infrared extinction. The green thick curve in the left panel indicates a created extinction curve with a size distribution of case (1), the green curve in the right panel also indicates a created extinction curve but for case (2). The blue thick curves in both panels indicate a calculated extinction curve with the nominal parameter of WD01. The colored points show the measured extinctions same as Figure 1.4.

5.2.3 Thermal emission from large grains

Spectrum of far-infrared and milimeter-wave emission from dust grains was measured by DIRBE/*COBE* (Arendt et al. 1998), FIRAS/*COBE*, and recent Planck Collaboration XVII 2014. Observation of global SED from far-infrared to milimeter-wave is also important to constrains the abundance of the interstellar dust. Here, we investigated that our created models with micrometer sized grains do not conflict with the result of *Planck* observations.

At first, we calculated the equilibrium dust temperature in a given ISRF. The temperature of single dust grain is calculated by radiative energy balance as follows:

$$\pi a^2 \int_0^\infty Q_{abs}\left(\lambda, a\right) u_{ISRF}\left(\lambda\right) d\lambda = \frac{4\pi}{c} \pi a^2 \int_0^\infty Q_{emis}\left(\lambda, a\right) B\left(\lambda, T_D\right) d\lambda \tag{5.7}$$

where $u_{ISRF}\left(\lambda\right)$ is the energy density of ISRF as a function of wavelength λ, $B\left(\lambda, T_D\right)$ is the Planck function for dust temperature T_D, $Q_{abs}\left(\lambda, a\right)$ is the absorption efficiency of dust grains as a function of wavelength λ and grain radius a, $Q_{emis}\left(\lambda, a\right)$ is the emission efficiency of dust grains. The left side is an integral over the product of the incident flux per unit wavelength from the stars which can be calculated by assuming the energy density of ISRF. We employed the model of local ISRF by Mathis et al. (1983) at the galactocentric distance $D_G = 10$ kpc. The right-hand side is the surface area of the grain, multiplied by the thermal emission per unit area of a dust grain. To obtain the equilibrium temperature T_D, we calculated the right-hand side for the grain temperatures between 1 K and 50 K with 0.1 K internals, and selected the closest one with the left side value of equation (5.8). Estimated dust temperature T_D as a function of grain size is shown in Figure 5.7.

From dust temperatures, we also calculated infrared emission spectrum from dust grains using equation (5.9).

$$\frac{I_{FIR}\left(\lambda\right)}{N_H} = \pi \int a^2 Q_{abs}\left(\lambda, a\right) B\left(\lambda, T_D\right) \frac{1}{n_H} \frac{dn}{da} da \tag{5.8}$$

The result is shown in Figure 5.8 and Figure 5.9 in comparison with *Planck* observations corresponding to $N_H = 10^{20}$ cm^{-2}. We also plotted the emission spectrum from micrometer sized graphite grains ($a \geq 1$ μm) with green dashed curves. Our extended dust model shows agreement with *Planck* result for $N_H = 10^{20}$ cm^{-2}, and the contribution of infrared emission from micrometer sized grains is sufficiently lower than the total contribution from dust grains.

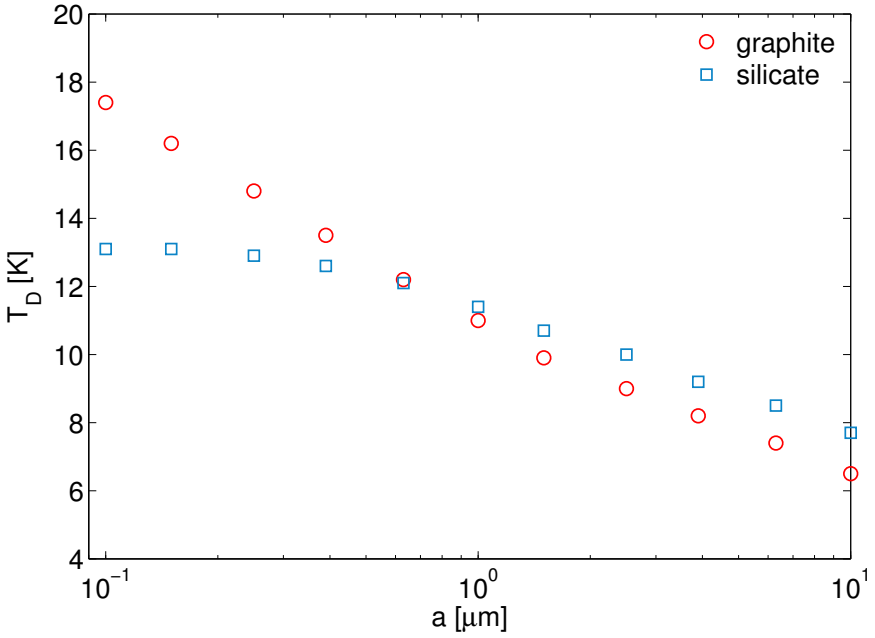

Figure 5.7 Equilibrium temperatures for silicate and graphite grains heated by the MMP83 ISRF.

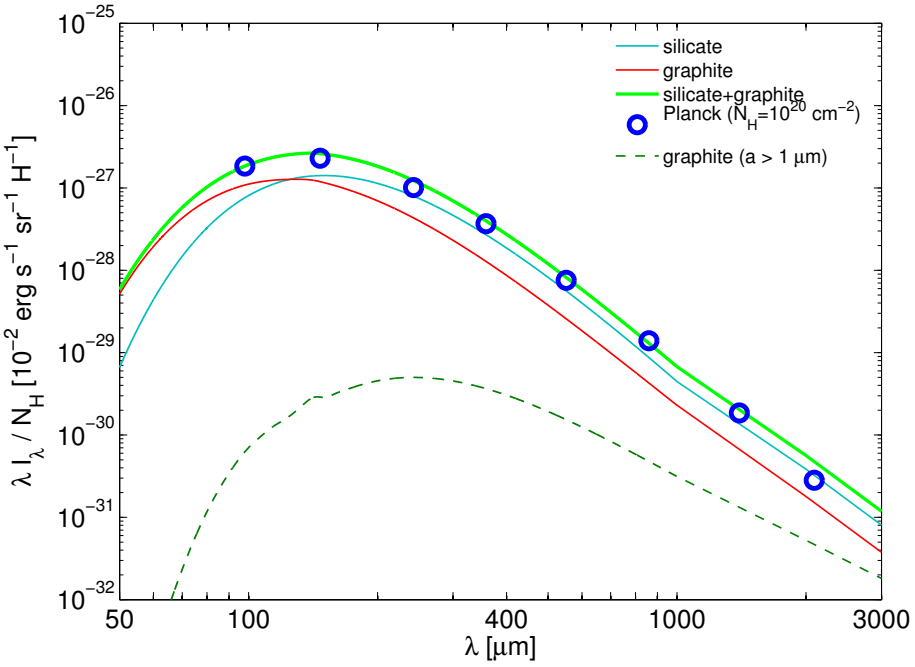

Figure 5.8 Comparison of our model to the observed emission from *Planck*, in the model (1).

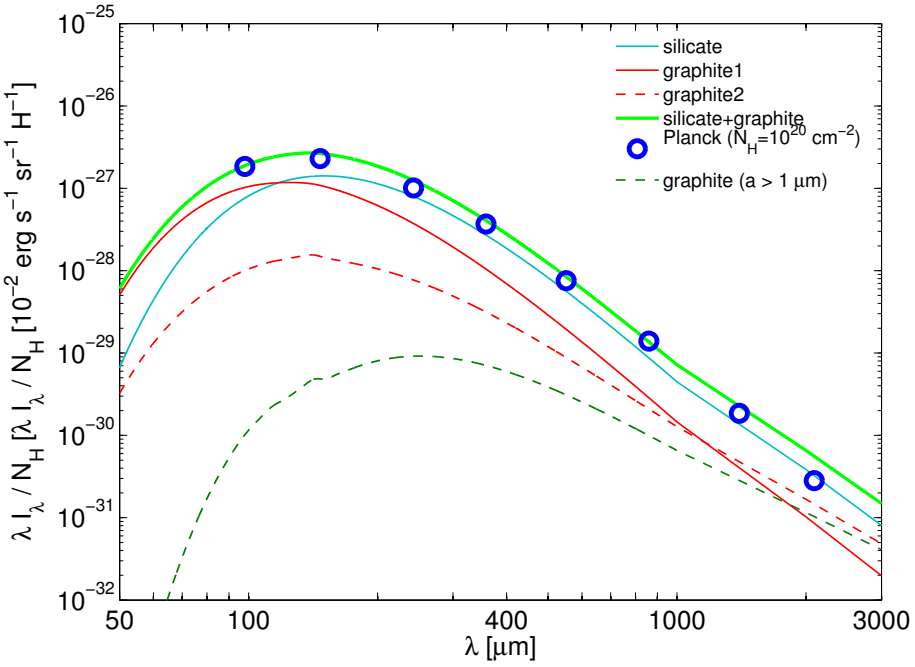

Figure 5.9 Comparison of our model to the observed emission from *Planck*, in the model (2).

5.2.4 Elemental abundance

The interstellar abundance of silicon and carbon are unknown. They are often assumed to be that of solar ($[\mathrm{Si/H}]_\odot \sim 35.5 \pm 3.6$ ppm and $[\mathrm{C/H}]_\odot \sim 295 \pm 36$ ppm, Asplund et al. 2009). Here, we calculated the mass fraction for silicate ($M_{\mathrm{sil}}/M_{\mathrm{H}}$) and graphite ($M_{\mathrm{gra}}/M_{\mathrm{H}}$) from our models. The calculation for dust component i is carried out by:

$$M_i/M_H = \frac{4}{3}\frac{\rho_i}{m_H}\pi \int a^3 \frac{1}{n_H}\frac{dn_i}{da}da \tag{5.9}$$

where ρ_i is the density of silicate and graphite (3.5 g cm^{-3} and 2.24 g cm^{-3}, respectively), m_H is the mass of hydrogen atom (1.67×10^{-24} g). The model requires a total silicate mass (relative to hydrogen) of $M_{\mathrm{sil}}/M_{\mathrm{H}} \sim 6.72 \times 10^{-3}$ and a total graphite mass (relative to hydrogen) $M_{\mathrm{gra}}/M_{\mathrm{H}} \sim 5.87 \times 10^{-3}$ and $M_{\mathrm{gra}}/M_{\mathrm{H}} \sim 6.26 \times 10^{-3}$ for model (1) and model (2), respectively. We also calculated the elemental abundance for silicon by assuming that all silicons are depleted into $MgFeSiO_4$ whose mass number per structural unit of 172, because Si, Mg, and Fe have similar abundances in the Sun (Savage & Sembach 1996). Then, the elemental abundance for silicon is evaluated to be $[\mathrm{Si/H}] \sim 39.0$ ppm. As for the abundance of carbon, its mass number per structural unit is 12, then we derived $[\mathrm{C/H}] \sim 488$ ppm and 521 ppm for model (1) and model (2), respectively. Our model requires too much C compared to solar's, even though Si abundance is consistent with that of solar.

However, we note that Parvathi et al. (2012) measured C abundance along 16 Galactic interstellar sightlines and found that gas-phase abundance of C varies from one sightline to another, with 1/3 of the sightlines having their gas-phase C/H abundance exceeding the solar C/H abundance. One of them has a gas-phase C/H abundance of 464 ± 57 ppm which is comparable to the total C/H abundance of our models.

5.2.5 Derivation of albedos

Calculation from models

In previous section, we tested our model by comparing with interstellar extinction and *Planck* observation. The results of investigation did not show any contradiction to both of them. Here, we demonstrated the calculation of albedos with our dust models. The albedo is calculated from the the weighted average of cross section and

the number density of grains corresponding to its size a by assuming that all size of dust grains are completely mixed in interstellar medium. Thus, the calculation of albedo $\gamma(\lambda)$ is carried out by

$$\gamma(\lambda) = \frac{\int \sigma_{ext}(\lambda, a)\,\omega(\lambda, a)\frac{1}{n_H}\frac{dn}{da}da}{\int \sigma_{ext}(\lambda, a)\frac{1}{n_H}\frac{dn}{da}da} \tag{5.10}$$

Here, $\sigma_{ext}(\lambda, a)$ is the cross section of total extinction which is defined by $\pi a^2 Q_{ext}(\lambda, a)$, $\omega(\lambda, a)$ is the ratio of scattering efficiency $Q_{sca}(\lambda, a)$ to extinction efficiency $Q_{ext}(\lambda, a)$ of dust grains as a function of λ and a, then given by

$$\omega(\lambda, a) = \frac{Q_{sca}(\lambda, a)}{Q_{ext}(\lambda, a)} \tag{5.11}$$

Calculated albedos are shown in Figure 5.11 with the label of "model (1)" and "model (2)". We also plotted albedos of 1 μm graphite grains. For 1 μm graphite, albedo spectrum has a peak around 1.4 μm and increase toward longer wavelength, due to the resonance bumping of Mie-scattering. If the dust size distribution does not follow power-law and it has an eccentric abundant population of graphite grains around $a \sim 1$ μm, it would show better agreement with measured albedos.

Derivation from DGL spectrum

We also derived near-infrared albedos by using our DGL spectrum to compare with created models and previous measurements of near-infrared albedos. In order to derive the near-infrared albedo, we utilized following relation.

$$\frac{I_{DGL,NIR}}{I_{DGL,opt}} = \frac{\gamma_{NIR}}{\gamma_{opt}} \cdot \frac{I_{ISRF,NIR}}{I_{ISRF,opt}} \cdot \frac{\tau_{NIR}}{\tau_{opt}} \tag{5.12}$$

where $I_{DGL,NIR}/I_{DGL,opt}$ presents the near-infrared to optical color of the DGL which is determined by the ratio of DGL intensity in near-infrared (I and H-band) to optical bands excluding a bumping data point of V-band. $I_{ISRF,NIR}/I_{ISRF,opt}$ is near-infrared to optical color of ISRF which is determined by spectrum of Bruzual & Charlot 2003. τ_{NIR}/τ_{opt} presents the ratio of optical depth in near-infrared to optical, i.e, ratio of extinction, which is derived in previous sections by using our dust models. Each term in equation (5.11) is derived by dividing the value in 1.1 μm or 1.6 μm by

averaged value from B-band to R-band ($\sim$ 0.4–0.7 μm). Then, we get the albedo color $\gamma_{NIR}/\gamma_{opt}$, and the optical albedo could be determined from weighted mean of literature values in the range of 0.4 to 0.7 μm ($\gamma_{opt} = 0.608 \pm 0.032$), we can derive the albedos at 1.1 and 1.6 μm. which are shown in Figure 5.2 with the literature values from optical to near-infrared. The light blue dashed curve labeled albedo (1) is derived by using extinction curve of model (1) and DGL spectrum. The green dashed curve labeled albedo (2) is derived by using extinction curve of model (2) and DGL spectrum. We summarized the result of albedos in Table 5.1. The derived albedos shows redder color than a model of WD01 and consistent with our model albedo spectrum, which suggest the existence of micrometer sized grains.

We note that equation (5.12) is applicable for optically thin case, which is almost satisfied because the DGL in MBM 32 is effectively determined by the linear-fit at low surface brightness region of $I_{100\mu\mathrm{m}} < 5$ MJy sr^{-1} , corresponding to $\tau_{0.55\mu\mathrm{m}} < 0.8$ (see Table 4.1). Consideration of the optical depth effect on DGL spectrum is shown in next subsection.

Consideration of scattering asymmetry

Our target MBM 32 is located to be less than 270 pc apart from Sun (Witt et al. 2008). At the Galactic latitude of 40°, the cloud is less than 170 pc apart from the Galactic plane which is comparable to the scale height of stellar distribution in the Galaxy. Therefore, ISRF may not be isotropic in the neighborhood of MBM 32. Here, we considered the anisotropic scattering effect on the derivation of near-infrared albedo from DGL color. Henyey & Greenstein (1941) introduced a scattering phase function which is expressed as a function of asymmetry parameter g whose range from $-1 < g < 1$:

$$\Phi(\theta) = \frac{1}{4\pi} \frac{1 - g^2}{(1 + g^2 - 2g\cos\theta)^{3/2}} \tag{5.13}$$

where θ denotes the scattering angle from the forward direction. $g = 0$ means that the fairly isotropic scattering, $g = 1$ corresponds to the completely forward scattering, and $g = -1$ corresponds to the completely backward scattering. Using the scattering phase function, asymmetry parameter g is defined by integration of its forward projection over the solid angle as follows:

$$g = \int_{4\pi} \Phi(\theta) \cos\theta d\Omega \tag{5.14}$$

Adopting the Henyey & Greenstein (1941) phase function for interstellar scattering, Jura (1979) numerically calculated the scattered light intensity toward the region of optical depth τ and Galactic latitude $|b|$, illuminated by an infinite homogeneous disk which locates at $b = 0°$. Bernstein et al. (2002) practically rewrote the intensity of DGL for particular use as:

$$I_{DGL} = \frac{\gamma}{1-\gamma} I_{ISRF} \left[1 - e^{-(1-\gamma)\tau}\right] \left(1 - 1.1g\sqrt{\sin|b|}\right) \tag{5.15}$$

where b donates Galactic latitude. We also approximate equation (5.15) for optically thin case as:

$$I_{DGL} \approx \gamma I_{ISRF} \tau \left(1 - 1.1g\sqrt{\sin|b|}\right) \tag{5.16}$$

Using equation (5.16), we derived near-infrared albedo relatively to optical value with asymmetry parameter g from our dust model which is calculated as:

$$g(\lambda) = \frac{\int \sigma_{sca}(\lambda, a)\, g'(\lambda, a) \frac{1}{n_H} \frac{dn}{da} da}{\int \sigma_{sca}(\lambda, a) \frac{1}{n_H} \frac{dn}{da} da} \tag{5.17}$$

where $\sigma_{sca}(\lambda, a)$ is the scattering cross section which is defined by $\pi a^2 Q_{sca}$, $g'(\lambda, a)$ is the asymmetry parameter of single grain with radius a which is calculated from Draine's code. Calculated asymmetry parameter is shown in Figure 5.10. Derived albedo from equation (5.16) is summarized in Table 5.1.

Table 5.1 Summary of the albedos, albedo (1) and albedo (2) are the derived one using our DGL spectrum.

	$\gamma_{1.1\mu m}/\gamma_{opt}$	$\gamma_{1.6\mu m}/\gamma_{opt}$	$\gamma_{1.1\mu m}$	$\gamma_{1.6\mu m}$	$\gamma_{1.1\mu m}/\gamma_{1.6\mu m}$
model (1)	1.22	1.15	0.71	0.67	1.09
model (2)	1.20	1.14	0.70	0.66	1.05
albedo (1) w/o g	—	—	0.57 ± 0.06	0.55 ± 0.06	1.04 ± 0.15
albedo (2) w/o g	—	—	0.60 ± 0.07	0.61 ± 0.07	0.98 ± 0.16
albedo (2) w/ g	—	—	0.74 ± 0.08	0.81 ± 0.09	0.91 ± 0.16
WD01	0.91	0.79	0.60	0.48	1.25

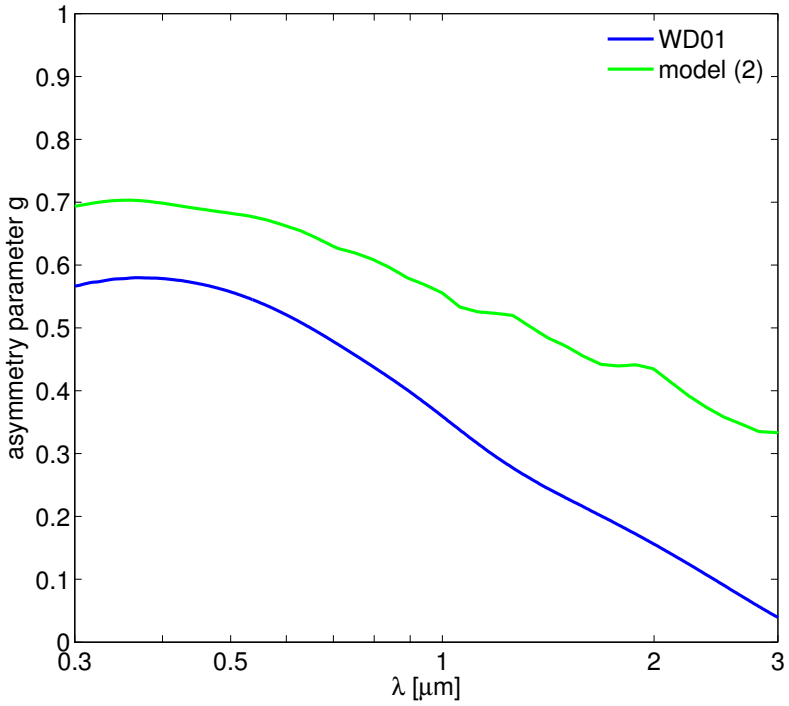

Figure 5.10 Wavelength dependence of scattering asymmetry parameter g. Light green solid curve indicates the calculated g from our model, blue solid one indicates one from WD01 original dust model.

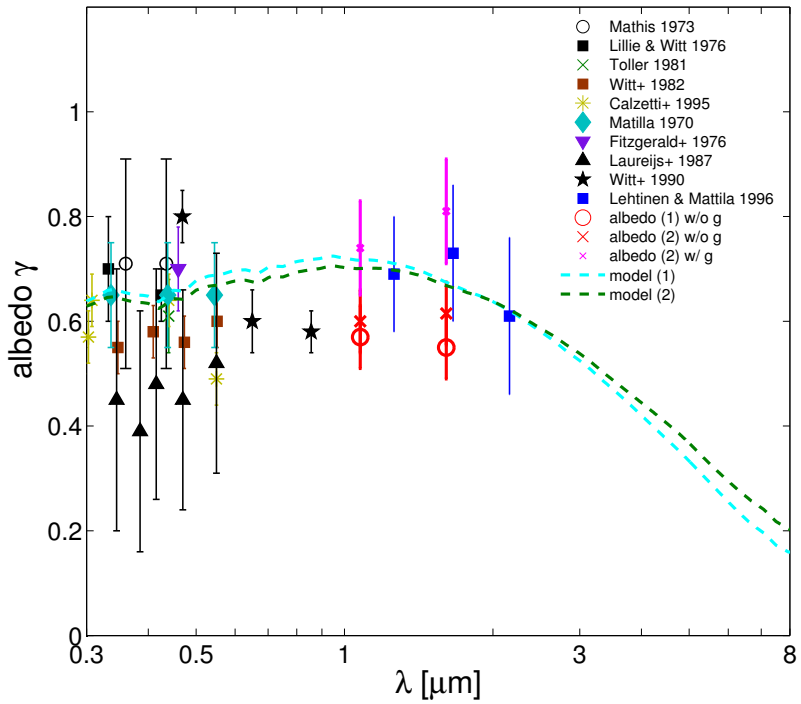

Figure 5.11 The spectra of albedos. The light blue curve is the calculated albedo spectrum with the size distribution of model (1), the green curve is also calculated spectrum but for model (2). Red symbols indicate the derived near-infrared albedos by using the DGL spectrum, albedo (1) and albedo (2) are derived by using extinction curve of model (1) and model (2), respectively. Megenta symbols also indicate one derived from the DGL spectrum, but considering the non-zero scattering asymmetry parameter.

5.2.6 Calculation of DGL spectrum

The last verification of applicability of the proposed dust model with micrometer sized graphite grains is whether it reproduces the spectrum of DGL over a wide range from optical to near-infrared. Based on equation (1.4) and equation (5.14), spectrum of DGL $I_{DGL}(\lambda)$ is calculated by assuming single scattering. We employed the BC03 as a spectrum of ISRF $I_{ISRF}(\lambda)$. Derived spectra of DGL are shown in Figure 5.12 with current works for DGL, which is normalized by $I_{100\mu\mathrm{m}} = 1$ MJy sr^{-1}. Figure 5.12 indicates the DGL spectrum for isotropic scattering model with several optical depth which is expressed by equation (1.4), and Figure 5.13 indicates one for the scattering model which interstellar dust illuminated by an infinite homogeneous disk. The light green curve in both Figure 5.12 and Figure 5.13 represents the spectrum from original WD01 model, which shows bluer color than the measured DGLfs even though anisotropic effect on scattering is taken into account. Our model spectra for isotropic scattering shows better agreement with measured near-infrared color of 1.1 to 1.6 μm and near-infrared to B-band, g-band, but the anisotropic one would agree with the measured DGL spectrum, if we reduce the micrometer sized grains toward smaller size. It is a solution to reduce the confliction with abundance constraint. It is also seen in the DGL spectrum, V-band (0.55 μm) value exceeds roughly twice of model spectra. For the possibility of excess, it might be coming from extended red emission (ERE), which is a broad-band emission from interstellar dust grains in 0.5 to 0.9 μm spectral range, which peaks around 0.6 μm. It is thought that ERE is caused by the interaction of far-UV photons (>10.5 eV) with interstellar dust (Witt & Schild 1985; Darbon et al. 1999; Witt et al. 2006). The possible existence of ERE in diffuse clouds has been reported by some authors (Guhathakurta & Tyson 1989; Gordon et al. 1998; Witt et al. 2008; Matsuoka et al. 2011; Ienaka et al. 2013). Furthermore, Smith & Witt (2002) found that the ERE peak wavelength is closely correlated with the local density of the far-UV radiation field.

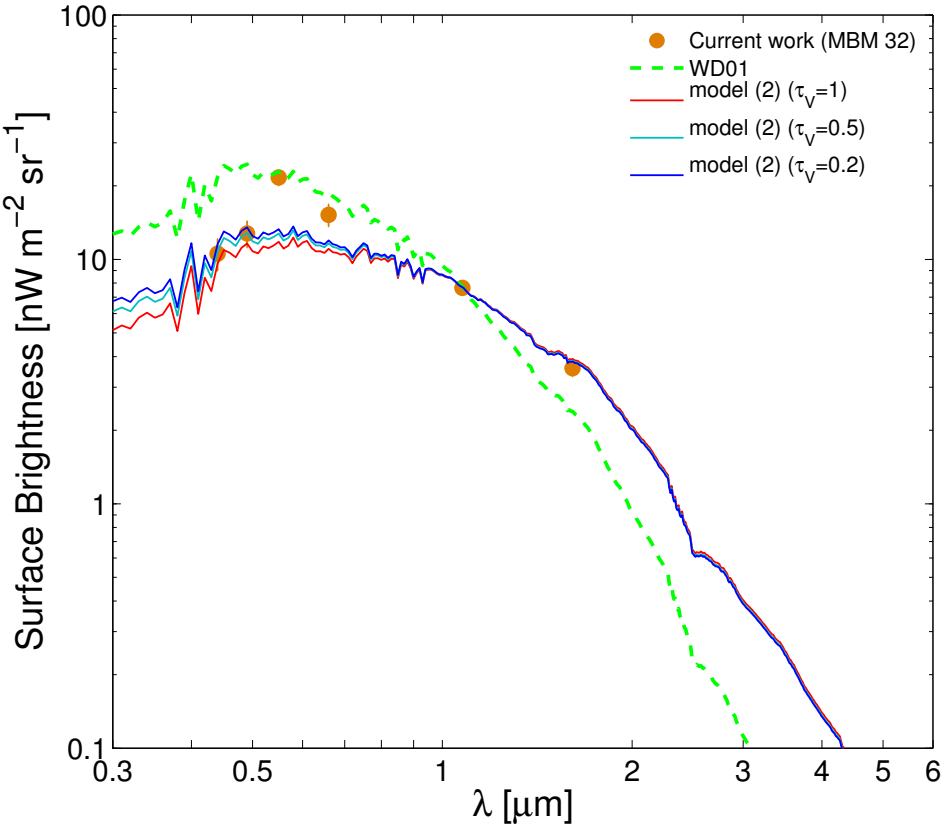

Figure 5.12 The spectra of DGL for isotropic scattering calculated by equation (1.4). Orange symbols indicate the derived DGL in MBM 32 normalized by $I_{100\mu\mathrm{m}} = 1$ MJy sr^{-1}. Solid curves are the calculated spectrum for non-zero value of optical depth with the size distribution of the model (2) assuming the single isotropic scattering of dust grains. Dashed light green curve also indicates the spectrum from original WD01 dust model.

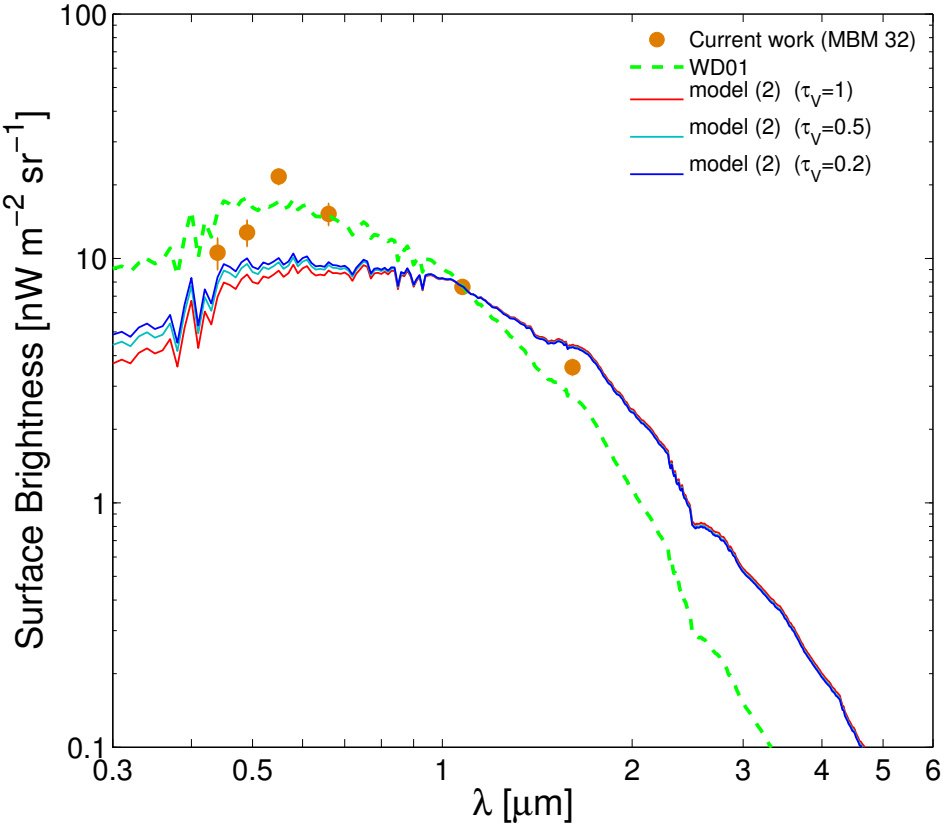

Figure 5.13 The spectra of DGL by considering non-zero scattering asymmetry parameter using equation (5.15). Orange symbols indicate the derived DGL in MBM 32 normalized by $I_{100\mu\mathrm{m}} = 1$ MJy sr^{-1}. Solid curves are the calculated spectrum for non-zero value of optical depth with the size distribution of the model (2), Dashed light green curve also indicate the spectrum from original WD01 dust model using equation (5.16).

5.3 Origin of large grains

In this chapter, based on high near-infrared albedos and flat structure of extinction curve, we considered an extra population of micrometer sized graphite grains. we found that they are reasonable for explaining both the DGL and interstellar extinction curve in mid-infrared, and suggest that micrometer sized grains are expected to exist not in Galactic center, Galactic plane, star forming regions, but also in high-latitude local diffuse cloud. We considered two cases of grain size distribution, one is the single power-law, another is two separated distribution of sub-micrometer sized and micrometer sized grains. The latter case sounds to be unrealistic phenomena, but best agree with extinction curve and near-infrared albedos. If there really exist large populations of interstellar dust, what is the origin of them?

The interstellar dust grains are thought to originate from supernova ejecta and mass -loss wind from red super giants. For the supernova origin, after the production of dust grains, they are destroyed in the ionized hydrogen gas which is swept by the shock wave of explosion. Theoretical calculations by Nozawa et al. (2006, 2007) show that the evolution of the dust size in the supernova remnants significantly varied according to the initial radius of the grains. The newly formed dust grains encounter the reverse shock, they acquire the high velocities relative to the gas and penetrate into the hot gas created by the passage of the reverse shock and forward shock. These dust grains are eroded by the kinetic sputtering and are also decelerated by the drag force of the gas. Small grains ($<$0.01 μm) decelerate efficiently, and become trapped in the hot gas, where they are efficiently destroyed by thermal sputtering. On the other hand, large grains ($>$1 μm) can maintain their high velocities, pass through the shocked gas and the outwardly expanding shock front, and injected into the interstellar space without significant destruction. Therefore, final size distribution of dust grains are expected to shift toward larger size (up to a few microns) than their initial size distribution. However, for example in the type IIb supernova which does not have thick outer layer of hydrogen gas, the dust grains are expected to be injected by keeping their initial size distribution without significant destruction of sub-micrometer grains.

For red super giants origin, dust grains are produced by a stellar wind and develop optically thick circumstellar dust shells by condensation of solid particulates in the outflowing gas. Yasuda & Kozasa (2012) investigated the formation of silicon carbide

grains in the framework of dust-driven wind around carbon-rich asymptotic giant branch (C-rich AGB) stars, and they suggested that the average radius of dust ejected from AGB stars are likely to be as large as $\sim 0.1 - 1.0$ μm, which is narrower range of size distribution than that from supernova ejecta. Such a difference of origins for dust grains would make a wide range size distribution of interstellar dust and might give a multi size distributions.

On the other hand, after the production of interstellar dust, grain growth is thought to be occurred by the accretion of gas-phase heavy elements onto pre-existing dust particles. Hirashita et al. (2013) presented the calculation of grain size growth in the interstellar clouds by accretion and coagulation. Their result suggested that the grain growth is more efficient for a higher gas density, a higher metallicity, and a smaller grains, which means the size distribution would become larger and narrower especially in gas dense regions. If the spectrum of DGL is accurately measured in various regions (e.g., on the galactic plane, nearby star forming regions, local molecular clouds) of our galaxy, and we could quantitatively investigate the variation of DGL, we would reveal what the effective factor to determine size distribution of interstellar dust is, when the interstellar dust in our galaxy was formed.

Chapter 6

Upper limit on near-infrared EBL

6.1 Application of the Dark Cloud Method

CIBDC 3 and CIBDC 5 are observed for the EBL detection, however CIBDC 5 is not suitable for the applying the dark cloud method, because the pixels available for the dust dense regions are significantly reduced by the procedure of point source masking. Here, we applied the dark cloud method to CIBDC 3 field.

The total diffuse component $I_{obs}(\tau)$ through the interstellar dust grains with optical depth τ can be explained using equation (6.1)

$$I_{obs}(\tau) = I_{ZL} + I_{ISL} + I_{EBL}e^{-\tau} + \frac{\gamma}{1-\gamma} I_{ISRF}\left[1 - e^{-(1-\gamma)\tau}\right] \tag{6.1}$$

where I_{ZL} is the isotropic component of the zodiacal light, I_{ISL} is the isotropic faint starlight contributions, and I_{EBL} is the background light coming from behind the dark clouds. The optical depth at 1.1 and 1.6 μm is estimated from the $E(B-V)$ map based on $IRAS$ and DIRBE/$COBE$ observations and observed extinction curve (Fitzpatrick 1999). We can then take the differences between all data points on the cloud and the optically thin region neighboring the cloud, which has $\tau = \tau_0$ as follows:

$$I_{obs}(\tau) - I_{obs}(\tau_0) = I_{EBL}\left(e^{-\tau} - e^{-\tau_0}\right) - \frac{\gamma}{1-\gamma} I_{ISRF}\left[e^{-(1-\gamma)\tau} - e^{-(1-\gamma)\tau_0}\right] \tag{6.2}$$

Using this differential method, the spatially uniform contributions I_{ZL} and I_{ISL} in front of the can be canceled. Before operating the fitting with equation (6.2), we extract the linear coefficient in order to reduce the parameter I_{ISRF} by using optically thin relation of equation (6.3).

$$I_{obs}(\tau) \approx I_{ZL} + I_{ISL} + I_{EBL} + (\gamma I_{ISRF} - I_{EBL})\,\tau \tag{6.3}$$

The result of linear fitting using equation (6.3) is shown in Figure 6.1. We assume that the region for $(1-\gamma_{1.1\mu m})\tau_{1.1\mu m} < 0.12$ is optically thin, and take the weighted mean of the linear coefficients in our three fields located at nearly the same galactic coordinates, i.e., same intensity of ISRF. The derived slope is $\gamma I_{ISRF} - I_{EBL} = 139.1 \pm 4.8$, 96.5 ± 7.1 nW m^{-2} sr^{-1} for the I- and H-bands, respectively. Following this process, we use the value of albedo γ reported by Lehtinen & Mattila (1996) into fitting function (6.2) which are shown in Figure 6.2.

Lehtinen & Mattila (1996) derived the near-infrared albedo of the interstellar dust grains measuring the Thumbprint Nebula in the J, H, and K bands. In their calculation, the albedo was only weakly dependent on the value of the asymmetry parameter of the grains, g. They concluded that the albedo values at 1 to 2 μm were restricted to the ranges from 0.6 to 0.8 for $g < 0.8$.

We summarize our EBL results for albedos 0.6, 0.65, 0.7, 0.75 and 0.8 in Table 6.1 with parameter errors and reduced χ^2 values for degree of freedom DOF$_\lambda$. According to χ^2 probability of fitting, 1.6 μm result ($P(\chi^2;\mathrm{DOF}) < 1\%$) should be rejected, but for 1.1 μm ($P(\chi^2;\mathrm{DOF}) \sim 16\%$), fitting model is acceptable. Thus, we provided 1σ upper limit of 38.2 ($29.8 + 8.4$) on EBL at 1.1 μm, established for $\gamma = 0.6$.

It is also seen in Table 6.1, our result is strongly dependent on the value of albedo. If albedo changes 10%, EBL changes 15 nW m^{-2} sr^{-1}. Nevertheless, our result implies that EBL measurement using dark cloud method can constrain the EBL intensity within at least ~ 10 nW m^{-2} sr^{-1}, if albedo is determined with 3% accuracy.

Table 6.1 Summary of the EBL results obtained by using the dark cloud method for several albedo values γ. Each error indicate 1σ parameter error. DOF and reduced χ^2 are also presented.

albedo γ	I_{EBL} 1.1 μm nW m^{-2} sr^{-1}	I_{EBL} 1.6 μm nW m^{-2} sr^{-1}	DOF$_{1.1\mu m}$	DOF$_{1.6\mu m}$	χ^2/DOF$_{1.1\mu m}$	χ^2/DOF$_{1.6\mu m}$
0.60	29.8 ± 8.4	36.4 ± 20.9	51	44	1.22	1.58
0.65	13.9 ± 7.3	19.8 ± 18.0	51	44	1.20	1.57
0.70	1.4 ± 6.3	10.8 ± 15.5	51	44	1.20	1.57
0.75	< 0	2.0 ± 12.9	51	44	1.21	1.57
0.80	< 0	< 0	51	44	1.21	1.58

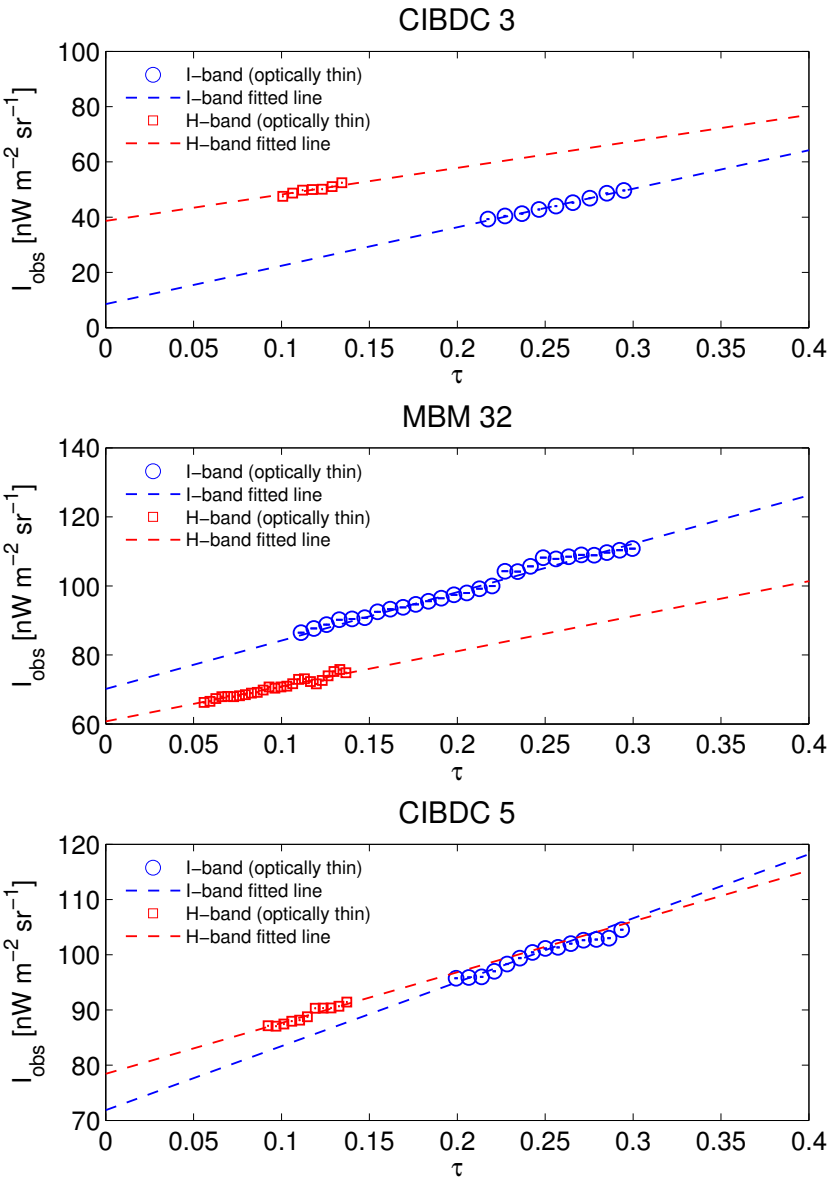

Figure 6.1 The result of linear fitting for optically thin regions. From top to bottom: CIBDC 3, MBM 32, and CIBDC 5's. Red symbols and blue symbols are I and H-band points, respectively.

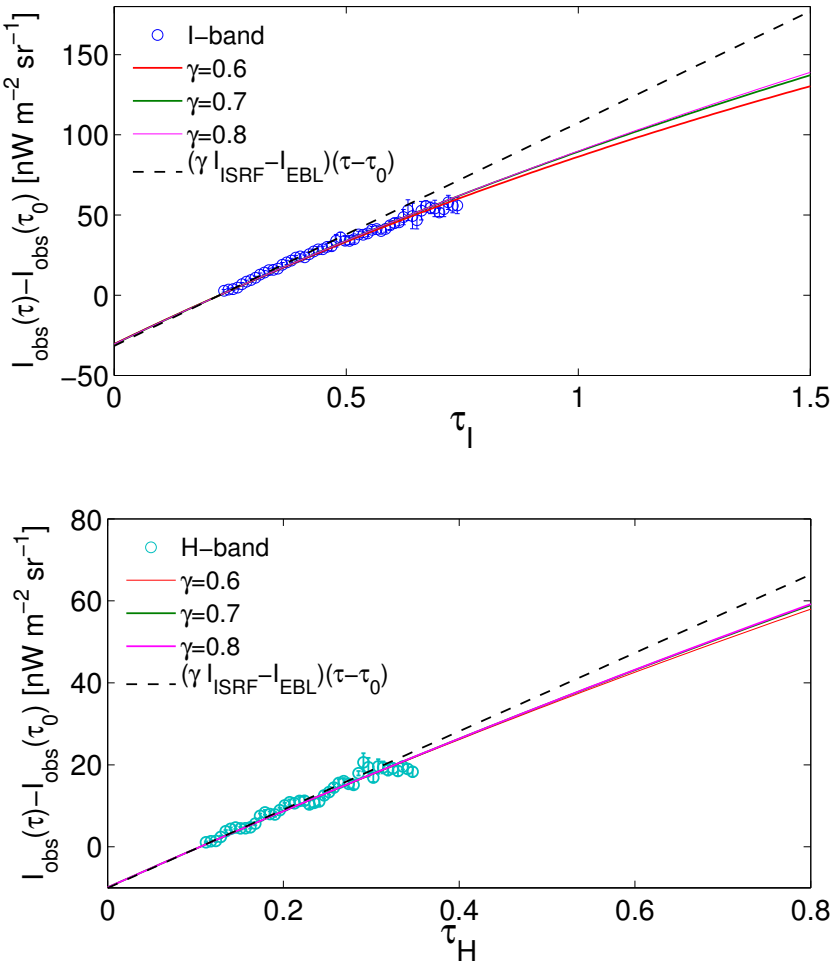

Figure 6.2 The observed $I_{obs}(\tau) - I_{obs}(\tau_0)$ for CIBDC 3 and best-fit curves for them, in case of $\gamma = 0.6, 0.7$, and 0.8.

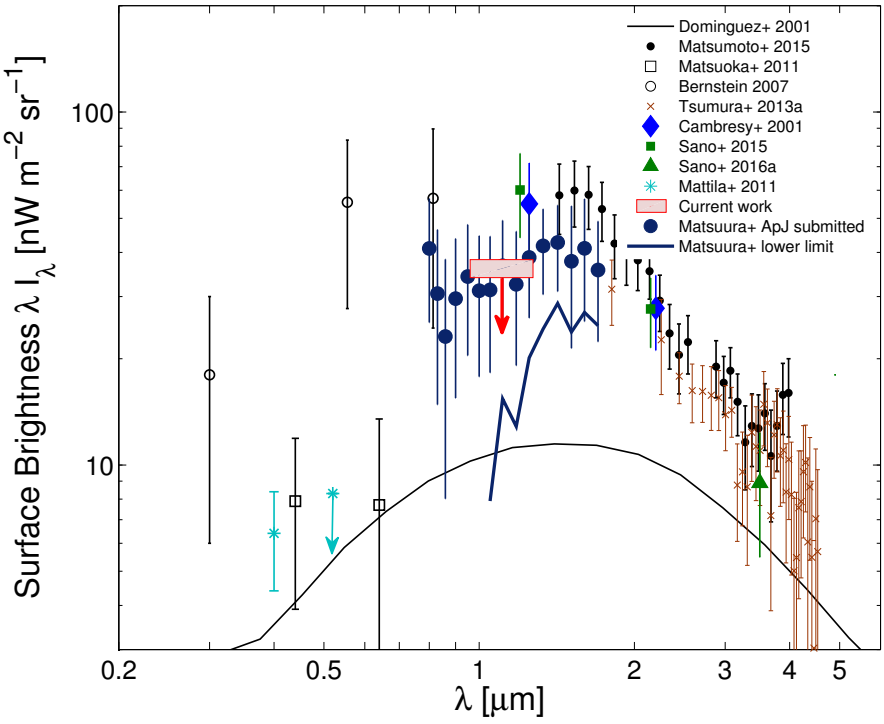

Figure 6.3 Surface brightness of EBL as a function of wavelength λ. The red arrows indicate the derived upper limit from this study (the center value, plus 1σ standard error in Table 6.1), assuming an interstellar dust albedo $\gamma = 0.6$. The shaded rectangle indicates where the range might have been changed by contribution of faint stars behind the cloud. The black solid curve indicates the estimated spectrum of integrated light from individual extragalactic sources based on the galaxy count (Domínguez et al. 2011). The navy thick solid line indicates the lower limit of near-infrared EBL obtained by LRS/CIBER. The other symbols are results of previous works deriving the EBL, Cambrésy et al. (2001) (Blue filled diamonds), Bernstein (2007) (Black open circles), Matsuoka et al. (2011) (Black open rectangles), Mattila et al. (2011) (Cyan asterisks),Tsumura et al. (2013a) (Brown cross points), Matsumoto et al. (2015) (Black filled points), Sano et al. (2015) (Green filled triangles), Sano et al. (2016a) (Green filled squares).

6.2 Albedo constraint from EBL

Our analysis of EBL using the dark cloud method can provide a constraint on the value of the albedo of interstellar dust grains in a manner different from that in previous measurements of albedos. The measurements of light from extragalactic sources based on the deep galaxy counts are so deep to effectively detect all of the optical and near-infrared photons from individual galaxies. Thus, those measurements give a significant lower limit to EBL. In near-infrared range around 1 μm, the contribution of integrated light from individual extragalactic sources is estimated to be about 10 nW m^2 sr^{-1}.

On the other hand, in our analysis using dark cloud method, as summarized in Table 6.1, in case of albedos higher than 0.7, the value of EBL would be less than the integrated extra-galactic flux ($<$ 10 nW m^2 sr^{-1}). Thus, we set a limit to the albedo of $\gamma < 0.7$. The constraint does not conflict with the albedo value derived in previous chapter. Note that the estimated EBL brightness for $\gamma = 0.7$ is comparable to the integrated flux of entire galaxies as a certain lower limit of the EBL.

6.3 Comparison with other EBL measurements

In I-band, the derived upper limit appears to be lower than the level of previous measurements of Sano et al. (2015) and Cambrésy et al. (2001) at J-band. In addition, our EBL result is thought to be coupled with faint starlight behind the dark clouds. Thus, the result should be lower than plotted points shown in Figure 6.3. We calculated the contribution of the stars fainter than 2MASS limit by assuming that all of the faint Galactic stars exist behind the dark cloud using the TRILEGAL star count model (Girardi et al. 2005). The contribution of the faint stars 7.1 nW and 6.5 nW m^{-2} sr^{-1}at 1.1 μm and 1.6 μm respectively. Thus, there is the possibility that the presented upper limit would go down by a few. Our EBL result points out that the remainder of foregrounds in the previous EBL observations. On the other hand, measured EBL by Sano et al. (2015) is expected to be spatially isotropic, which means the remainder of foregrounds should be spatially isotropic and should be in front of the local dust cloud.

One candidate of isotropic foreground is ZL. In fact, a popular model of ZL by Kelsall et al. (1998) is established with making use of all-sky data of DIRBE/*COBE*,

thus it could be modelized without the separation of isotropic ZL, even though it includes a spatial variation of ZL. If all of the remainder is attributed by ZL, it is comparable to at least 3%, at most 20% of ZL intensity. However, spectral measurement of EBL from 0.8 to 1.6 μm by Matsuura et al. (ApJ submitted) shows that the spectral color of EBL is significantly redder than the spectrum of ZL. Thus, all of remainder does not originate from ZL even if it includes a part of them.

6.4 Candidates of excess emission

Matsuura et al. (ApJ submitted) also derived a lower limit for EBL by arbitrary subtraction adjusting to galaxy counts at ~ 1 μm, which is shown in Figure 6.3 with a navy thick curve. Thus, the level of near-infrared EBL should be between Matsuura et al. (ApJ submitted) and our result, corresponding to $\sim 15 - 40$ nW m^{-2} sr^{-1} at I-band, which implies that the EBL exceeds to galaxy counts.

One possibility is Galactic origin. There may exist numerous faint stars in the Galactic halo which causes isotropic background. However, the negative detection of extended halo in external galaxies was reported by Uemizu et al. (1998). In addition, the excess emission at H-band can be resolved for the external galaxies with HST/NICMOS (Thompson et al. 2007a; Thompson et al. 2007b), but detection is not reported yet. These results support that the observed excess emission originates from extragalactic sources.

For the extragalactic sources, unresolved first stars (Pop-III stars) and Pop-III galaxies are one candidate of excess emission (Santos et al. 2002; Salvaterra & Ferrara 2003; Cooray & Yoshida 2004; Dwek et al. 2005a; Madau & Silk 2005; Mii & Totani 2005; Fernandez & Komatsu 2006; Fernandez at al. 2010). However, some authors insist the difficulties in attributing the near-infrared EBL from energy output from Pop-III stars. Theoretical calculations of Dwek, Arendt & Krennrich (2005) pointed out that the light from Pop-III stars at redshift $z > 6$, makes a contribution of only ten times lower level than the galaxy counts (~ 0.1 nW m^{-2} sr^{-1}). In order to explain the excess emission with Pop-III star formation, it requires the conversion of about 10% of all baryons in the universe into Pop-III stars. In addition, indirect derivation of EBL by measuremet of the spectrum of blazars emitting γ-rays indicate that the EBL brightness is comparable to known galaxy counts. Since γ-rays are attenuated by interacting with Pop-III's photons in the propagation of the intergalactic space,

EBL intensity can be derived by assuming the intrinsic blazar spectrum.(e.g., Guy et al. 2000; Dwek & Krennrich 2005; Schroedter 2005; Aharonian et al. 2006; Albert et al. 2008; Mazin & Raue 2007; Orr et al. 2011; Meyer et al. 2012). According to the recent result of the High Energy Stereoscopic System (H.E.S.S.) experiment has offered a constraints on EBL, (Abramowski et al. 2013). Most of the γ-rays constraints on EBL at 1 to 2 μm is few times lower than the derived near-infrared EBL. It is $14.8^{+2.1}_{-1.7}$ nW m^{-2} sr^{-1} at 1.25 μm.

Besides Pop-III stars, recent studies of EBL by Cooray et al. (2012b) and Zemcov et al. (2014) suggested a model to explain the EBL by the diffuse intrahalo light (IHL) of galaxies. The IHL is generated by tidally stripped stars from their parent galaxies by mergers and collisions (Cooray et al. 2012b). Zemcov et al. (2014) estimated the contribution of IHL to the excess emission of near-infrared EBL at 1.1 and 1.6 μm. The measurement of the EBL fluctuation is one way to avoid the uncertainty of the Zodiacal Light, because the ZL is known to be spatially smooth (Pyo et al. 2012). They estimated the EBL intensity associated with the fluctuations by taking the measured fluctuation amplitude between multi-pole moment $500 < l < 2000$ obtained by subtracting estimated contributions from low-z galaxies and DGL, and multiplying by a model dependent contrast factor $I_{EBL}/\delta I_{EBL}$. For the IHL model, which has a low contrast factor, associated EBL of $7.0^{+4.0}_{-3.5}$ and $11.4^{+5.4}_{-4.8}$ nW m^{-2} sr^{-1} at 1.1 and 1.6 μm, respectively. Thus, the maximum case of total energy including the known galaxy counts presents 21.7 and 26.4 nW m^{-2} sr^{-1} at each band, which can explain the lowest case of near-infrared EBL at 1.1 μm from Matsuura et al. (ApJ submitted).

6.5 Future project for EBL measurements

The origin and the accurate level of the near-infrared EBL is not still clear from this work, and new observations are highly expected to delineate their origin. *SPHEREx* (Doré et al. 2015) with a 20 cm all-aluminum telescope with a wide 3.5° × 7° field of view will make a first all-sky near-infrared spectral survey at 0.75–4.8 μm.

KASI is also developing a Near-infrared Imaging Spectrometer for Star formation history (NISS) with a large field of view of 1.7° × 1.7° and a wavelength coverage of 0.95–3 μm. Those spectroscopic wide-field survey will accurately measure the EBL brightness by applying dark cloud method.

For the other ideal observation of EBL, a small infrared telescope, EXo-Zodiacal Infrared Telescope (EXZIT), has been proposed as one of instruments on a Solar Power Sail mission to Jupiter (Matsuura 2014). The measurement of near-infrared EBL at 5 AU will be realized in the 2020s. In 5AU, ZL foreground is expected to be lower than the ZL level in Earth's orbit, which will be able to make a strong limit for EBL.

Chapter 7

Summary and conclusions

In this thesis, we have carried out the near-infrared observations of high latitude dust clouds at 1.1 and 1.6 μm with the high photometric data obtained by MIRIS, primary to derive a accurate spectrum of DGL over a wide range from optical to near-infrared, secondary to put constraints on near-infrared EBL using dark cloud method.

For DGL, we succeeded in deriving the spectral color of DGL between optical and near-infrared range with the best ever accuracy. Our DGL result shows bluer color than the conventional dust model predicted even though anisotropic scattering is taken into account. Thus, it suggests the existence of larger size grains than the conventional dust models considers, which was also previously suggested by measurement of extinction curve and near-infrared albedo. According to those results, we extended a popular dust model by invoking an extra population of micrometer sized graphite grains and investigated its applicability to our DGL result concurrently taking account of the effects on the interstellar extinction curve and the thermal emission in the far-infrared and sub-milimeter wave.

Main conclusions of DGL study are as follows:

- Employment of micrometer sized graphite grains works well to explain a flat shape of extinction curve in 3–8 μm, and near-infrared albedos which is relatively evaluated from measured DGL spectrum and previous albedo values in optical wavelength range. In addition, the near-infrared spectrum of albedo exhibits redder color than the model prediction. Thus, our result emphasized the previous suggestion that the micrometer sized grains exists in interstellar space.

- We calculated DGL spectra from our model by considering two scattering models, one is the isotropic scattering model, and the another is the anisotropic one that the dust grains are illuminated by an infinite homogeneous disk. Isotropic scattering model with micrometer sized grains are more favorable to explain the near-infrared color of DGL than the anisotropic one. However, anisotropic one would be agree with the measured DGL spectrum by shifting the size distribution of our model toward smaller size, which can reduce the confliction with abundance constraint of carbon. The spectra also mostly agree with the measured DGL color between optical near-infrared wavelengths, besides 0.55 μm.

For EBL, we have succeeded in limiting the level of near-infrared EBL without subtraction uncertainty of ZL for the first time and demonstrated the derivations with the several step of albedo corresponding to $\gamma = 0.6$ to 0.8. Conclusions of EBL measurement are as follows.

- We obtained 1σ upper limits on the EBL brightness of 38.2 nW m^{-2} sr^{-1} at 1.1 μm, corresponding to allowable minimum albedo ($\sim$ 0.6). In other words, by assuming the integrated galaxy light (IGL) from the deep galaxy counts as the lower limit of the EBL brightness, we could determine the maximum albedo of the interstellar dust to be 0.7 at 1.1 μm. The constraint on albedos does not conflict with the one, which is derived from our DGL spectrum.

The result of EBL strongly depends on assumption of albedo values. Conversely, our first trial of the detection of near-infrared EBL using dark cloud method implies that EBL would be detected within at least $\sim$ 10 nW m^{-2} sr^{-1} error, if albedo is determined with 3% accuracy. Thus, the detailed study of scattering properties of interstellar dust grains will play a key role to constrain on the EBL intensity (in other words star formation history in the universe) by using the dark cloud method.

For future prospects of EBL measurement, wide-field and wide spectral range observations by SPHEREx and NISS is under launching. By using them, EBL will be supply more accurate data for dark cloud method. And, an observation from outside the zodiacal dust cloud is an ultimate way and ,in fact, such mission named EXZIT is planned. It will be a great help for constraining on EBL brightness in near-infrared wavelengths.

Appendix A

Systematic uncertainties of point source masking

Contamination from point sources can become a influence for the result of EBL and DGL. Here we report the systematic change which is caused by point source masking.

As written in section 3.2, we derived the point source masks for the observed images with making use of 2MASS PSC and 2σ clipping method because of incompleteness of the masking which are occurred by pointing instability of MIRIS.

First of all, in order to investigate the difference of masking effect between using 2MASS PSC and 2σ clipping, we directly compare the results of DGL which are conducted from the images whose masks are generated by following three procedures.

- A: Masked by 2MASS PSC after 2σ clipping method has been applied.
- B: Masked by 2MASS PSC.
- C: Masked by 2σ clipping method after masked by 2MASS PSC (Nominal procedure).

The distributions of pixel values with the image of CIBDC 3 (I-band) is shown in Figure A.1. As can be seen in Figure A.1, number of bright pixels are increased by method B (in the case of using only 2MASS PSC). Thus, it is proper to derive a mask using 2σ clipping method in addition to 2MASS mask. Figure A.2 also indicates the correlation between MIRIS image and 100 μm intensity map. For the low 100 μm intensity regions, the leakage from point sources appear to affect significantly and

reduce the correlation slope i.e., DGL. In the other fields, the tendencies of masking effect for each procedure are same as CIBDC 3's as summarized in TableA.1.

In the next, we performed the masking by 1.8, 2.5, 3.0σ clipping in addition to 2MASS PSC masking (Method B), to confirm whether point sources was enough to be removed by 2σ clipping and checked whether there the results of DGL are changed by a factor of σ. The result of investigation is also summarized in Table A.1. From the result, the strength of σ clipping does not signifficantly affects the result of DGL.

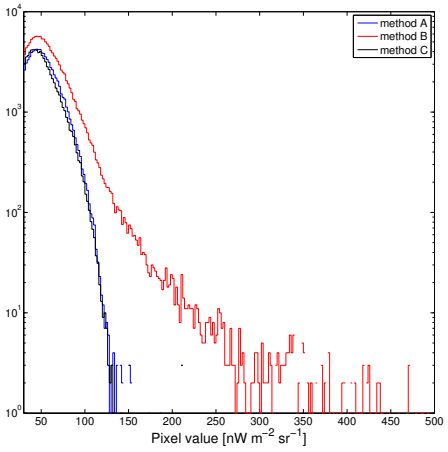

Figure A.1 Pixel distributions for three masking procedures (A), (B) and (C).

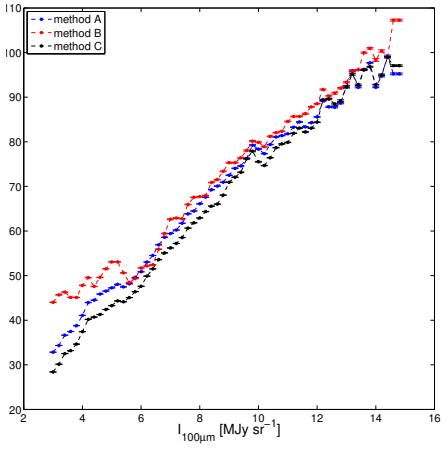

Figure A.2 Correlation between 1.1 μm and 100 μm intensity for three masking procedures (A), (B) and (C).

Table A.1 Summary of the DGL value when we applied several procedures of point source masking.

Field	λ [μm]	Method A b_λ [nW m^{-2} MJy^{-1}]	Method B b_λ [nW m^{-2} MJy^{-1}]	Method C b_λ [nW m^{-2} MJy^{-1}]	B & 3σ b_λ [nW m^{-2} MJy^{-1}]	B & 2.5σ b_λ [nW m^{-2} MJy^{-1}]	B & 1.8σ b_λ [nW m^{-2} MJy^{-1}]
CIBDC 3	1.1	6.03 ± 0.11	5.38 ± 0.29	6.23 ± 0.10	6.29 ± 0.13	6.25 ± 0.12	6.21 ± 0.12
	1.6	2.35 ± 0.09	2.08 ± 0.18	2.51 ± 0.08	2.58 ± 0.10	2.53 ± 0.10	2.48 ± 0.10
MBM 32	1.1	7.29 ± 0.36	6.44 ± 0.50	7.64 ± 0.32	7.88 ± 0.39	7.76 ± 0.38	7.64 ± 0.32
	1.6	3.33 ± 0.31	3.09 ± 0.34	3.59 ± 0.27	3.81 ± 0.30	3.66 ± 0.29	3.55 ± 0.27
CIBDC 5	1.1	6.35 ± 0.11	5.59 ± 0.24	6.56 ± 0.11	6.67 ± 0.14	6.57 ± 0.15	6.58 ± 0.14
	1.6	2.32 ± 0.12	2.11 ± 0.28	2.63 ± 0.10	2.79 ± 0.12	2.68 ± 0.15	2.63 ± 0.12

Appendix B

Calculation of ISL

ISL is the cumulative brightness of Galactic stars which is fainter than the limiting magnitude of MIRIS optics. The most part of contamination by Galactic stars should be removed by the procedure of pointsource masking described in section 3.2 and the ISL in front of the cloud is eliminated by dark cloud method. However, starlight coming from behind the cloud is coupled with EBL.

In order to investigate the maximum contribution of starlight fainter than 2MASS completeness limit (15.8 mag in J-band), we carried out the calculation with TRILEGAL star count model derived by Girardi et al. (2005) by assuming that all of the faint stars locate behind the diffuse cloud. The model in TRILEGAL includes main components of Milky Way such as thin and thick disks, halo and buldge, each component contains stellar population which is defined by star formation rate and age-metalicity relation. In Girardi et al. (2005), they discussed on the model reproducibility to the observations in comparison with deep star count. As the result, they found that the difference between the model and observations is less than 30%.

According to their investigation of discrepancies, we checked the difference between TRILEGAL and 2MASS star count for CIBDC 3 field. As the result, there is $\sim 20\%$ discrepancy between TRILEGAL model and 2MASS star counts. In order to quantify the contribution of ISL, we scaled the TRILEGAL star counts to 2MASS star counts where the magnitude of stars are brighter than 15.8 mag in J-band. Estimated scaling factor from TRILEGAL to 2MASS star counts is 1.18. The star count and cumulative brightness of scaled TRILEGAL count are shown in Figure B.1. Using the estimated J-band scaling factor, we calculated the ISL contribution for I and H-band, and we obtained ISL contributions of 7.1 and 6.5 nW m^{-2} sr^{-1} for I and H-band, respectively.

They are account for less than 20% of EBL upper limits.

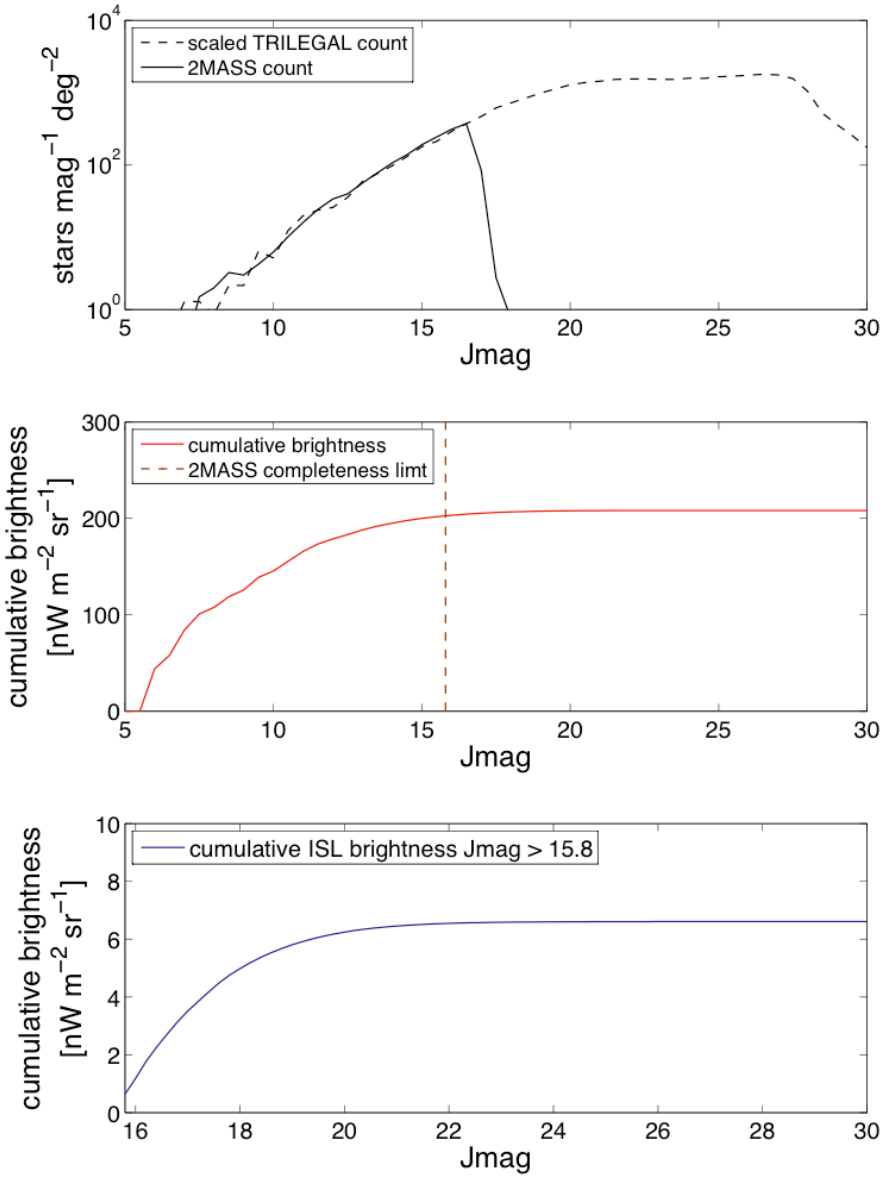

Figure B.1 Star counts and cumulative brightness of ISL. The top panel indicates the star count by 2MASS PSC and scaled TRILEGAL model. The middle panel indicates the cumulative brightness calculated by scaled TRILEGAL count. The bottom panel also indicates but for fainter than 2MASS completeness limit (J-band magnitude > 15.8)

Appendix C

Uncertainty of ZL removal

In section 3.3, we employed the model by Kelsall et al. (1998) to remove the ZL gradient from our observed images. As described in Kelsall et al. (1998), the uncertainty of their model is estimated as the intensity difference between the two ZL models (two IPD distributions) at the north Galactic pole (NGP) where the deviation is reported to be the largest. This uncertainty is ~ 15 nW m^{-2} sr^{-1} at J-band (1.25 μm) which corresponds to 2%, 5%, and 5% absolute differences in CIBDC 3, MBM 32 and CIBDC 5.

Here, we investigated the effect of ZL subtraction on the DGL and the EBL results. We considered a few % differences by changing the factor of the ZL brightness of f_{ZL} as follows:

$$I_{obs}(\lambda) = I_{sky}(\lambda) - f_{ZL}(\lambda) I_{ZL}(\lambda) \tag{C.1}$$

where $I_{sky}(\lambda)$ is the total diffuse sky brightness in our field, $I_{ZL}(\lambda)$ is absolute brightness of ZL from Kelsall et al. (1998). And, we correlated $I_{obs}(\lambda)$ with $I_{100\mu\mathrm{m}}$, and estimated the systematic differences of linear coefficients b_λ in equation (4.5). Figure C.1 shows the comparison between near-infrared brightness and 100μm brightness by considering 2%, 5%, 5% changes in ZL brightness for CIBDC 3, MBM 32 and CIBDC 5, respectively. The linear-fit parameters are shown in Table C.1. Solid lines in each panel indicate the correlation slope with the subtraction of nominal model value, dashed lines are fitted one with the subtraction of the additional ZL value (nominal plus a few %): alternate long and short dashed lines are ones with the subtraction of the reduced ZL value (nominal minus a few %). As shown in Figure C.1 and Table C.1, a few % of difference for removal of ZL gradient in FOV hardly affect to the DGL results ($< 2\%$).

We also summarized the effect on upper limit of EBL in Table C.2. The EBL result is changed by the changes in ZL value because the slight change of the slope in the optically thin region ($\gamma I_{ISRF} - I_{EBL}$) affect to EBL result.

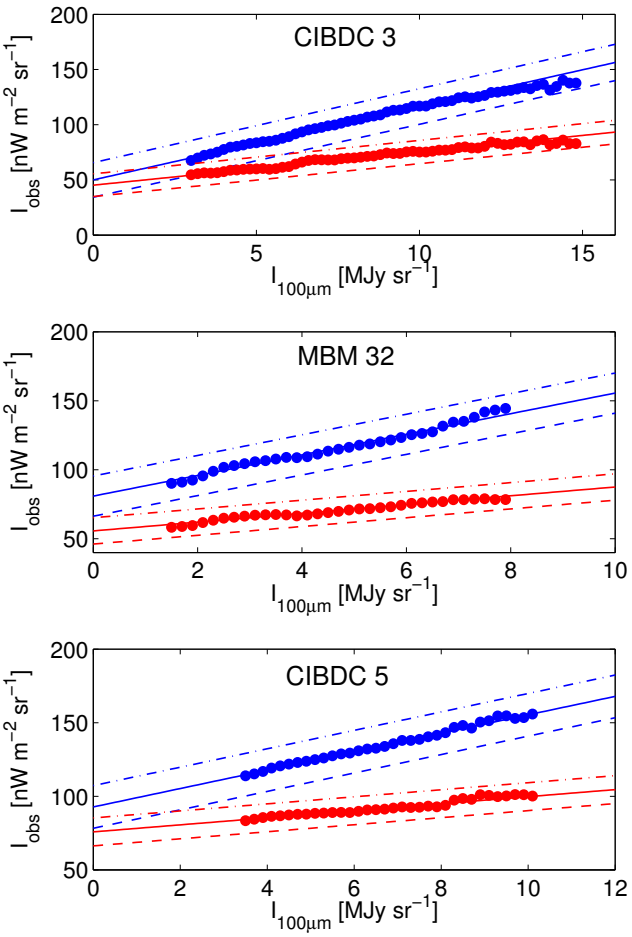

Figure C.1 Comparison between near-infrared brightness and 100 μm brightness (blue:I-band, red:H-band). Solid lines are fittedones from our nominal data, dashed/alternate long and short dashed lines are one from subtraction of additional/reduced ZL value (see text).

Table C.1 Summary of the DGL when we changed a few % of model values of ZL.

Field	range of $I_{100\mu m}$ [MJy sr^{-1}]	f_{ZL}	$a_{1.1\mu m}$ [nW m^{-2} sr^{-1}]	$b_{1.1\mu m}$ [nW m^{-2} MJy^{-1}]	$a_{1.6\mu m}$ [nW m^{-2} sr^{-1}]	$b_{1.6\mu m}$ [nW m^{-2} MJy^{-1}]
CIBDC 3	≤ 15	1	50.3 ± 3.1	6.23 ± 0.10	42.4 ± 2.8	2.51 ± 0.09
	≤ 15	1.02	34.4 ± 3.0	6.13 ± 0.09	31.8 ± 2.8	2.46 ± 0.09
	≤ 15	0.98	66.1 ± 3.1	6.32 ± 0.12	53.0 ± 2.8	2.54 ± 0.09
MBM 32	≤ 7	1	84.5 ± 5.2	7.75 ± 0.32	60.5 ± 2.7	3.64 ± 0.27
	≤ 7	1.05	74.3 ± 5.3	7.67 ± 0.31	49.3 ± 2.7	3.60 ± 0.29
	≤ 7	0.95	98.7 ± 5.5	7.82 ± 0.32	71.6 ± 2.8	3.68 ± 0.29
CIBDC 5	≤ 10	1	95.4 ± 5.6	6.68 ± 0.36	73.2 ± 4.8	2.85 ± 0.32
	≤ 10	1.05	79.8 ± 5.8	6.60 ± 0.36	62.0 ± 4.8	2.82 ± 0.32
	≤ 10	0.95	111.0 ± 5.7	6.75 ± 0.37	85.4 ± 4.8	2.89 ± 0.33

Table C.2 Summary of the EBL for albedo $\gamma = 0.6$, when we changed a few % of model values of ZL.

f_{ZL}	I_{EBL} 1.1 μm nW m^{-2} sr^{-1}	I_{EBL} 1.6 μm nW m^{-2} sr^{-1}
1	29.8 ± 8.5	36.4 ± 20.9
1.02	22.5 ± 8.6	28.8 ± 20.5
0.98	37.3 ± 8.3	48.0 ± 20.6

Appendix D

Light scattering and absorption by spherical particles

The theory of light scattering and absorption by small particles is basic for the study of interstellar dust grains. Actually, this theory is used to calculate the SED of the DGL, the absorption cross section and the albedo of interstellar dust grains. In this appendix, I introduce the theory of scattering and absorption for spherical particles.

D.1 Grain properties

D.1.1 Cross sections and efficiency factor

When radiation interacts with the particles, a part of the radiation is absorbed and the rest part is scattered. Thus, the total amount of the radiation loss from the incident is the sum of the scattered and the absorbed components. These are generally expressed in terms of the dimensionless efficiency factors Q_{sca} and Q_{abs} for the scattering and the absorption components. The efficiency factors for the total extinction is given by

$$Q_{ext} = Q_{sca} + Q_{abs} \tag{D.1}$$

They are related to the corresponding cross sections as:

$$\sigma_{sca} = \pi {a_{\rm eff}}^2 Q_{sca} \tag{D.2}$$

$$\sigma_{abs} = \pi {a_{\rm eff}}^2 Q_{abs} \tag{D.3}$$

$$\sigma_{ext} = \pi {a_{\rm eff}}^2 (Q_{abs} + Q_{sca}) \tag{D.4}$$

where $a_{\rm eff}$ is the effective grain radius for the materials with solid volume V which does not include the volume of any voids:

$$a_{\rm eff} = (3V/4\pi)^{1/3} \tag{D.5}$$

This is a natural choice, because it relates the scattering and absorption directly to the actual volume of grain materials.

D.1.2 Dielectric function and refractive index

In order to evaluate the scattering and absorption properties of the interstellar dust grains, we need to characterize the response of the materials to the local oscillating electric and magnetic field. An applied oscillating electric field $\boldsymbol{E}(\boldsymbol{r}, t) = \boldsymbol{E_0} e^{i(\boldsymbol{k}\cdot\boldsymbol{r} - \omega t)}$ propagates through the medium with conductivity σ and the dielectric constant ϵ_L. The electric current $\boldsymbol{j}$ and the electrical displacement $\boldsymbol{D}$ are related to the electric field by

$$\boldsymbol{j} = \sigma \boldsymbol{E} \tag{D.6}$$

$$\boldsymbol{D} = \epsilon_L \boldsymbol{E} \tag{D.7}$$

These obey the Maxwell's equation

$$\nabla \times \boldsymbol{H} = \frac{1}{c}\frac{\partial \boldsymbol{D}}{\partial t} + \frac{4\pi}{c}\boldsymbol{j} \tag{D.8}$$

Using equations (D.6) and (D.7), this formula can be rewritten as:

$$\nabla \times \boldsymbol{H} = \frac{1}{c}\left(\epsilon_L + i\frac{4\pi\sigma}{\omega}\right)\frac{\partial \boldsymbol{E}}{\partial t} = \frac{1}{c}\epsilon\frac{\partial \boldsymbol{E}}{\partial t} \tag{D.9}$$

where ϵ is a complex dielectric function:

$$\epsilon = \epsilon_L + i\frac{4\pi\sigma}{\omega} \tag{D.10}$$

In this representation, the conduction by electrons are considered as a part of the dielectric medium. The dielectric constant is directly related to the optical properties. The complex refractive index of the grain m is defined as:

$$m = n + ik = \sqrt{\epsilon} \tag{D.11}$$

where n is the usual refractive index and k is the extinction coefficient.

D.2 Scattering by small particles: Size $\ll \lambda$

Consider a small spherical particles whose size smaller than the wavelength of incident light. The dipole moment $\boldsymbol{p}$ is induced in the particle is proportional to the electric field $\boldsymbol{E}$:

$$\boldsymbol{p} = \alpha \boldsymbol{E} \tag{D.12}$$

where α is the polarizability of the particle. The scattered electric field $\boldsymbol{E_{sca}}$ at a distance r ($\gg \lambda$) from the dipole is given by

$$\boldsymbol{E_{sca}} = \frac{1}{r}\frac{1}{c^2}\frac{\partial^2 \boldsymbol{p}}{\partial t^2}\sin\phi \tag{D.13}$$

where ϕ is the angle between the scattered dipole moment $\boldsymbol{p}$ and the direction of observation. In oscillating periodic field, the dipole moment is given in terms of induced dipole moment by

$$\boldsymbol{p} = \boldsymbol{p_0} e^{i(\boldsymbol{k}\cdot\boldsymbol{r}-\omega t)} \tag{D.14}$$

and thus the electric field is

$$\boldsymbol{E_{sca}} = -\frac{\alpha\omega^2}{rc^2}\boldsymbol{E_0} e^{i(\boldsymbol{k}\cdot\boldsymbol{r}-\omega t)}\sin\phi \tag{D.15}$$

We show the conceptual diagram of the wave scattering by the single dielectric particle in Figure D.1.

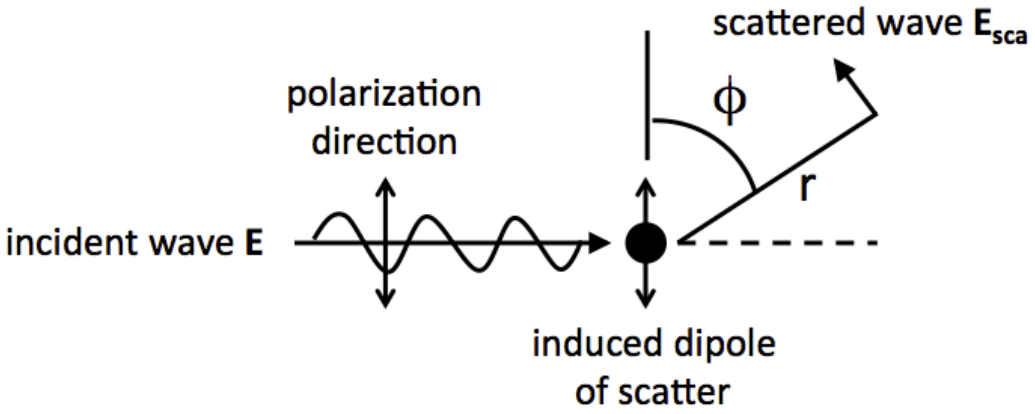

Figure D.1 Conceptual diagram of the electric wave scattering by the single dielectric particle.

Using the incident wave $\boldsymbol{E}$ and the scattered wave $\boldsymbol{E_{sca}}$, the intensites of the incident and the scattered light, I_0 and I_{sca} are given by

$$I_0 = \frac{c}{8\pi}|\boldsymbol{E}|^2 \tag{D.16}$$

$$I_{sca} = \frac{c}{8\pi}|\boldsymbol{E_{sca}}|^2 \tag{D.17}$$

Integrating I_{sca} over a sphere, we obtain the total energy scattered in all directions per unit time as:

$$W_{sca} = \frac{1}{3}\left(\frac{\omega}{c}\right)^4 c|\boldsymbol{p}|^2 \tag{D.18}$$

and dividing equation (D.18) by I_0, scattering cross section is represented as:

$$\sigma_{sca} = W_{sca}/I_0 = \frac{8\pi}{3}\left(\frac{\omega}{c}\right)^4 |\alpha|^2 \tag{D.19}$$

For spherical particles, electric polarizability can be written with refractive index m and radius a as:

$$\alpha = \frac{m^2-1}{m^2+2}a^3 \tag{D.20}$$

Direct substitution into the formula of equation (D.19) gives

$$Q_{sca} = \frac{8}{3}x^4 \mathrm{Re}\left(\frac{m^2-1}{m^2+2}\right)^2 \propto \lambda^{-4} \tag{D.21}$$

where x is the size parameter of particle defined by $x = 2\pi a/\lambda$. Hence, scattering cross section and efficiency is proportional to λ^{-4}, which is generally called Rayleigh scattering.

As for the absorption, if we now allow the grain material to have a finite absorption term (i.e., the imaginary part to the refractive index is non-zero), at long wavelengths ($Q_{abs} > Q_{sca}$). The absorption term is expressed with the imaginary part of electric polarizability α as:

$$\sigma_{abs} = \frac{4\pi\omega}{c}\,\mathrm{Im}\,(\alpha) \tag{D.22}$$

Thus, the absorption efficiency is given by

$$Q_{abs} = -4x\,\mathrm{Im}\left(\frac{m^2-1}{m^2+2}\right) \tag{D.23}$$

From equation (D.21) and (D.23), we see that for grains small with respect to wavelength ($x \ll 1$) the scattering efficiency is proportional to λ^{-4}, and the absorption cross section is proportional to λ^{-1}, which can be seen in longer wavelengths of Figure 5.5 and Figure 5.4.

D.3 Scattering and absorption in Mie theory

At optical wavelengths, the dust particles are not small compared to the wavelength of the scattered light, and electric dipole approximation is no longer applicable. We need to find the solution to Maxwell's equations with an incident plane wave, for an object of specified size and shape, composed of material with a specified dielectric function ϵ and refractive index m.

For the spherical grains, an analytic solution was found by Mie, and is known as Mie theory (Mie 1908). The electromagnetic field inside and outside the sphere can be decomposed into spherical harmonics with appropriate radial functions, with coefficients determined by the need to give an incident plane wave at infinity and to satisfy the continunity conditions at the surface of the sphere.

According to Mie theory, the efficiency factors of scattering and extinction are expressed in the form of the following series:

$$Q_{sca} = \frac{2}{x^2} \sum_{j=1}^{\infty} (2j+1) \left(|a_j|^2 + |b_j|^2 \right) \tag{D.24}$$

$$Q_{ext} = \frac{2}{x^2} \sum_{j=1}^{\infty} (2j+1) \operatorname{Re} (a_j + b_j) \tag{D.25}$$

$$Q_{abs} = Q_{ext} - Q_{sca} \tag{D.26}$$

where complex expansion coefficients a_j and b_j are called the Mie coefficients. The terms in the Mie series correspond to the partial waves of different orders. The number of terms, which should be taken into account, increases with increasing the diffraction parameter. Mie coefficients are expressed in terms of the Riccatty-Bessel functions Ψ_j and ξ_j.

$$a_j = \frac{\psi_j (x) \psi_j' (\beta x) - \beta \psi_j (\beta x) \psi_j' (x)}{\xi_j (x) \psi_j' (\beta x) - \beta \psi_j (\beta x) \xi_j' (x)} \tag{D.27}$$

$$b_j = \frac{\beta \psi_j (x) \psi_j' (\beta x) - \psi_j (\beta x) \psi_j' (x)}{\beta \xi_j (x) \psi_j' (\beta x) - \psi_j (\beta x) \xi_j' (x)} \tag{D.28}$$

where x is the size parameter of grains, β is the complex optical constant corresponding to materials.

The angular characteristics of scattering are expressed by the following complex amplitude functions, corresponding to perpendicular polarizations:

$$S_1 (\mu) = \sum_{j=1}^{\infty} \frac{2j+1}{j (j+1)} \left[a_j \pi_j (\mu) + b_j \tau_j (\mu) \right] \tag{D.29}$$

$$S_2(\mu) = \sum_{j=1}^{\infty} \frac{2j+1}{j(j+1)} \left[b_j \pi_j(\mu) + a_j \tau_j(\mu) \right] \tag{D.30}$$

Here $\mu = \cos\theta$, where θ is the angle of scattering measured from the direction of the incident radiation, and π_j and τ_j are special angular functions. The scattering phase function for linear polarized incident radiation is

$$\Psi(\theta, \varphi) = \left(\frac{2}{Q_{sca}} \right)^2 \left[|S_1(\theta)|^2 \sin^2\varphi + |S_2(\theta)|^2 \cos^2\varphi \right] \tag{D.31}$$

Angle φ is measured from the polarization plane of the incident radiation. For calculating the asymmetry factor of scattering, one can use the Debye equation,

$$g = \langle \mu \rangle = \left(\frac{2}{Q_{sca}} \right)^2 \sum_{j=1}^{\infty} \left[\frac{j(j+2)}{j+1} \mathrm{Re}\left(a_j a_{j+1}^* + b_j b_{j+1}^* \right) + \frac{2j+1}{j(j+1)} \mathrm{Re}\left(a_j b_j^* \right) \right] \tag{D.32}$$

where the asterisk denotes a complex conjugate quantity.

Absorbing particles with size much larger than the wavelength ($x \gg 1$) behave as an opaque screen ($Q_{abs} \approx 1$). Their edges diffract the incoming radiation and it can be shown that $Q_{sca} \approx 1$ so that $Q_{ext} \approx 2$, which is independent of wavelength as can be seen in shorter wavelengths of Figure 5.5 and Figure 5.4.

Acknowledgements

I am grateful to my supervisor Prof. Hideo Matsuhara (ISAS/JAXA) and Prof. Shuji Matsuura (Kwansei Gakuin University) for giving me a great opportunity to study the infrared astronomy and astrophysics. My deepest appreciation goes to Prof. Toshio Matsumoto (ISAS/JAXA), Dr. Kohji Tsumura (Tohoku university), Dr. Mai Shirahata (NAOJ), Dr. Toshiaki Arai (Tohoku university), Dr. Kei Sano (University of Tokyo) for valuable guidance throughout my all research activities.

This study is based on significant contributions from the MIRIS team. We greatly appreciate Prof. Woong-Seob Jeong (KASI), Dr. Jeonghyun Pyo (KASI), Dr. Il-Joong Kim (KASI), Dr. Hyun Jong Seo (KASI), Dr. Wonyong Han (KASI), Dr. Dae-Hee Lee (KASI), Dr. Bongkon Moon (KASI), Dr. Won-Kee Park (KASI), Dr. Youngsik Park (KASI), Mr. Min Gyu Kim (KASI) and all of the MIRIS staff for their observations and support in terms of data reduction.

In addition, we obtained advice on the selection of targets from Prof. Kazuhito Dobashi (Tokyo Gakugei University), Assoc. prof. Kimiaki Kawara (IoA-UT), and Dr. Yoshiki Matsuoka (IoA-UT), Dr. Nobuyuki Ienaka (IoA-UT) and also appreciate their guidance. The authors acknowledge support from the Japanese Society for the Promotion of Science, KAKENHI (grant number 26800112, 21111004, 15H05744).

Bibliography

Abraham P., Leinert C., Lemke D., 1997 A&A, 328, 702

Abramowski, A., Acero, F., Aharonian, F., et al. 2013, A&A, 550, A4

Aharonian, F., Akhperjanian, A. G., Bazer-Bachi, A. R., et al. 2006, *Nature*, 440, 1018

Albert, J., Aliu, E., Anderhub, H., et al. 2008, Science, 320, 1752

Arai, T., Matsuura, S., Bock, J., et al. 2015, ApJ, 806, 69

Arendt, R. G., Odegard, N., Weiland, J. L., et al. 1998, ApJ, 508, 74

Asplund, M., Grevesse, N., Sauval, A.J., & Scott, P. 2009, ARA&A, 47, 481

Bernstein, R. A. 2007, ApJ, 666, 663

Block, D.L. 1996, New Extragalactic Perspectives in the New South Africa

Brandt, T. D., & Draine, B. T. 2012, ApJ, 744, 129

Bruzual, G., & Charlot, S. 2003, MNRAS, 344, 1000

Cambrésy, L., Reach, W. T., Beichman, C. A., & Jarrett, T. H. 2001, ApJ, 555, 563

Caulet, A., Hook, R. N., & Fosbury, R. A. E. 1994, A&AS, 108, 271

Charlot, S., & Bruzual, G. 2007, unpublished, models distributed on demand (CB07)

Clayton, D. D., Liu, W., & Dalgarno, A. 1999, Science, 283, 1290

Cooray, A., & Yoshida, M. 2004, MNRAS, 351, 71

Cooray, A., Smidt, J., de Bernardis, F., et al. 2012b, Nature, 490, 514

Cutri, R. M., Skrutskie, M. F., van Dyk, S., et al. 2003, The IRSA 2MASS All Sky Point Source Catalog, NASA/IPAC Infrared Science Archive

Darbon, S., Perrin, J.M., & Sivan, J.P. 1999, A&A, 348, 990

Dwek, E., Arendt, R. G., & Krennrich, F. 2005a, ApJ, 635, 784

Désert, F.-X., Abergel, A., Bernard, J.-P., et al. 1996, American Institute of Physics Conference Series, 348, 96

de Vries, C. P., & Le Poole, R. S. 1985, A&A, 145, 7

Domínguez, A., Primack, J. R., Rosario, D. J., et al. 2011, MNRAS, 410, 255

Draine, B. T., & Lee, H.M. 1984, ApJ, 285, 89

Draine, B. T., & Li, A. 2007, ApJ, 657, 810

Draine, B. T., & Fraisse, A. 2009, ApJ, 696, 1

Draine, B. T. 2011, Physics of the Interstellar and Intergalactic Medium (Princeton University Press)

Dwek, E., & Krennrich, F. 2005, ApJ, 618, 657

Dwek, E., Krennrich, F., & Arendt, R. G. 2005b, ApJ, 634, 155

Elsässer, H., & Haug, U., 1960 ZAp, 50, 121

Elvey, C. T., & Roach, F. E. 1937, ApJ, 85, 213

Fernandez, E. R., & Komatsu, E. 2006, ApJ, 646, 703

Fernandez, E. R., Komatsu, E., Iliev, I. T. & Shapiro, P. R. 2010, ApJ, 710, 1089

Flaherty, K. M., Pipher, J. L., Megeath, S. T., et al. 2007, ApJ, 663, 1069

Girardi, L., Groenewegen, M. A. T., Hatziminaoglou, E., & da Costa, L. 2005, A&A, 436, 895

Gao, J., Jiang, B.W., & Li, A., 2009, ApJ, 707, 89

Gondhalekar, P. M. 1990, The Galactic and Extragalactic Background Radiation, 139, 49

Gordon, K. D., Witt, A. N., & Friedmann, B. C. 1998, ApJ, 498, 522

Guhathakurta, P., & Tyson, J. A. 1989, ApJ, 346, 773

Guy, J., Renault, C., Aharonian, F. A., et al. 2000, A&A, 359, 419

Han, W., Lee, D, H., Jeong, W, S., et al. 2014, PASP, 126, 853

Hauser, M. G., Arendt, R. G., Kelsall, T., et al. 1998, ApJ, 508, 106

Henyey, L. G., 1937, ApJ, 85, 213

Henyey, L. G., & Greenstein, J. L. 1941, ApJ, 93, 70

Ienaka, N., Kawara, K., Matsuoka, Y., et al. 2013, ApJ, 767, 80

Indebetouw, R., Mathis, J. S., Babler, B. L., et al. 2005, ApJ, 619, 931

Ishiguro, M., & Ueno, M., 2007, Observational studies of Interplanetary Dust, 231 Springer

Jiang, B.W., Gao, J., Omont, A., Schuller, F., & Simon, G. 2006, A&A, 446, 551

Jura, M. 1979, ApJ, 227, 798

Kashlinsky, A., Arendt, R. G., Mather, J., & Moseley, S. H. 2005, Nature, 438, 45

Kelsall, T., Weiland, J. L., Franz, B. A., et al. 1998, ApJ, 508, 44

Laureijs, R. J., Mattila, K., & Schnur, G. 1987, A&A, 184, 269

Lehtinen, K., & Mattila, K. 1996, A&A, 309, 570

Leinert, C., & Grun, E. 1990, Physics of the Inner Heliosphere I, 207

Leinert, C., Bowyer, S., Haikala, L. K., et al. 1998, A&AS, 127, 1

Levenson, L. R., Wright, E. L., & Johnson, B. D., 2007, ApJ, 666, 34

Li, A., & Greenberg, J.M. 1997, A&A, 323, 566

Li, A., 2004, invited review article for the international symposium gPenetrating Bars Through Masks of Cosmic Dusth, pp. 535-559

Low, F. J., Young, E., Beintema, D. A., et al. 1984, ApJ, 278, 19

Lutz, D. 1999, in The Universe as Seen by ISO, ed. P. Cox & M. Kessler (ESA Special Publ., Vol. 427; Noordwijk: ESA), 623

Madau, A., & Silk, J. 2005, MNRAS, 359, 37

Maraston C., 2005, MNRAS, 362, 799

Mathis, J. S., Rumpl, W., & Nordsieck, K. H. 1977, ApJ, 217, 425

Mathis, J. S., Mezger, P. G., & Panagia, N. 1983, A&A, 128, 212

Matsumoto, T., Matsuura, S., Murakami, H., et al. 2005, ApJ, 626, 31

Matsumoto, T., Kim, M. G., Pyo, J., & Tsumura, K. 2015, ApJ, 807, 57

Matsuoka, Y., Ienaka, N., Kawara, K., & Oyabu, S. 2011, ApJ, 736, 119

Matsuura, S., et al. 2014, gJoint Planetary andAstronomical Science with the Solar Power Sail Spacecraft.h Trans. JSASS, Aerospace Tech. Japan, 12, ists29, Tr 1

Mattila, K. 1976, A&A, 47, 77

Mattila, K. 1979, A&A, 78, 253

Mattila, K., Lehtinen, K., Väisänen, P., et al. 2011, Proceedings IAU Symoisium No. 284, 429

Mazin, D., & Raue, M. 2007, A&A, 471, 439

Melbourne, J. et al. 2012, ApJ, 748, 47

Mie, G, 1908 "Beiträge zur Optik trüber Medien, speziell kolloidaler Metallösungen". Annalen der Physik. 330, 377-445.

Mii, H., & Totani, T. 2005, ApJ, 628, 873

Meyer, M., Raue, M., Mazin, D., & Horns, D. 2012, A&A, 542, 59

Nishiyama, S., Tamura, M., Hatano, H., et al. 2009, ApJ, 696, 1407

Nozawa T., Kozasa T., Habe A., 2006, ApJ 648, 435

Nozawa T., Kozasa T., Habe A., et al. 2007, ApJ, 666, 955

Orr, M. R., Krennrich, F., & Dwek, E. 2011, ApJ, 733, 77

Pagani, L., Steinacker, J., Bacmann, A., et al. 2010, Science, 329, 1622

Parvathi, V. S., Sofia, U. J., Murthy, J., & Babu, B. R. S. 2012, ApJ, 760, 36

Planck Collaboration XVII 2014, A&A, 566, A55

Pyo, J., Matsumoto, T., Jeong, W. S., & Matsuura, S., 2012, ApJ, 760, 102

Salvaterra, R., & Ferrara, A. 2003, MNRAS, 339, 973

Sano, K., Kawara, K., Matsuura, S., et al. 2015, ApJ, 811, 77

Sano, K., Kawara, K., Matsuura, S., et al. 2016, ApJ, 818, 72

Sano, K., Matsuura, S., Tsumura, K., et al. 2016, ApJL, 821, 11

Santos, M. R., Bromm, V., & Kamionkowski, M. 2002, MNRAS, 336, 1082

Savage, B. D., & Sembach, K. R. 1996, ARA&A, 34, 279

Schlegel, D. J., Finkbeiner, D. P., & Davis, M. 1998, ApJ, 500, 525

Schroedter, M. 2005, ApJ, 628, 617

Skrutskie, M. F., Cutri, R. M., Stiening, R., et al. 2006, ApJ, 131, 1163

Steinacker, J., Ormel, C. W., Andersen, M., & Bacmann, A. 2014, A&A, 564, 96

Smith, T. L., & Witt, A. N. 2002, ApJ, 565, 304

Thompson, R. I., Eisenstein, D., Fan, X., Rieke, M., & Kennicutt, R. C. 2007, ApJ, 657, 669

Thompson, R. I., Eisenstein, D., Fan, X., Rieke, M., & Kennicutt, R. C. 2007, ApJ, 666, 658

Tsumura, K., Battle, J., Bock, J., et al. 2010, ApJ, 719, 394

Tsumura, K., Matsumoto, T., Matsuura, S., et al. 2013, PASJ, 65, 120

Tsumura, K., Matsumoto, T., Matsuura, S., et al. 2013, PASJ, 65, 121

Uemizu, K., Bock, J. J., Kawada, M., Lange, A., E., Matsumoto, T., Watabe, T., & Yost, S. A. 1998, ApJ, 506, 15

van de Hulst, H. C., & de Jong, T. 1969, Phy, 41, 151

Wang, S., Gao, J., Jiang, B. W., Li, A., & Chen, Y. 2013, ApJ, 773, 30

Weingartner, J. C., & Draine, B. T. 2001, ApJ, 548, 296

Witt, A. N., & Schild, R. E. 1985, ApJ, 294, 225

Witt, A.N., Lindell, R.S., Block, D.L., & Evans, R. 1994, ApJ, 427, 227

Witt, A. N., Gordon, K. D., Vijh, U. P., et al. 2006, ApJ, 636, 303

Witt, A. N., Mandel, S., Sell, P. H., Dixon, T., & Vijh, U. P. 2008, ApJ, 679, 497

Wolstencroft R. D., Rose L. J., 1966, Nature, 209, 388

Wright, E. L. 1998, ApJ, 496, 1

Wright, E. L. 2001, ApJ, 553, 538

York, D. G., Adelman, J., Anderson, J. E., Jr., et al. 2000, AJ, 120, 1579

Zemcov, M., Smidt, J., Arai, T., et al. 2014, Science, 346, 732

Zibetti, S., Gallazzi, A., Charlot, S., Pierini, D., Pasquali, A. 2013, MNRAS, 428, 1479

Zubko, V., Dwek, E., & Arendt, R. G. 2004, ApJS, 152, 211